Development and Translation of Fluorine-19 MRI for Lymphocyte Tracking

by

Lawrence M. Lechuga

A dissertation submitted in partial fulfillment of

the requirements for the degree of

Doctor of Philosophy

(Medical Physics)

at the

UNIVERSITY OF WISCONSIN-MADISON

2022

Date of final oral examination: June 3, 2022

The dissertation is approved by the following members of the Final Oral Committee:

Sean Fain, Professor, Radiology
Oliver Wieben, Professor, Medical Physics
Diego Hernando, Associate Professor, Medical Physics
Sandro Mecozzi, Professor, Pharmacy
Christian Capitini, Associate Professor, Pediatrics

TABLE OF CONTENTS

Development and Translation of Fluorine-19 MRI for Lymphocyte Tracking

By

Lawrence M. Lechuga

A dissertation submitted in partial fulfillment of the requirements for the degree of

Doctor of Philosophy

(Medical Physics)

Performed under the supervision of:

Sean B. Fain, Ph.D., Professor, Departments of Medical Physics, Biomedical Engineering, and Radiology

ABSTRACT

Magnetic resonance imaging (MRI) is a non-invasive, non-ionizing imaging modality that can be relied on for the longitudinal evaluation of patients with a variety of structural and functional irregularities. The goal of this thesis is to develop preclinical cell tracking techniques using Fluorine-19 (^{19}F) MRI and translate it to a clinical 3T platform. The advances in cellular-based therapies and the ability to expand and activate lymphocytes have renewed interest in these immunotherapy approaches for refractory cancers. However, after *in vivo* delivery of these activated immune cells, the location and lifetime of these cells are often unknown. Non-invasive tracking and quantification of these adoptively transferred cells can provide relevant information to improve treatment efficacy. Accordingly, preclinical cell tracking studies were performed in various cell types to detect and quantify cells after *in vivo* delivery. These cell tracking studies were applied to natural killer (NK) cells in a murine lymphoma model as cells were tracked and quantified *in vivo,* where label retention and cellular viability were subsequently validated. This work establishes the ability of ^{19}F MRI to detect and quantify NK cells in a syngeneic murine cancer model with high specificity multiple days after injection. To address the need for clinical applicability, a dual tuned ^{1}H/^{19}F multichannel coil was installed on a clinical 3T platform, where product pulse sequences were modified to allow for multinuclear manual prescan and data acquisition. Sequences were modeled and optimized for improved signal-to-noise (SNR) efficiency where the sensitivity and detection limits were assessed in phantoms for a popular ^{19}F cellular probe. Additionally, ^{19}F detection was demonstrated in an ex vivo canine model where detection limits were assessed. Overall, this work demonstrates the utility of ^{19}F MRI for longitudinal lymphocyte tracking and provides the foundational development of ^{19}F MRI for a clinical setting.

To my family, for all of their love and support throughout this long journey

ACKNOWLEDGMENTS

This work and my subsequent training were financially supported in part by the AOF SciMed GRS fellowship and the Radiological Sciences T32 training grant (CA009206). These research projects were also supported in part by the National Cancer Institute/National Institutes of Health (NCI/NIH) R01 CA215461, NCI/NIH P30 CA014520, University of Wisconsin Carbone Cancer Center Cancer Immunotherapy/Tumor Immunology pilot grant, and American Cancer Society Research Scholar grant RSG-18-104-01-LIB.

Thank you to my advisor, Dr. Sean Fain, who made my education and Ph.D. training a possibility. I am very grateful for the mentorship and encouragement that I have received from him throughout my Ph.D. work. Through his constructive critiques and encouragement, I have become a much more independent and competent researcher. Thank you for all of the time and effort you have put into my training and professional development. To my committee members, Dr. Christian Capitini, Dr. Diego Hernando, Dr. Oliver Wieben, and Dr. Sandro Mecozzi, thank you for all of your advice, guidance, and feedback that has improved my competency as a scientist. Their expertise has proven to be a wonderful resource that has greatly improved the quality and perspective of my research.

To the several past and Fain Lab members, Dr. Kai Ludwig, Dr. Greg Barton, Dr. Andrew Hahn, and Dr. Katie Carey, thankx you for all of your help training and assisting me in coding and running the scanners. Furthermore, to all past and current Fain Lab members, especially (future) Dr. Luis Torres, thank you for all of your technical help, collaboration, and friendship throughout my Ph.D. journey, you have all made it such a memorable and great experience.

Many professional collaborations and friendships have developed during my journey here at UW-Madison that I will remember for a lifetime. Some of the important people not mentioned above, include Dr. Phil Corrado, Grant Roberts, Daniel Seiter, Ruiming Chen Edmondson, Alma Spahic, Mu-

Lan Jen, Hayley Whitson, Dalton Griner, Dr. Syndey Jupitz, Dr. Jonas Rodriguez, Dr. Charlene Rivera Bonet, Dr. Matthew Forsberg, Monica Cho, and countless others, thank you!

To my family, thank you for all of your love and support over the years. Mom, thank you for your countless sacrifices, encouragement, and all of the love that you have given me throughout my life. To my siblings, Kyle, Sheridan, and Shely, thank you for always accepting and loving me unconditionally, but also keeping me grounded. To my grandparents and dad, thank you for all of the phone calls, advice, and love that have helped me remain strong in times of doubt. To my extended family and friends, Dillon, Adam, Derrick, and Benito, thank you for the friendship, despite the distance, that has proven priceless over the years.

Lastly, to my amazing girlfriend, Dr. Charina Ruiz, whose love and support have kept me motivated and afloat over the last 4 years, thank you. Your sacrifices, unconditional love, and encouragement have allowed me to reach this milestone in my career. I could not have done it without you. I am so excited about what the future has in store for us! Also, shout out to my good boy, Rafa, for being the best coworker and pet over the last year and a half. Time to explore California!

LIST OF FIGURES

LIST OF TABLES

LIST OF ABBREVIATIONS

^{19}F	Fluorine-19
^{51}C	Chromium-51
ACK	Ammonium-chloride-potassium
ACT	Adoptive cell transfer
ADCC	Antibody-dependent cellular cytotoxicity
ALL	Acute Lymphoblastic Leukemia
ARC	Autocalibrating Reconstruction for Cartesian Imaging
BLI	Bioluminescence imaging
bSSFP	Balanced Steady-State Free Precession
CAR	Chimeric antigen receptor
CCK8	Cell counting kit 8
CMM	Complete mouse media
CS	Compressed sensing
CSE	Chemical shift encoding
CTLA-4	Cytotoxic T-lymphocyte associated protein 4
DC	Dendritic cell
D$_2$O	Deuterium oxide
DLS	Dynamic light scattering
DPBS	Dulbecco's phosphate-buffered saline
ETL	Echo train length
EPR	Enhanced Permeability and retention
FA	Flip angle
FBS	Fetal bovine serum
F$_C$	Cellular loading density
FIESTA	Fast Imaging Employing Steady-State Acqusition
FOV	Field of view
FSE	Fast spin-echo
GFP	Green fluorescent protein
GRAPPA	Generalized Autocalibrating Partial Parallel Acquisition
GVHD	Graft versus host disease
IACUC	Institutional Animal Care and Use Committee

IFN-γ	Interferon-gamma
IL-2	Interleukin 2
mAb	Monoclonal antibody
MFI	Median fluorescent intensity
MIP	Maximum intensity projection
NE	nanoemulsion
NEX	Number of excitations
NK	Natural killer
NMR	Nuclear magnetic resonance
OI	Optical imaging
OSA	Osteosarcoma
PBS	Phosphate-buffered saline
PCR	Polymerase chain reaction
PET	Positron emission tomography
PFC	Perfluorocarbon
PFCE	Perfluoro-15-crown-5-ether
PFPE	Perfluoropolyether
RBC	Red blood cell
RES	Reticuloendothelial system
ROI	Region of interest
RF	Radiofrequency
SD	Standard deviation
SEM	Standard error of the mean
SENSE	SENSitivity encoding
SNR	Signal-to-noise
SPECT	Single photon emission computed tomography
SPGR	Spoiled Gradient Recalled Echo
SPIO	Superparamagnetic iron oxide
SSFP	Steady-state free precession
TAA	Tumor associated antigen
TFA	Trifluoroacetic acid
TSA	Tumor specific antigen

TNF-α	Tumor necrosis factor alpha
UTE	Ultrashort echo time

INTRODUCTION

Motivation

As of 2018, the global cancer burden rose to 18.2 million new cases with over 9.6 million deaths worldwide.[1] As the second leading cause of death worldwide, cancer remains extremely challenging to treat and cure. The established method for primary lesions relies on radiotherapy, surgery, chemotherapy, or a combination of each. These methods can be very effective but they carry a significant risk of severe side effects including toxicity to healthy cells, cancer resistance to chemotherapy and radiation, and tumor relapse.[2,3] The immunotherapy approach, which has been increasing in success, has shown encouraging results as a treatment paradigm for those suffering from refractory malignancies.

One strategy in the immunotherapy arsenal is to deliver lymphocytes expanded *ex vivo* and reintroduce them into the patient to elicit an increased antitumor response. A common T cell therapy infuses exogenously modified chimeric antigen receptor T cells (CAR-T) to target tumors. This breakthrough has shown great success in treating many pediatric and adult hematological cancers among others such as acute lymphoblastic leukemia (ALL), B-cell lymphoma, and multiple myeloma. Another promising immunotherapy approach uses infusions of natural killer (NK) cells to treat cancers, like leukemia and refractory neuroblastomas.[4–6] The advantageous safety profile and ability to recognize abnormal cells without prior sensitization makes this an attractive approach.

While these immunotherapies are encouraging and have shown exciting results, they struggle to elicit a reliable response rate within solid tumors. Given the complex mechanisms restricting lymphocyte infiltration of the tumor microenvironment and immunosuppressive effects, more tools are needed to best adapt the approach for solid tumors. Previous work has shown that the distribution and tumor infiltration of these effector lymphocytes hold important clinical information that can inform treatment decisions.[7–10] Additionally, the FDA has published guidelines, suggesting that cellular therapies should include imaging techniques to monitor transferred cells in a clinical and preclinical setting.[11] One such imaging modality, known as Fluorine-19 MRI (^{19}F MRI), is a noninvasive, nonradioactive imaging technique that is capable of tracking and quantifying cell populations *in vivo* with high specificity. ^{19}F MRI can be used to track and quantify immune cells labeled with perfluorocarbons (PFC) *in vivo* over days to weeks without interference from background contrast.[12,13] ^{19}F MRI, therefore, provides a unique opportunity over other cell-based imaging modalities to explore the persistence and behavior of immune cells post-injection.

Objectives

The overall goal of this thesis project is to develop ^{19}F MRI methodology in preclinical mouse cancer models using a dedicated small animal MRI system to provide quantitative cell tracking and to extend these methods to build the foundation for translation of this technology to a clinical 3T platform. The specific objectives of this proposed research are: 1) to characterize and improve cellular viability and labeling to maximize ^{19}F contrast agent cell uptake; 2) to validate and detect immune cell populations via ^{19}F MRI for tracking adoptively transferred cells after injection in preclinical tumor models; 3) to translate ^{19}F MRI technology to a clinical multichannel platform where multinuclear manual prescan techniques and fast pulse sequences will be developed, assessed, and applied to *ex vivo* models. To accomplish these objectives, specific aims were identified and are discussed in more detail below.

Aim 1: **Detect and quantify ^{19}F-labeled lymphocytes in cancer models**

Subaim 1: Characterize and detect adoptively transferred ^{19}F-labeled T cells in a metastatic melanoma model

Subaim 2: Characterize, track, and quantify PFC-labeled GFP+ natural killer (NK) cells in a syngeneic lymphoma model with postmortem validation

Subaim 3: Implement and test a novel highly fluorous ^{19}F contrast agent for the assessment of cancer imaging

Aim 2: Develop techniques for ^{19}F imaging with an 8-channel ^{1}H/^{19}F coil on a clinical 3T system

Subaim 1: Setup coil and convert several GE product sequences to allow for multinuclear data acquisition

Subaim 2: Develop manual prescan techniques to calibrate flip angle and determine the center frequency for the ^{19}F contrast agent

Aim 3: Maximize and assess SNR-efficiency for ^{19}F-MRI using gradient echo and steady-state free precession pulse sequences

Subaim 1: Determine the theoretical optimal sequence parameters to maximize SNR-efficiency and validate choices experimentally

Subaim 2: Assess the achieved sensitivity in phantom and *ex vivo* experiments

Subaim 3: Demonstrate the feasibility of phantom and ex vivo detection using ARC acceleration

Innovation

The innovation demonstrated in this thesis can be summarized in two points. First, at the time of writing this document, there are only 2 other works demonstrating the ability to detect NK cells using ^{19}F MRI. Of these works, our published research is the first to rigorously demonstrate detection, quantification, and specificity of murine NK cells within a syngeneic lymphoma model.

Leveraging the dual-fluorescent labeling, this preclinical study provided rigorous validation and assessment of cellular viability and ^{19}F label retention within the adoptively transferred cells 6 days after injection. This demonstrated methodology can now be easily extended to various other adoptive cell therapy cancer models.

Second, this work demonstrates the use of a dual-tuned ^{1}H/^{19}F multichannel phased array coil on a clinical platform. This research demonstrates a workflow for calibrating center frequency and radiofrequency (RF) transmit gain to achieve an accurate flip angle for a common ^{19}F cellular tracking probe. This work goes on to establish relaxation times for the ^{19}F-contrast agent and concentration detection limits for 3 optimized sequences. Additionally, this work demonstrates detection feasibility in a concentration phantom and in ex vivo tissues for both non-accelerated and parallel imaging acquisitions. Overall, the methodology developed can be adapted for the optimization of sequences for various ^{19}F contrast agents of interest, including the calibration of center frequency and flip angle, and for *ex vivo* and *in vivo* cell detection studies.

Summary of chapters

The overall development and presentation of this dissertation are organized into 7 distinct chapters as described below:

Chapter 1: A background and introduction to cellular-based immunotherapies, including natural killer (NK) and T cell applications, for the treatment of cancer, will be presented. A review of various *in vivo* lymphocyte imaging techniques will be introduced. ^{19}F contrast agents for cellular tracking in ^{19}F MRI, along with relevant applications, acquisition and quantitative techniques, and current challenges faced in the field will be presented.

Chapter 2: Tracking of perfluorocarbon (PFC) labeled murine T-cells within a metastatic melanoma cancer vaccine model is presented. Quantification of ^{19}F label uptake, *in vitro* effects, and label validation via confocal microscopy will be demonstrated. *In vivo* detection limits and IV detection feasibility will also be demonstrated. This chapter will conclude by discussing some of the challenges we faced, and steps taken to improve the methodology.

Chapter 3: Via ^{19}F MRI, tracking and quantification of PFC labeled green fluorescent protein (GFP+) murine NK cells within lymphoma over 6 days is presented. Characterization of *in vitro* effects, quantification and validation of PFC label uptake, and validation of label retention and cellular viability are established.

Chapter 4: The *in vivo* detection and passive tumor targeting of a novel ^{19}F contrast agent over 14 days in tumor-bearing mice is presented. Improved cellular ^{19}F uptake is demonstrated and quantified in murine T cells via ^{19}F NMR. Passive tumor and organ uptake over 14 days are assessed.

Chapter 5: The implementation of a dual-tuned multichannel proton/Fluorine-19 torso coil is presented here. A basic overview of the coil, sequence capabilities, and a flip angle and center frequency calibration protocol are presented here. Moreover, the theoretical parameter optimizations for spoiled gradient recalled echo (SPGR), balanced steady-state free precession (bSSFP), and phase-cycled (PC) bSSFP to maximize signal-to-noise (SNR) efficiency for a common PFC agent is demonstrated for a clinical 3T system. Ernst angle validation and receiver bandwidth (rBW) testing were demonstrated for each sequence. Achieved SNR-efficiency and ^{19}F concentration detection limits in phantoms were assessed and compared for each sequence. The performance of PC-bSSFP and detection limits were also determined in a canine *ex vivo* model. The feasibility of an Autocalibrating Reconstruction for Cartesian imaging (ARC) parallel imaging acceleration technique is also demonstrated in phantom and *ex vivo* models.

Chapter 7: The overall results of this dissertation research are summarized, and the future directions are discussed.

Chapter 1 BACKGROUND: IMAGE GUIDANCE FOR CELLULAR-BASED IMMUNOTHERAPIES

1.1 Immunotherapy for cancer

Throughout an individual's lifetime, the host immune system plays a significant role in detecting and preventing the development of neoplasia.[14] Yet, cancer has evolved various mechanisms to survive and grow within its host. The tumor microenvironment can utilize these complex mechanisms to restrict immune cell infiltration and otherwise suppress the host immune system.[15] More specifically, tumor cells can evade the immune system by down regulation of MHC expression, antigen loss, and cytokine production changes, which can create an immunoprivileged tumor microenvironment.[16]

Over 100 years ago Dr. Paul Ehrlich, the father of modern chemotherapy, discussed medicine's "magic bullet" as a strategy to aim directly at malignant and diseased cells.[17] In recent years, an approach known as cancer immunotherapy has developed into an effective treatment against cancers, in which the body's immune system can be leveraged to target cancerous cells. This evolving strategy has the promise to provide less toxicity and more reliable response rates against primary tumors and metastases.[3] The immunotherapy treatment arsenal can be categorized in the following ways:

- Cytokine Therapies: small proteins that bind to surface cell receptors to signal the changes in function, survival, and development of various immune cells.[18] For example, Interleukin-2 (IL-2) is one cytokine that has been used to successfully treat cancers such as metastatic renal cell carcinoma.[19]
- Monoclonal Antibodies: specialized proteins created by hybridized cells that can bind to a single specific epitope, as opposed to antibodies which bind to multiple epitopes.[20] One of

the earliest mAbs approved to treat cancer is known as rituximab, which was successful at treating forms of Non-Hodgkin's lymphoma.[21]

- Checkpoint inhibitors: drugs that work to block or inhibit the immune system's regulatory checks that can suppress tumor cell killing and detection. Among the first checkpoint inhibitors discovered, cytotoxic T lymphocyte-associated antigen 4 (CTLA-4) was a groundbreaking discovery that is approved to treat advanced melanoma.[22]
- Cancer vaccines: tumor-associated antigens are delivered to subjects to induce an antitumor response or immune protection. For example, a successful HPV vaccine was approved in recent years to reduce the risk of cervical and head and neck cancers.
- Adoptive cell transfers (ACT): lymphocytes are cultured *ex vivo* and introduced to the patient where these cells can stimulate the endogenous immune system and target tumor cells directly.

Each of these approaches are aiming to invoke an antitumor response by either stimulating an endogenous immune response, targeting specialized surface receptors to block checkpoint inhibition, or flagging specific tumor markers for death. As seen in Figure 1.1, the number of FDA approved therapeutics based on mAbs has dramatically increased in the last decade to over 100 total in 2021.[23,24]

Historically, parallel success was also seen in the field of cellular therapies. As early as 1988, Steven Rosenburg et al. demonstrated the antitumor effects of Tumor-Infiltrating Lymphocytes (TILs) in a preclinical model[25], and then 2 years later followed up with a study[26] in humans using genetically modified TILs for treatment in advanced melanoma cases. During that same decade (1989), the seminal work was published detailing the generation of the first chimeric antigen receptor (CAR) T cells.[27] Since then, improvements in the CAR T manufacturing process and constructs were made, and by 2017, two clinical trials using CD19 CAR T cell therapies for acute lymphoblastic leukemia (ALL) and large B cell lymphoma led to their approval by the FDA.[28,29] This FDA approval paved the way for its use and subsequent approval to treat mantle cell lymphoma and multiple myeloma.[30]

While CAR-T cell therapies have demonstrated great success in the treatment of various indications of advanced cancers, NK cells are emerging as an attractive potential candidate for new ACT therapies. NK cells are an attractive alternative to T cell-based therapies because they can target malignant or diseased cells without needing prior sensitization or previous exposure to the cancer cell antigens.[31] These cells also have the capacity to attack transformed cells via antibody dependent cellular cytotoxicity (ADCC), produce various cytokines like interferon-gamma and tumor necrosis factor alpha, and can be highly activated and expanded *ex vivo*.[32] NK cells are also inhibited by the presence of Human Leukocyte Antigen (HLA) protein that is highly expressed in healthy tissues, by interacting with the killer-cell immunoglobulin-like receptor (KIR), which blocks their activation in healthy tissue.[33] Furthermore, NK cell therapies do not require HLA matching and do not contribute to graft versus host disease (GVHD), which is a distinct advantage over T cell approaches.[34]

1.2 Image-guidance in cancer immunotherapies

While the Response Evaluation Criteria in Solid Tumors (RECIST) remains the criterion of choice for evaluating the treatment response for chemotherapy-based cancer treatments, there remain several challenges in applying this to immunotherapy approaches.[35] As explained in Seymour et al., currently immunotherapies lack sufficient biomarkers to predict and quantify treatment response in patients. Furthermore, the unique treatment approach of these immune-modulating and ACT drugs can create treatment responses that appear as tumor progression, termed pseudoprogression.[36] It is believed that this pseudoprogression is caused by a local inflammatory response where effector immune cells infiltrate the tumor microenvironment enlarging the tumor, and thus incorrectly appear on anatomic images or exams as tumor progression.[37] The limitation of anatomic imaging to capture the underlying biology highlights the need for alternative approaches that can improve our understanding of these treatments.[38]

There exist several molecular imaging approaches that can be utilized, *in vivo*, to track effector immune cells in cellular-based therapies. Optical imaging (OI) methods[39] such as fluorescence[40] and bioluminescence (BLI) imaging have proven to be valuable tools to help track cells *in vivo* within a preclinical setting. BLI is a common and versatile modality that utilizes luciferase reporters to create enzymes that can be used to create an optical signal within its host. While BLI is a sensitive and low-cost technique, it is limited to preclinical models given its low resolution and limited depth of penetration of approximately 1 cm.

Other approaches, like Single-photon Emission Computed Tomography (SPECT) and Positron Emission Tomography (PET) imaging rely on radioactive compounds to generate a quantitative signal *in vivo*. The superb sensitivity allows for the detection of concentrations on the order of picomoles/L, which allows for dosages of radiopharmaceuticals on the order of nanograms.[41] The low doses of radiotracers are unlikely to elicit a pharmacological effect[41]; however, PET/SPECT also has several limitations. These imaging techniques deliver ionizing radiation to the subject limiting its repeated use, decay away over time due to limited radioactive half-life, have relatively low resolution, and require infrastructure, like a cyclotron or generator, to generate the radioisotopes.

PET and SPECT techniques are the most common of the cell-tracking techniques, but their previously mentioned disadvantages and their inability to provide anatomic information have allowed for the exploration of alternate approaches. Recently, MRI has emerged as an alternative approach with the potential for broad clinical applicability. Conventional MRI generates a signal through manipulation of proton's (^{1}H) magnetic moment, and thus magnetization through the use of a strong magnetic field and radiofrequency (RF) pulses.[42] *In vivo*, tissues return to their equilibrium states at different rates, termed spin-lattice (T_1) and spin-spin (T_2) relaxation times, which allows MRI to generate images with superb soft tissue contrast and high resolution. Further manipulation of the T_1 and T_2 relaxation times can be achieved by using paramagnetic agents, like Gadolinium(III)[43] or Super Paramagnetic Iron Oxide (SPIO)[44] particles. The latter method relies on negative contrast to create strong fluctuations in the local magnetic field, which ultimately lead to a hypointense signal in regions of high SPIO concentration. This imaging method has been successfully used to track various cell types, such as mesenchymal stem cells[45] and lymphocytes[46,47], and even demonstrated great sensitivity by detecting single cells.[48] While MRI using SPIO for cellular tracking relies on negative contrast, it provides high resolution, great sensitivity, and has no depth of penetration issues compared to optical imaging techniques.

1.3 Fluorine-19 Magnetic Resonance Imaging

Given its advantageous sensitivity and abundance in biological systems, conventional MRI focuses on imaging ^1H nuclei; however, imaging of other nuclei can be performed if the nuclei are magnetically active. While ^1H MRI can provide anatomic and functional information, other nuclei may provide alternative methods for developing new biomarkers. Table 1 summarizes the properties of magnetically active nuclei that can be imaged using MRI.[49] It can be seen from Table 1, that ^1H nuclei have favorable natural abundance, biologic concentration, and sensitivity compared to all other MR-active nuclei. However, another strong candidate for MR imaging is ^{19}F, which has comparable sensitivity to ^1H at 83.3%. With 100% natural abundance and very low endogenous biological concentration, there is effectively no confounding background signal, leading to an unambiguous ^{19}F signal. Exogenous contrast agents can then be introduced to the biological system to allow for highly specific imaging.

Table 1.1: Nuclear properties and approximate biologic concentration in humans of various MR-active nuclei.

x	Spin	γ (MHz/T)	Relative sensitivity	% Natural Abundance	Biologic Concentration
^{1}H	1/2	42.58	1.000	99.99	88 M
^{3}He	1/2	32.43	0.442	0.0001	-
^{13}C	1/2	10.71	0.016	1.109	-
^{19}F	1/2	40.06	0.833	100	4 μM
^{23}Na	3/2	11.26	0.018	100	80 mM
^{31}P	1/2	17.25	0.066	100	75mM

1.3.1 *Perfluorocarbons for ^{19}F MRI*

The main contrast agents used in ^{19}F MRI are organofluorine compounds known as perfluorocarbons (PFCs). These fluorinated compounds have a carbon backbone and the resulting C-F bonds are one of the strongest single bonds known in organic chemistry.[50] This stability makes PFC agents physiologically inert in animals and humans, with no metabolism being observed *in vivo*.[51,52] PFCs are cleared by exhalation in the lungs and/or uptake into the reticuloendothelial system (RES), which is comprised of phagocytic cells like monocytes and macrophages. However, these agents are very fluorophilic and are not miscible in water or hydrophobic substances. For this reason, PFCs need to be emulsified for intravenous delivery. The PFC core along with the emulsifier, typically phospholipids or poloxamers, can be formed into a nanoemulsion (NE), as shown in a simple graphic in Figure 1.2, using microfluidization or high-pressure homogenization, with a typical target droplet size being 100-200 nm in diameter.[53] PFC nanoemulsions have been extensively studied for application in various biomedical applications, such as blood substitutes[51,52] and ultrasound[54] contrast agents.

Two PFC agents of particular interest are known as perfluoropolyether (PFPE) and perfluoro-15-crown-5-ether (PFCE). Their structures, shown in Figure 1.3, emphasize why they are favorable for ^{19}F MRI implementation. The 20 magnetically-equivalent fluorine nuclei in the PFCE structure results in a single strong fluorine NMR peak; whereas the linear PFPE structure exhibits 1 predominant peak with greater than 40 magnetically-equivalent fluorine atoms and two small side peaks.[13] These PFC agents have been used in many MRI applications including oximetry[55] and cellular tracking.[56] Many cell types, such as macrophages[57–59], NK cells[60–62], T cells[63,64], CAR T cells[10], dendritic cells[65,66] (DC), and various stem cells[67–69] have been monitored *in vivo* using ^{19}F MRI. While most of these studies were performed in a preclinical setting, the first human phase I clinical trial demonstrated the ability to track PFC labeled DCs by ^{19}F MRI in patients with stage 4 colorectal cancer at 3T.[65]

1.3.2 *Cellular detection and quantification*

In ^{19}F MRI, cells can be labeled either *in situ*, or *ex vivo*.[70] For *in situ* labeling, the PFC NE is injected directly and is largely taken up by phagocytic cells like monocytes, macrophages, and to a lesser amount neutrophils, granulocytes, and B cells, which can be imaged to assess an inflammatory response.[71–73] Labeling of specific cells can be accomplished by culturing the cells *ex vivo* with the PFC nanoemulsion, which allows for intracellular uptake. Multiple studies have demonstrated that *ex vivo* labeled stem cells and other lymphocytes can be tracked for days or weeks post-injection. Unlike methods using SPIO, which detect labeled cells indirectly, PFC labeled cells detected with ^{19}F MRI will produce positive contrast “hot-spot” images that are much easier to interpret and will not perturb the ^{1}H anatomic images.

Given the signal linearity with ^{19}F concentration and positive contrast images, quantification of the cell numbers can be achieved *in vivo.*[63] Quantitively tracking the distribution of injected cells is critical to understanding cellular therapies deeper and improving their efficacy.[70] Quantification of cells from ^{19}F images requires prior knowledge of multiple values:

- Labeling efficiency (F_C): The number of ^{19}F nuclei within each cell on average. This is determined by performing nuclear magnetic resonance (NMR) spectroscopy on lysed samples of the PFC-labeled cell populations. Utilizing a quantitative reference standard, such as trifluoroacetic acid (TFA), the relative area under the curves for the PFC and TFA resonance peaks can be calculated to determine the number of ^{19}F nuclei with the samples.

- Reference vial ^{19}F concentration (ρ_{ref}): The concentration of ^{19}F nuclei within a PFC reference vial that is placed within the imaging field of view during ^{19}F MRI acquisitions.

After thresholding, the images at a signal-to-noise ratio (SNR) of 4 or 5, the total signal from the labeled cells (ΣS_V) within a region-of-interest (ROI) and the average signal in the ^{19}F reference vial (S_{ref}) can be calculated, as seen in the example in Figure 1.4. Utilizing the prior information, the image derived values, and spin-density weighted ^{19}F acquisitions, the total number of detected cells can be calculated as seen in Equation 1.1.

$$N_c = \sum S_V \cdot \frac{\rho_{ref}}{F_C \cdot S_{ref}} \tag{1.1}$$

These cell quantification methods have been demonstrated and validated in multiple studies; however, cross-validation steps remain a critical component for this imaging modality.[74] One method of validating cell labeling *in vitro*, *in vivo*, and *ex vivo* is to use PFC nanoemulsions that include a fluorescent label. To confirm cellular uptake of the PFC label, electron microscopy of the cells is the gold standard for validation purposes, as its high-resolution method allows for direct visualization of individual cellular compartments and nanoemulsion particles.[75] However, many PFC nanoemulsion formulations either incorporate fluorophores into the emulsion[73] or are covalently bound to the PFC[76] itself. One particular strength of the linear PFPE agent is its ability to incorporate a red BODPY-TR fluorophore directly, via covalently binding to the PFPE amides.[77] This allows for label uptake validation via confocal microscopy; however, when using this approach care must be taken to ensure proper staining of the cell membrane and nucleus to ensure true intracellular labeling.[74]

1.3.3 *Challenges*

Although the popular PFC agents provide many fluorine nuclei in a single nanoemulsion droplet, there remain some challenges. Upon uptake into the cell or after intravenous injection, the agent decreases in concentration as it is diluted moving through the bloodstream and organs; therefore, a NE needs to be chosen that can stably load large amounts of PFCs to increase ^{19}F signal strength per unit volume. As addressed in Chapter 5, due to the intrinsically low ^{19}F

concentration that can be effectively achieved *in vivo*, careful consideration should be taken in the choice of the pulse sequence and its parameters to ensure optimal signal acquisition efficiency.

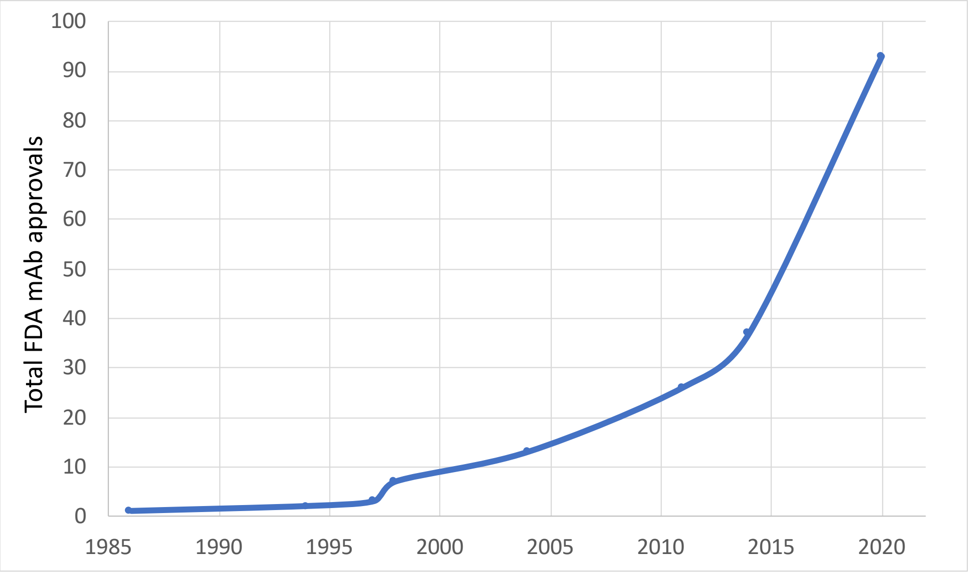

Figure 1.1: The total number of monoclonal antibodies (mAbs) by year. *Rapid increase in the number of United States Food and Drug Administration (FDA) approved mAb therapeutics by year, with a total of 93 mAbs by 2020.*

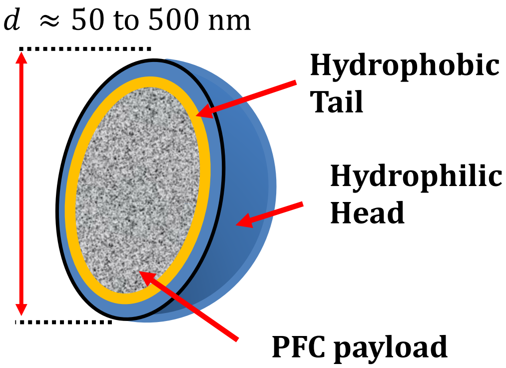

Figure 1.2: Illustration of a PFC loaded nanoemulsion. *Graphical depiction of a PFC loaded nanoemulsion where the PFC payload is encapsulated within an emulsifier of a diameter is between 50-500 nm.*

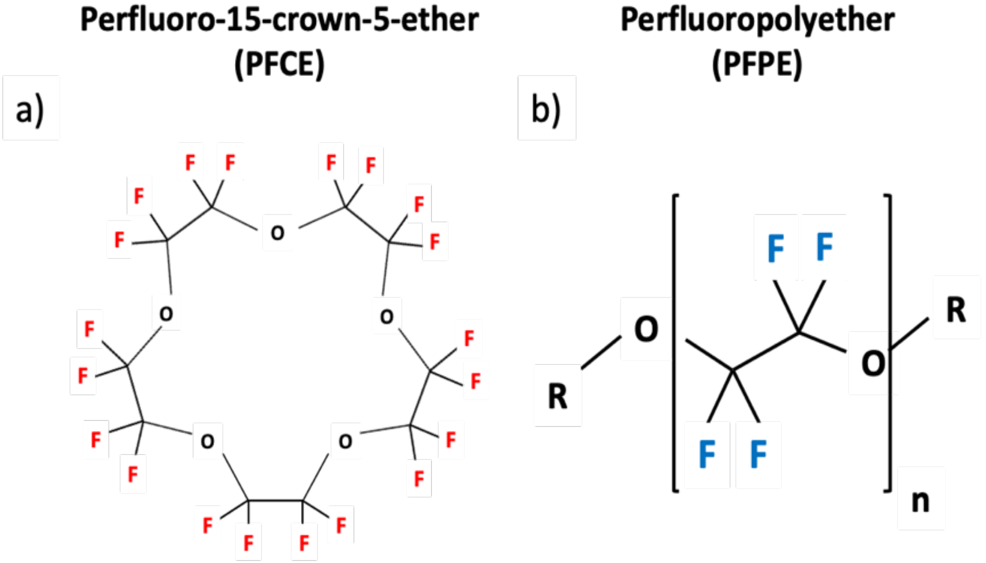

Figure 1.3: Chemical structure for two common ^{19}F MRI agents. *The chemical structure for (a) cyclic perfluoro-15-crown-5-ether (PFCE) and (b) linear perfluoropolyether (PFPE).*

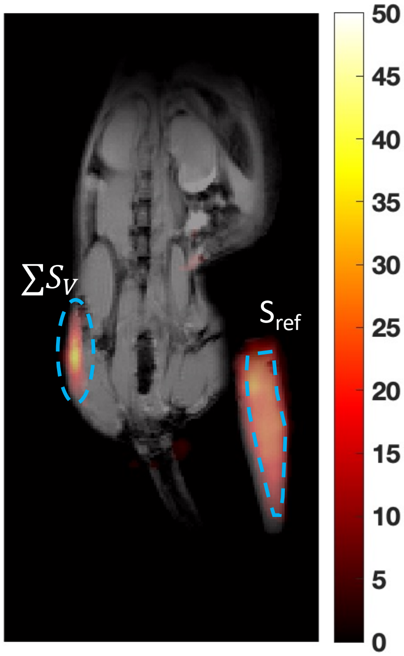

Figure 1.4: ^{19}F MR-image quantification example. *Composite ^{1}H (grayscale)/^{19}F ("hot iron" color scale) coronal image of a mouse after subcutaneous labeled cell injection, demonstrating an example of ROI selection for the quantification process to determine total signal from labeled cells, $\sum S_V$, and average signal in the reference vial, S_{ref}.*

Chapter 2 CHARACTERIZATION AND DETECTION OF MURINE T CELLS: FEASIBILITY AND TROUBLESHOOTING

Additional Contributors: Wonjong Jin, PhD; Zachary Morris, PhD MD

2.1 Abstract

Purpose: The purpose of this work was to 1) Characterize the effects of PFPE-labeling on murine T cells and determine an *in vivo* detection limit, 2) develop quality-assurance techniques to improve PFPE label consistency and validate intracellular uptake, and 3) apply ^{19}F MRI T cell tracking to a cancer vaccine model.

Methods: CD3+ T cells were isolated from male B6 mice and labeled with varying concentrations of PFPE- red for set periods of time, *in vitro* assays were performed to characterize any detrimental effects due to labeling, and uptake was confirmed via flow cytometry. Afterward, 2 aliquots of the labeled T cells were prepared at varying cell counts and injected subcutaneously into separate sites, and imaged with ^{1}H/^{19}F MRI, where a detection limit was extrapolated from the signal at the injection sites. Quality assurance techniques with confocal microscopy and ^{19}F nuclear magnetic resonance (NMR) were implemented to ensure proper and consistent labeling.

Results: Flow cytometry indicated that a labeling concentration of 4 mg/mL for 16 hours resulted in the greatest fluorescent signal within the CD3+ murine T cells without inducing detectible changes in phenotype, function, or viability. Fluorine-19 MRI demonstrated the ability to detect both of the injection sites with an approximate detection limit of 5.1×10^5 T cells. Implementation of confocal imaging and NMR techniques allowed for rapid determination of labeling success and quantification of PFPE-red uptake within T cells.

Conclusion: Flow cytometry results demonstrated minimal detrimental impact on T cell viability and function. Quality assurance implementation allowed for rapid confirmation and quantification of PFPE-red label uptake into murine T cells. Furthermore, feasibility of cellular detection via ^{19}F MRI was demonstrated and an *in vivo* detection limit was established. However, we also found

that the current cellular detection limit precludes its use in the proposed metastatic melanoma model.

2.2 Introduction

Accurate detection and quantification of effector cells delivered in Adoptive Cell Therapies (ACT) would enable *in vivo* assessment of immunotherapies, which may improve its efficacy.[78] Imaging modalities such PET[79,80], SPECT[81,82], and optical imaging (OI)[83] have established methods to image immune cells *in vivo*. These modalities offer great utility in cellular tracking studies but have some limitations. PET/SPECT modalities rely on ionizing radiation and have a short imaging window due to radioisotope decay, which precludes its use for repeated long-term imaging studies. OI techniques are very useful in preclinical mouse models but are not clinical viable due to limitations in the depth of penetration *in vivo*.[84]

Several MRI methods have been developed as viable non-ionizing radiation techniques for cellular tracking that do not suffer from depth of penetration issues.[85] One particular MRI approach utilizes excitation of fluorine-19 (^{19}F) nuclei to track exogenously perfluorocarbon (PFC) labeled immune cells over the course of days to weeks post injection. The low endogenous fluorine concentration naturally found *in vivo* results in images with negligible background, which leads to an unambiguous positive contrast signal.[86,87] Fluorine-19 MRI is particularly attractive as a cell tracking technique due to its high specificity and the ability to precisely and accurately quantify cells directly from the resultant ^{19}F images.[63,88] However, as a developing cell tracking method, cross-validation is essential to its continued progress and translation. Testing and validation of the PFC nanoemulsion uptake into the cells, intracellular label retention post-infusion, characterization of labeling effects on viability, phenotype, and cell function, and quality assurance testing need to be considered for future translational studies.[74,89]

In recent years, ACT using various forms of T cells have shown success in the treatment of multiple forms of refractory cancers.[23,90] T cell lymphocytes are members of the adaptive immune system, which is responsible for creating a long lasting immunity to previously encountered antigens or pathogens. One immunotherapy strategy is to target particular tumor specific antigens (TSAs), or tumor associated antigens (TAAs) in order to elicit a vaccination-like response. This approach is enticing, given the theoretical possibility of producing lifetime immunity against particular cancers; however, this approach is difficult due to our inability to elicit an effective adaptive immune response from TSAs and TAAs.[91,92]

Of interest for this thesis project is an approach that looks to create a therapeutic cancer vaccine for metastatic melanoma. More specifically, this novel approach looks to combine radiation therapy, IL-2 linked TSAs, and anti-cytotoxic T lymphocyte-associated antigen-4 (CTLA-4) to elicit an *in-situ* vaccine response that has been shown to increase survival in mice and eradicate large tumors and metastases.[93] To further improve understanding this cancer vaccine model, the foundational work for cellular tracking of T cells was developed. The purpose of the work presented in this chapter was 3-fold. 1) Characterize the *in vitro* effects of labeling murine T cells with perfluoropolyether (PFPE), and determine an *in vivo* cellular detection limit, 2) develop quality-assurance techniques to improve PFPE label consistency and validate intracellular uptake, and 3) apply ^{19}F MRI T cell tracking to a murine cancer vaccine model.

2.3 Methods

2.3.1 ***Study Design***

This research project design is divided into a two main sections: 1) foundational work to establish a workflow for evaluation, quality assurance, and troubleshooting and 2) application in a metastatic melanoma cancer vaccine model. A graphical depiction of this study can be seen in Figure 2.1.

2.3.2 ***Quality assurance protocol***

After several unsuccessful experiments, a quality assurance protocol was implemented to ensure efficient use of resources and to improve overall experimental success. The first issue addressed the overall shelf-life of the commercially available ^{19}F contrast agent of choice, PFPE

(Celsense Inc; Pittsburgh, PA). PFC nanoemulsions are not thermodynamically stable, but instead kinetically stable, which results in increased particle size over time due to Ostwald Ripening.[94] Increased particle size can cause changes in true particle uptake into the cells and sedimentation in culture that will inhibit the ability to remove unbound agent with centrifugation, which can lead to false positive cell signals.[74,95] Thus, adherence to a conservative shelf life of less than 3 weeks for an opened vial of agent was enforced to ensure minimal changes in particle size during its experimental usage. The second issue addressed was the large variability in PFC-label uptake that can be seen within T cells. To ensure that sufficient cell uptake has been achieved, ^{19}F NMR was enacted prior to *in vivo* cell delivery to serve as pass/fail test based upon the amount of average ^{19}F nuclei/cell in the test sample. The criterion for passing was enforced to be ±1 standard deviation from the previously determined average label uptake, $\overline{F_c}$.

2.3.3 *T cell isolation and expansion*

To begin, the spleens of male B6 mice were isolated and single cell dissociation was performed using a 70 μm pore cell strainers with 5 mL of RPMI media. Cells were then transferred to a 50 mL centrifuge tube and centrifuged for 5 minutes at 2000 RPMs at 4 °C. Supernatant was then discarded, and the cells were resuspended in 4 mL of phosphate buffered saline (PBS). Cells were washed again, and 4 mL of Red Blood Cell (RBC) lysis buffer was added to deplete erythrocytes. Cells were then incubated at room temperature for 3 minutes, then 10 mL of PBS was added, and cells were once again centrifuged. Afterwards, T cells were sorted using a Pan T Cell Isolation kit and a magnetic activation cell sorting (MAC) method. Cells were then cultured in triplicate on 48-well plates at 2×10^6 T cells per 500 μL per well with K10 media and IL-2.

2.3.4 *T cell labeling and characterization*

To determine ideal PFPE-red incubation concentration and time for the cells of interest, samples of expanded CD3+ T cells will be incubated in triplicate with 0 (control), 1, 4, and 10 mg/mL of PFPE-red (CS-1000 DM Red, Celsense Inc; Pittsburgh, PA) for 1, 4, and 12 hours. After the allotted labeling time, cells were transferred to 1.5 mL centrifuge tubes, and centrifuged at 2000 RPMs for 5 minutes at 4 °C. The supernatant was then discarded, and cells were resuspended in 1 mL of PBS. This washing step was repeated an additional 2 times to ensure the removal of residual PFPE-red agent and then the cells were counted. Live T cells from this experiment were assessed via the 450 nm optical density (OD450) using a SpectraMax i3 microplate reader (Molecular Devices; San Jose, CA). In separate experiments T cells were labeled in triplicate with 0, 2, 4, and 10 mg/mL of PFPE for 16 hours were then stained with 20 μL of 10 μM DAPI nuclei stain. The viability of labeled T cells was then assessed relative to their respective control, via flow cytometry. Relative labeling intensity was further explored by recording the median fluorescent intensity (MFI) for T cells labeled in triplicate with 4 mg/mL for 1, 12, and 16 hours.

Flow cytometry was also utilized to quantify the impact of 16-hour labeling with PFPE-red at 2, 4, and 10 mg/mL on the expression of CD4 and CD8 in CD3+ T cells. And lastly, interferon gamma (IFN-γ) release was explored with flow cytometry as an additional metric for T cell function. The IFN-γ release measurements were performed using CD3+ T cells cocultured with either 8Gy irradiated B78 melanoma target cells, or non-radiated B78 cells. T cells were either unlabeled or labeled with 4 mg/mL of PFPE-red for 24 hours.

2.3.5 ***PFPE Label validation and quantification***

2.3.5.1 Confocal Microscopy

Validation of the PFPE-red labeling was performed via a Nikon A1RS confocal microscope (Nikon, Tokyo, Japan), where a subset (<1.0 x10^6 cells) of labeled T cells was stained via Hoechst 33342 for 15 minutes and placed in 8-well glass-bottom microscope slides (Ibidi USA inc, Fitchburg, WI) in duplicate. Microscopy images were then be acquired with the red (BODIPy) and blue (Hoechst) laser excitation. Red and blue channel images were processed with ImageJ and composite images were generated. These composite images were used as a visual confirmation of intracellular PFPE-red labeling in the T cells.

2.3.5.2 ^{19}F nuclear magnetic resonance

To quantify cellular uptake (^{19}F nuclei/cell), a subset of the labeled T cells were then prepared for ^{19}F NMR analysis at the end of their labeling period. Samples were washed three times, as previously described, counted, and pelleted (1.0-3.0 x 10^6 cells/sample). Pelleted T cell samples were lysed by resuspending the pellet in 125 µL of 1% Triton X-100 lysing agent diluted in deuterium-oxide (D_2O) and 125 µL of 0.1% trifluoroacetic acid (TFA) in D_2O. The known volume of TFA serves as both a ^{19}F chemical shift and a quantification reference. Cell lysate solutions were then transferred to 400 MHz 5 mm NMR tubes (Wilmad-Labglass, Vineland, NJ). ^{19}F spectra were acquired on a 9.4T (400 MHz) NMR spectrometer (Avance III HD, Bruker, Billerica, MA) with a 12 second recycle delay (TR), 90° flip angle, and 64 transients (averages). Following Equation 2.1, the resulting cellular labeling density, F_c, of each sample will be calculated as:

$$F_c = \frac{3(I_c)(M_r)(N_\mathrm{A})}{(I_r)(N_c)} \tag{2.1}$$

Where I_C and I_r are the integrated areas under the peaks of our cellular label and reference peaks located at -91 and -76 ppm, respectively; M_r is the moles of TFA reference, N_c is the number of lysed cells in the sample, and N_A is Avogadro's number. The optimal labeling time was chosen based on the greatest mean labeling density, $\overline{F_c}$, that doesn't significantly impact cellular viability and function relative to the control group.

2.3.6 *In vivo MRI and post-processing*

2.3.6.1 In vivo cell concentration detection limit

To determine a cellular detection limit using naïve T cells labeled at 4 mg/mL for 12 hours, a male B6 mouse was injected subcutaneously in two locations on the abdomen with either

3.0×10^6 or 1.5×10^6 PFPE-red labeled T cells in 100 μL. After injection, mice were placed under 1.5% ISO anesthetic at 1.0% O_2 and placed prone into the $^1H/^{19}F$ volume coil. A warm-air blower was placed near the mouse along with a temperature probe to ensure the subject temperature was maintained at 37 °C. MR images were acquired using a 4.7T horizontal bore small animal system (Agilent Technologies; Santa Clara, CA). Anatomic imaging was performed using a T_2-weighted FSE sequence with a FOV of 72x36 mm with 2 mm slices, reconstruction matrix of 64x32, TR/TE = 3000/20 ms, and an ETL=16. ^{19}F images were acquired using a FSE sequence partially optimized with respect to SNR temporal efficiency with FOV and slice thickness matched to the T_2-weighted proton acquisition, a reconstruction matrix of 64/32, TR/TE = 1250/20 ms, ETL = 8, and a NEX = 300 for a total scan time of 25 minutes. A chemical saturation pulse situated at +2150 Hz was also added to remove isoflurane contamination.

Resultant images were reconstructed and analyzed using region-of-interest (ROI) analysis via MATLAB 2018b (Mathworks; Natick, MA). First, a noise measurement was taken in a background region devoid of true signal, and the mean noise value, $\overline{N}$, was corrected for its Rayleigh-distributed noise, as indicated in Equation 2.2, to arrive at an unbiased estimate of the noise, σ_g.

$$\sigma_g = \sqrt{\frac{2}{\pi}}\overline{N} \tag{2.2}$$

Each image slice was then scaled against its noise and thresholded at an SNR = 4 to avoid contribution from noise. ROIs were manually drawn over the signal injection sites to determine the average signal within the region. Assuming a minimum threshold SNR of 4, the average SNR from each injection site was plotted against known cell number and a linear regression was performed to extrapolate the minimum detectible cell concentration (cells/voxel) for the given protocol.

2.3.6.2 Intravenous detection of TSA T cells in bilateral melanoma

To investigate T cell trafficking in the previously described cancer vaccination model proposed by Morris et al.[93], intravenous T cell detection was explored in a melanoma model. CD3+ T cells were isolated, as previously described, from previously "vaccinated" B78 tumor bearing mice, and labeled with PFPE-red at 4 mg/mL for 12 hours. Prior to injection of the labeled T cells, the recipient tumor-bearing mouse received the combination treatment of radiation therapy on the right flank tumor, and injection of anti-CTLA-4, and IL-2 linked TSAs, hereafter referred to as "vaccinated". The vaccinated B6 mouse with bilateral B78 melanoma tumors was given a tail vein injection of 4.0×10^6 labeled T cells. Immediately after injection (day 0) the mouse was anesthetized and placed prone into the $^1H/^{19}F$ volume coil. To serve as a ^{19}F chemical shift reference, a vial of PFPE was placed on the left side of the mouse hind legs. Anatomic imaging was performed using a T_2-weighted FSE sequence with a FOV of 72x36 mm with 2 mm slices, acquisition matrix of 64x32, TR/TE = 3000/20 ms, and an ETL=16. ^{19}F images were acquired using the previously described FSE sequence partially optimized with respect to SNR and acquisition time with matching FOV and slice thickness to the T_2-weighted proton acquisition, a acquisition matrix of 64/32, TR/TE = 1250/20 ms, ETL = 8, and a NEX = 300 for a total scan time of 18.75 minutes. Mice were imaged again on day 7 post injection.

2.4 Results

2.4.1 *T cell isolation and expansion*

CD3+ murine T cells, stained with the anti-CD3 monoclonal antibody with a conjugated FITC fluorophore, were successfully isolated at high efficiency. With the positive sorted population being CD3+ at 93.3%, and 97.3% of the negative sorted T cell population being CD3-, as indicated by flow cytometric analysis shown in Figure 2.2. Furthermore, as seen in Figure 2.3, successful T cell expansion was seen out to 12 days, with over a 5-fold increase in live cell count after day 8 and an overall increase in cell viability after day 1.

2.4.2 *PFPE-label characterization*

2.4.2.1 Viability and function effects

The *in vitro* effects of both PFPE-red labeling time and dose on T cell viability was quantified in Figure 2.4A, where similar viability was seen across all three time points for 1 and 4 mg/mL relative to control. However, a significant reduction in viability was seen with a labeling concentration of 10 mg/mL for all incubation durations. The secondary measurements in viability, shown in Figure 2.4B, followed a similar trend that demonstrated that 0, 1, and 4 mg/mL of PFPE-red incubation for 16 hours did not have a measurable effect on T cell viability, but 10 mg/mL did result in a significant reduction in viability, relative to control. The BODIPy-TR MFI for T cells labeled at 4 mg/mL for multiple time points, shown in Figure 2.5, indicated an increased relative uptake of PFPE-red into the T cells with time, which suggests that labeling with 4 mg/mL for 16 hours would produce the greatest intracellular signal uptake without unacceptable reduction in cell viability.

While viability was shown to be preserved in T cells labeled at 0 to 4 mg/mL, expression of T cell markers CD4 and CD8, and IFN-γ were also measured to ensure viable cells remain functional. As shown in Figure 2.6, CD3+ T cells showed no detectible differences in their expression of CD4 or CD8 for labeling concentrations of 0, 1, 4, and 10 mg/mL of PFPE-red for 20 hours. Furthermore, quantification of CD4+ and CD8+ T cell function after PFPE-labeling, shown in Figure 2.7B-C, indicated no significant changes in IFN-γ production in either the irradiated or non-irradiated PFPE-red labeled group, compared to control. Together, the results of these 4 tests suggest that T cell labeling with PFPE-red at 4 mg/mL for 16 hours will not result in measurable changes in T cell viability or function.

2.4.3 *Labeling validation and quantification*

To verify intracellular uptake of the PFPE-red label into CD3+ T cells, confocal microscopy was performed and independently verified using flow cytometry for cells labeled for

16 hours at 4 mg/mL. The confocal microscopy results, shown in Figure 2.8A, show PFPE-red (Texas Red) fluorescence surrounding the DAPI blue stained nucleus of CD3+ T cells. The flow cytometry histograms and corresponding MFI, shown in Figure 2.8B, from the labeled T cells indicate the intracellular presence of PFPE-red. To quantify the mean fluorine nuclei content within T cells labeled at 4 mg/mL for 16 hours, ^{19}F NMR was performed on triplicate samples of 1.0×10^6 lysed T cells. The NMR spectra, displayed in Figure 2.9, successfully show the TFA and PFPE main peaks at -76 and -91 ppm, respectively. Integration of the respective peaks reveal an average PFPE-red uptake of $5.5 \pm 0.3 \times 10^{11}$ ^{19}F nuclei/cell.

2.4.4 *In vivo cell detection limit*

After labeling T cells for 16 hours at 4 mg/mL with PFPE-red, cells were injected subcutaneously, as previously described to determine an approximate cell detection limit. The resulting composite anatomic, fluorine, and ^{1}H/^{19}F images, shown in Figure 2.10, indicate successful detection of both injection sites along the mouse abdomen in multiple slices. ROI analysis of the injection sites indicated an average SNR of approximately 8.5 ± 1.1 and 14.3 ± 1.3 within the 1.5×10^6 and 3.0×10^6 T cell injection sites, respectively. The linear regression (Figure 2.11) of the data indicates that a cell detection limit, defined conservatively at a cut off of SNR = 4, results in a cell detection limit of approximately 5.1×10^5 T cells, under the prescribed imaging protocol and T cell preparation.

2.4.5 *In vivo detection in melanoma model*

Detection and tracking of T cells for a week within a bilateral B78 melanoma model was tested. The resulting images (Figure 2.12), show successful detection of ^{19}F signal near the left axillary lymph node at days 0 and 7 post injection. On day 7, signal was also detectible in the right axillary lymph node, suggesting migration of the T cells from days 0 to 7. However, no signal was detectible within either tumor in the mouse at days 0 or 7.

2.5 Discussion

In this project, the methodology was presented to characterize, quantify, and validate murine T cell labeling with a common ^{19}F contrast agent, PFPE. This workflow determined the efficiency of T cell isolation and expansion and the effects of PFPE-red labeling on viability, function, and expression. The ideal incubation time and dose to improve label uptake without detrimental effects was also determined to be 4 mg/mL for 16 hours. The label uptake under these conditions was both quantified and verified via confocal microscopy and ^{19}F NMR spectroscopy. Furthermore, this work determined a conservative *in vivo* cell detection limit of 5.1×10^5 T cells and demonstrated the feasibility to track these cells out to a week post injection via ^{19}F MRI.

Various types of T cells are currently being implemented and explored as a therapeutic agent in cancer immunotherapies. Employing cellular imaging techniques to detect and track these effector T cells after delivery would allow *in vivo* efficacy assessments and biomarker development, which may improve its effectiveness[78] and translatability from preclinical animal models to clinical trials in humans. This would enable clinicians to determine how long the effector cells persist *in vivo*, where they migrate to, and reveal trafficking patterns that can help improve treatment strategies.

While detection of PFPE-red labeled T cells was successful in both a subcutaneous and IV model, we were unsuccessful at detecting cells within the tumors. This inability can be attributed to the relatively small PFPE-red uptake into the T cells, which have intrinsically low phagocytic capacity[64,74] compared to other immune cells such as NK cells. Although the average ^{19}F uptake per cell shown in this study was within the range seen in the literature, which varies by up to 100-fold[96], the achieved sensitivity was insufficient to allow more minute detection *in vivo*. One simple strategy to improve our detection ability would be to increase the number of injected T cells; however, the biological effects of delivering large numbers of effector cells may preclude its use in particular treatment models, such as the aforementioned metastatic melanoma vaccine model.

One viable method to improve sensitivity would be to include a transfecting agent, such as FuGENE, or electroporation as an additional labeling treatment to increase ^{19}F uptake into the cells, which has demonstrated an average T cell labeling on the order of 10^{13} fluorine nuclei per cell.[63] This transfecting method did not appear to show any differences in viability or function, but did cause a transient change in CD4 expression. Authors suggested this temporary CD4 reduction during labeling could be due to receptor-mediated endocytosis (RME) mechanisms being utilized during transfection treatment, which has been shown to reduce CD4 expression during this process.[97] Additionally, to improve the success of this preclinical model, higher field strength systems (e.g. >=7T) could provide a significant increase in SNR, which would lower the cell detection limit proportionally.

In conclusion, while the overall aim to track T cell migration to B78 melanoma tumors was unsuccessful, this research provided 2 significant contributions that aided our future endeavors. First, the development and implementation of a quality assurance protocol enabled us to detect cell viability or labeling complications prior to *in vivo* delivery. This step enabled us to detect and rectify flaws in the labeling methodology (i.e., PFPE sedimentation or incomplete cell lysis), and reduce the loss of resources, such as paid scanner time and agent waste. Second, the development of a labeling workflow with validating steps has allowed us to expand this process to various cell types, such as CAR T cells, stem cells, NK cells, and monocytes, that have shown promise in various preclinical and clinical applications.

2.6 Acknowledgements

This project was a collaborative effort led by Drs Zach Morris and Sean Fain. Postdoctoral researcher, Dr. Wonjong Jin, conducted the bulk of the wet lab work such as T cell expansion, labeling, tumor inoculation, and *in vitro* assays. Dr. Jin also provided his expertise in oncology and cellular biology to assist in the interpretation of the experimental results. My (Lawrence Lechuga) responsibilities and contributions were to 1) validate and quantify cellular labeling

through development of confocal microscopy and NMR spectroscopy techniques, 2) design, gather, and process *in vivo* fluorine MRI data of mice, 3) develop a quality assurance protocol for *in vivo* imaging of labeled cells, and 4) provided my imaging expertise to assist in the interpretation and design of the study.

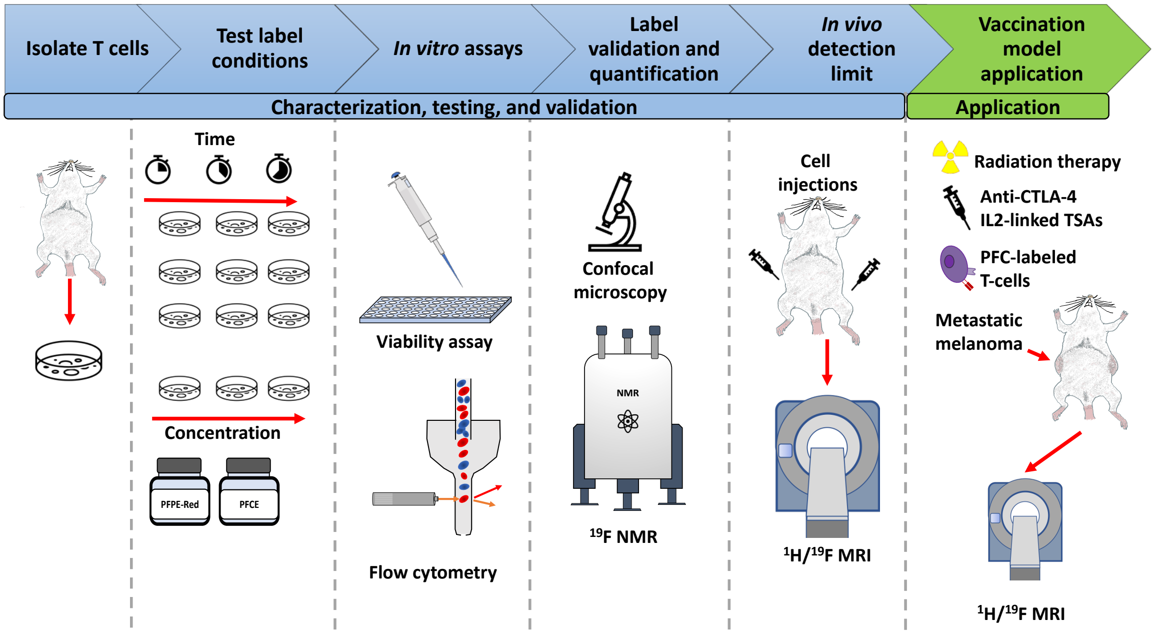

Figure 2.1: Graphical depiction of the study design. *A graphical outline of the tasks performed to characterize and develop a ^{19}F MRI cell tracking platform for murine T cells and application in a cancer vaccine model.*

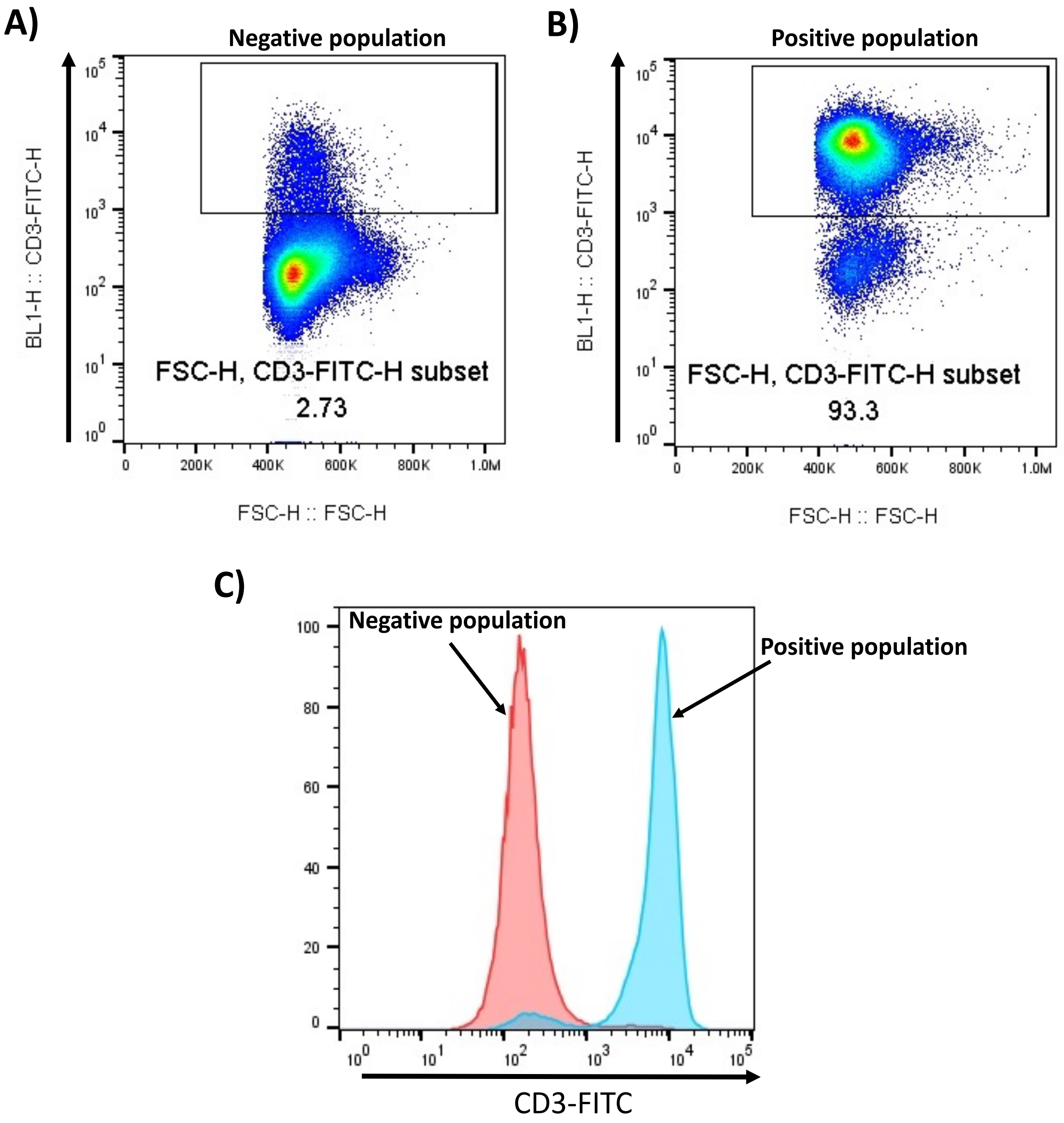

Figure 2.2**: **Assessment of T cell sorting efficiency by flow cytometry. *Flow cytometry dot plots indicating (A) only 2.73% of the negative population displayed CD3 markers, while (B) the positive population was 93.3% CD3+, indicated high efficiency of T cell sorting. (C) Histograms demonstrate the fluorescent intensity of the negative (CD3-) and positive (CD3+) T cell populations.*

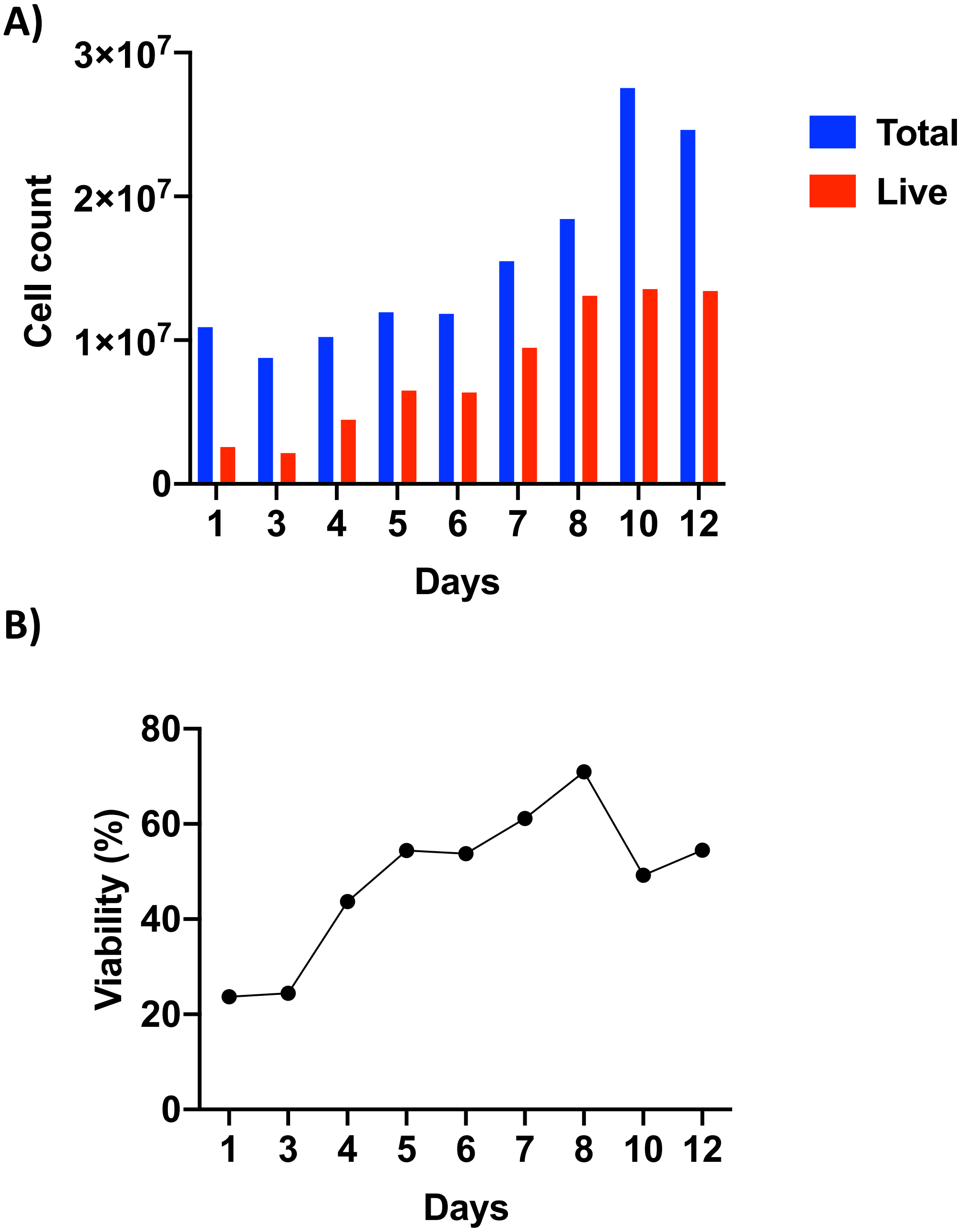

Figure 2.3: T cell expansion cell count by day. *A) Bar plot indicating total and live T cells in culture by day, using a Cell Counting Kit-8 (CCK8). A 5-fold increase in live cells were seen by day 8, and B) an increase in overall viability was seen at each time point relative to day 1.*

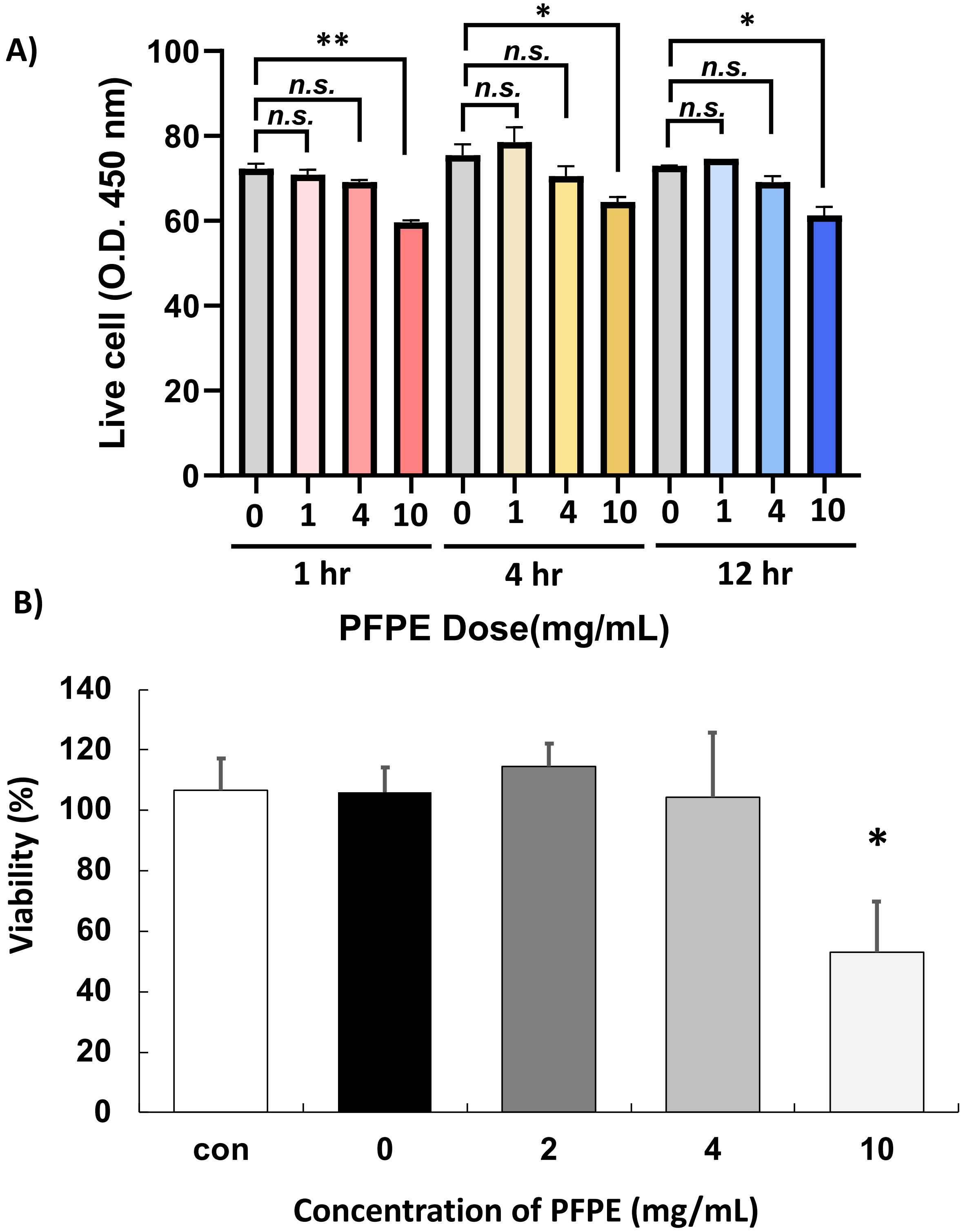

Figure 2.4: Viability of PFPE-labeled T cells across concentration and incubation duration. *Bar plots of the viability of CD3+ T cells, prepared in triplicate, after incubation in (A) 4 different concentrations of PFPE-red across 3 time intervals or (B) incubated across 4 different concentrations for 16 hours. No significant changes in viability were seen up to 4 mg/mL of PFPE-red across any timepoint; however, a significant reduction in viability was seen at an incubation concentration of 10 mg/mL at all time points, relative to control. Note: * = p-value < 0.05 and ** = p-value <0.01.*

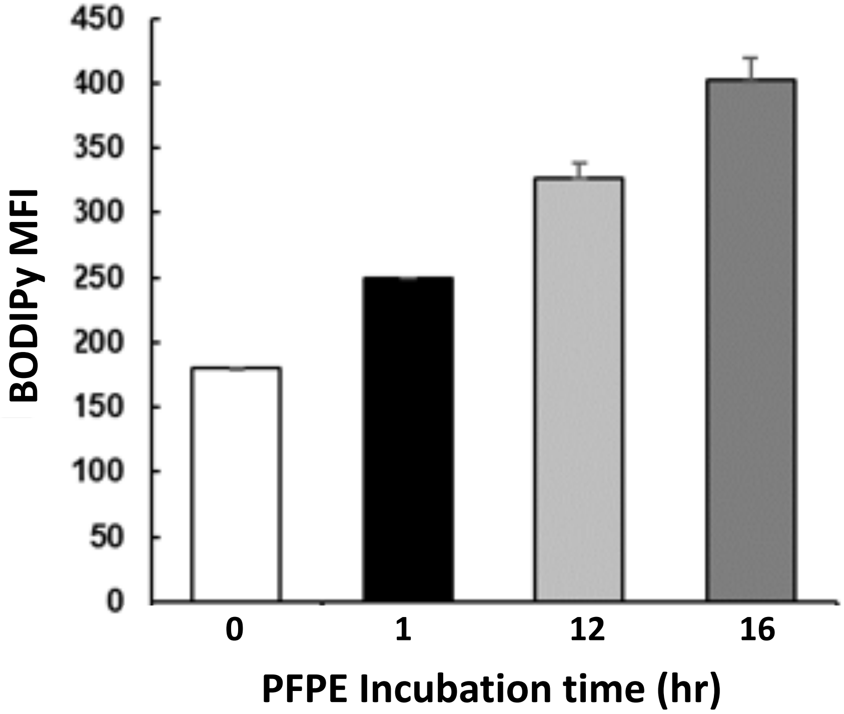

Figure 2.5: Assessment of relative PFPE-red labeling of T cells*. The MFI of PFPE-red labeled CD3+ T cells was recorded for 0, 1, 12 and 16 hours of total labeling time. Increased fluorescence was seen with increased labeling time, indicating stronger PFPE-red uptake with time.*

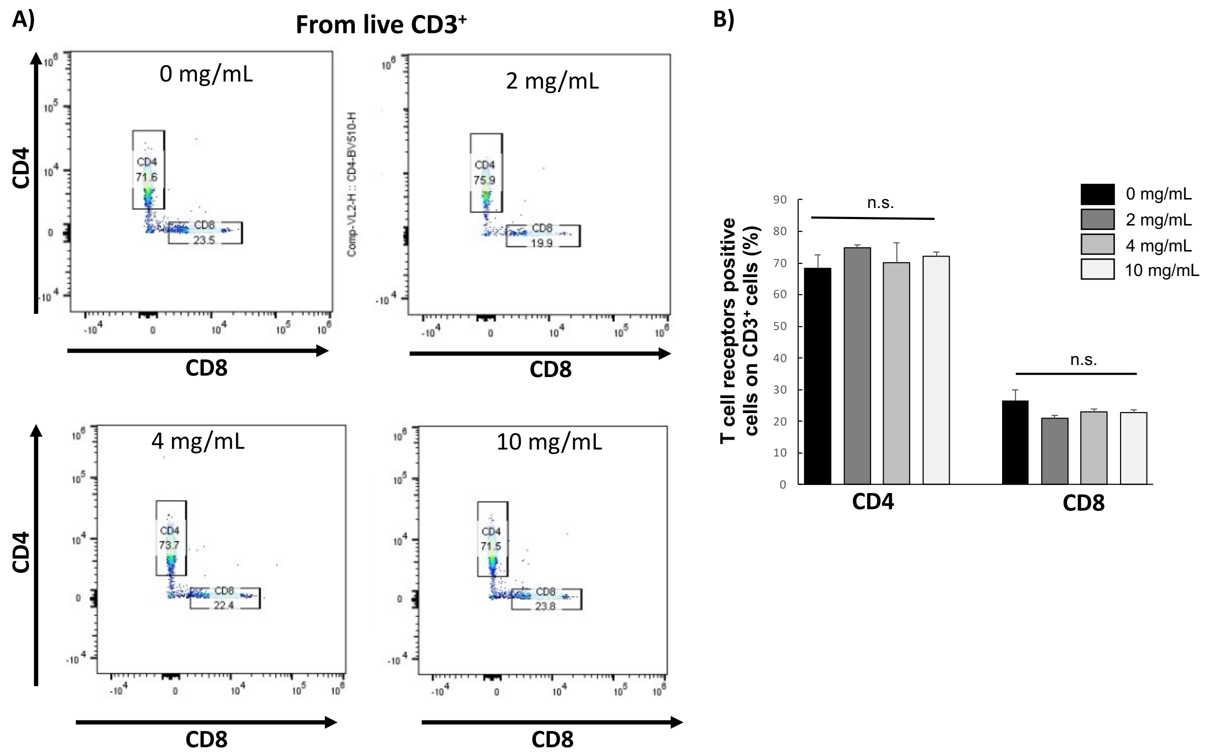

***Figure 2.6: PFPE-labeled T cell marker expression**. (A) Representative flow cytometry dot plots of CD4 and CD8 expression in CD3+ T cells (prepared in triplicate) after labeling with 0, 2, 4, and 10 mg/mL of PFPE-red for 20 hours. (B) As demonstrated in the bar plots, no significant changes in CD4 or CD8 expression were detectible. Note: n.s. = not significant.*

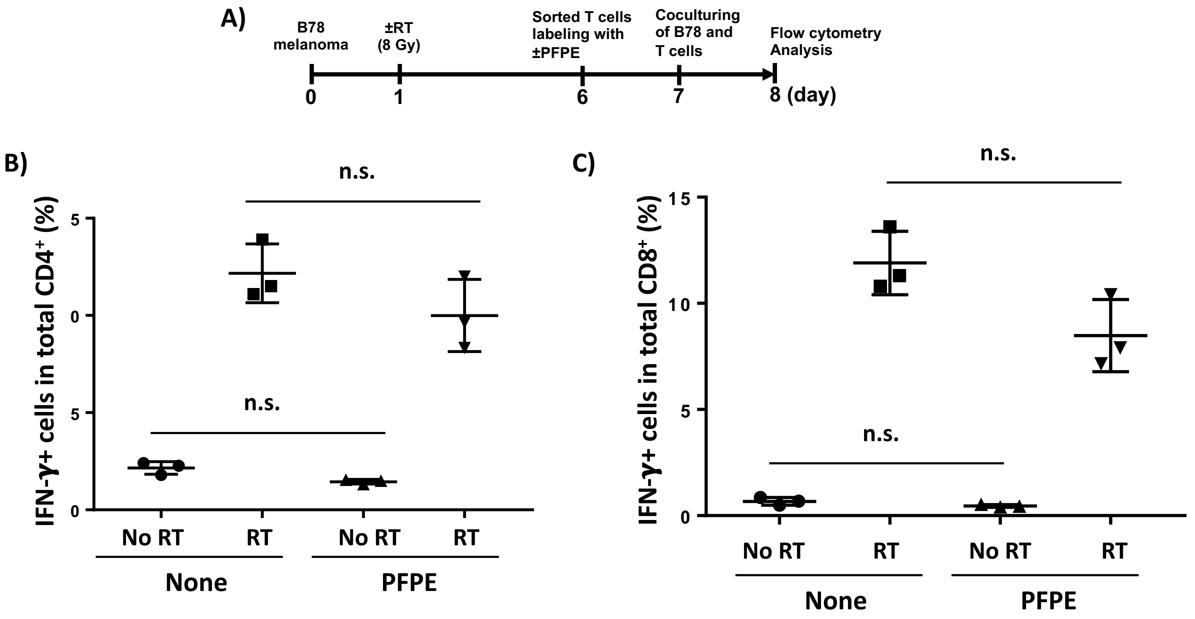

***Figure 2.7: PFPE-labeled T cells showed functional activity against radiated B78 melanoma**. Murine B78 melanoma cells were irradiated by 8Gy and cocultured with sorted T cells (±PFPE labeling, 4 mg/ml) at day 7. After 24h further incubation, the cells were determined internal IFNγ expression level using flow cytometry. The experimental scheme is shown along the top (A), IFNγ-positive cells in CD4 (B) and CD8 (C). n. s., no significance.*

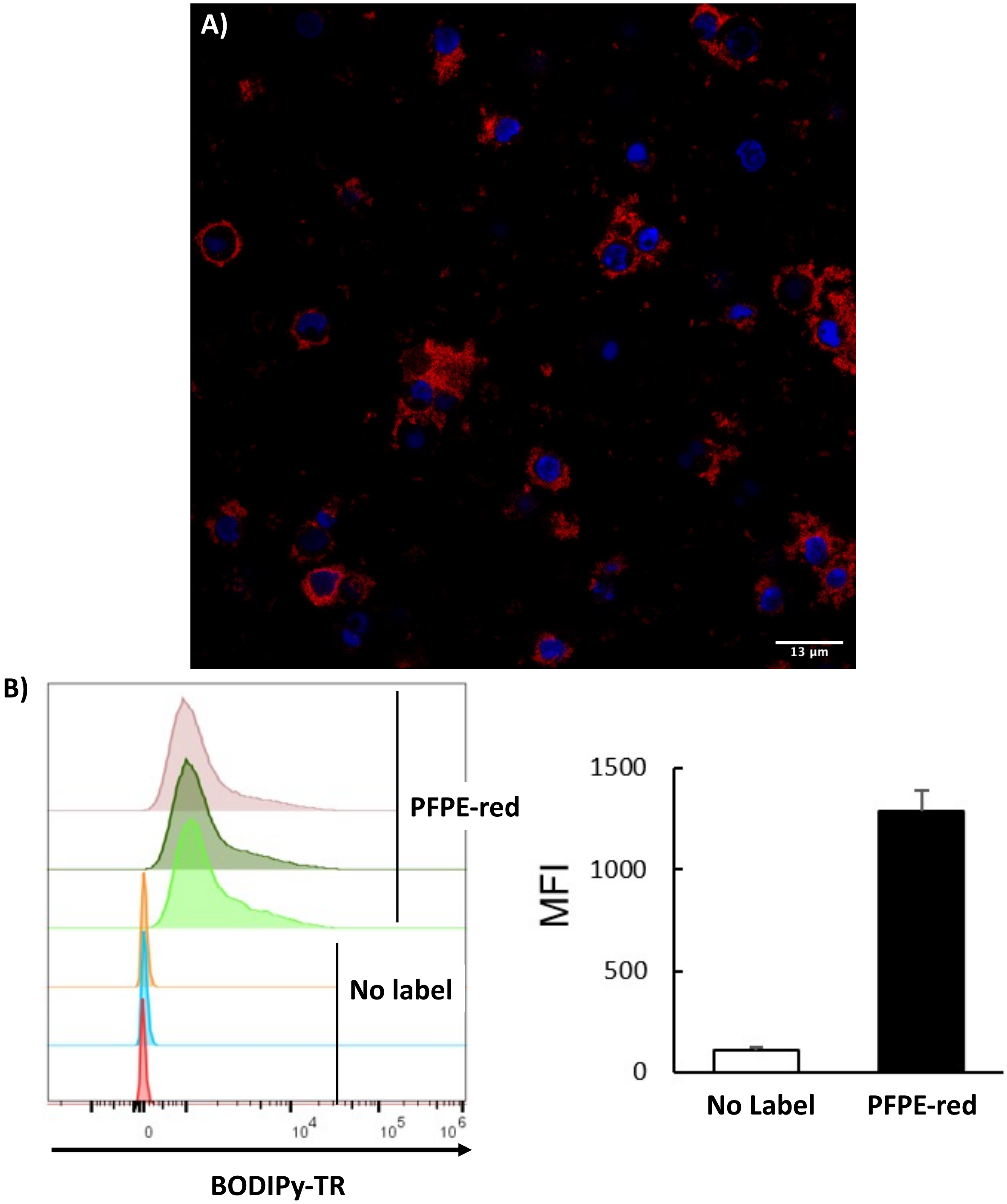

*Figure 2.8: **Cellular label validation via confocal microscopy and flow cytometry.** (A) Confocal microscopy (100x) of CD3+ murine T cells where Hoechst 33342 DNA-stain (blue) can be seen surrounded by PFPE-red label (BODIPY-red). Scale bar can be seen in bottom left corner for reference. (B) Histograms indicating fluorescent intensity along with the MFI for PFPE-Red labeled cells, compared to control, where labeling was performed at 4 mg/mL for 16 hours.*

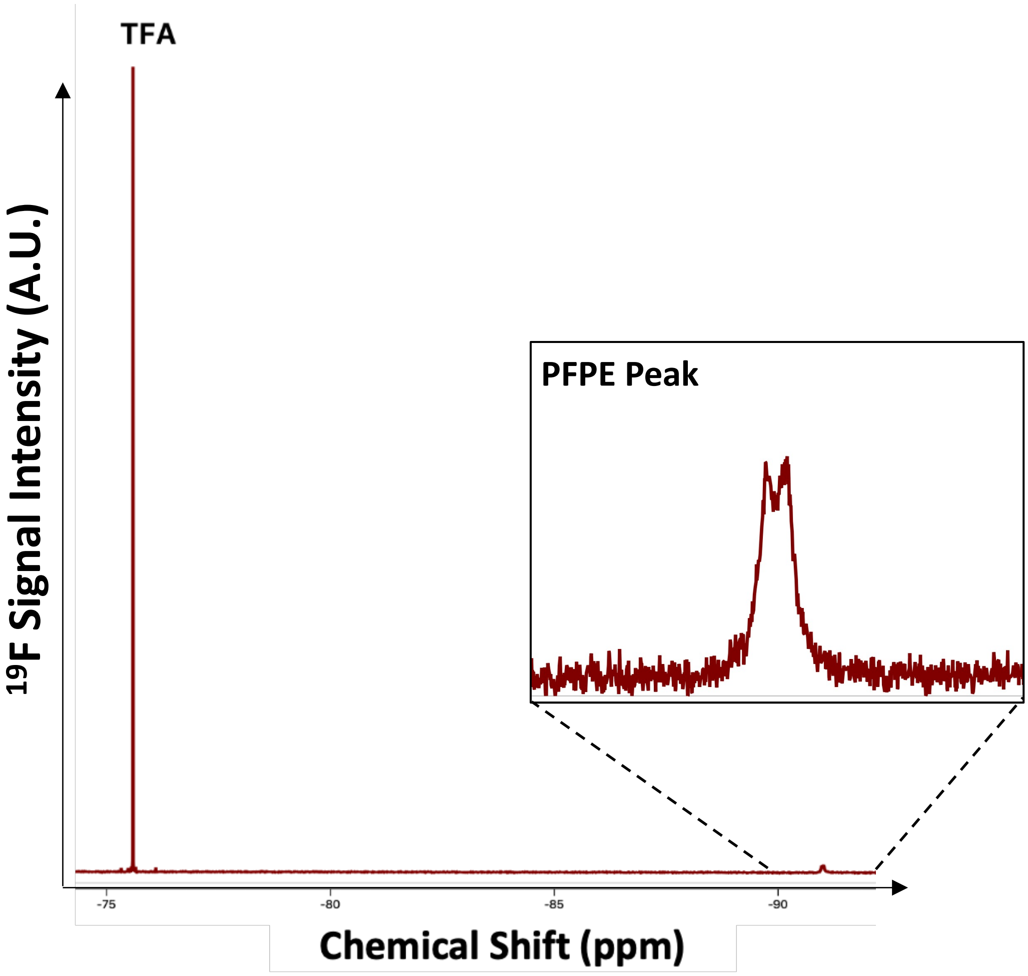

Figure 2.9: Nuclear magnetic resonance spectrum of lysed T cells. *Representative ^{19}F NMR spectrum of lysed PFPE-red labeled T cells. Trifluoroacetic acid (TFA)and PFPE peak are visible at -76 and -91 ppm, respectively. Integration of the peaks indicate a mean uptake of 5.5E11 ^{19}F nuclei/cell.*

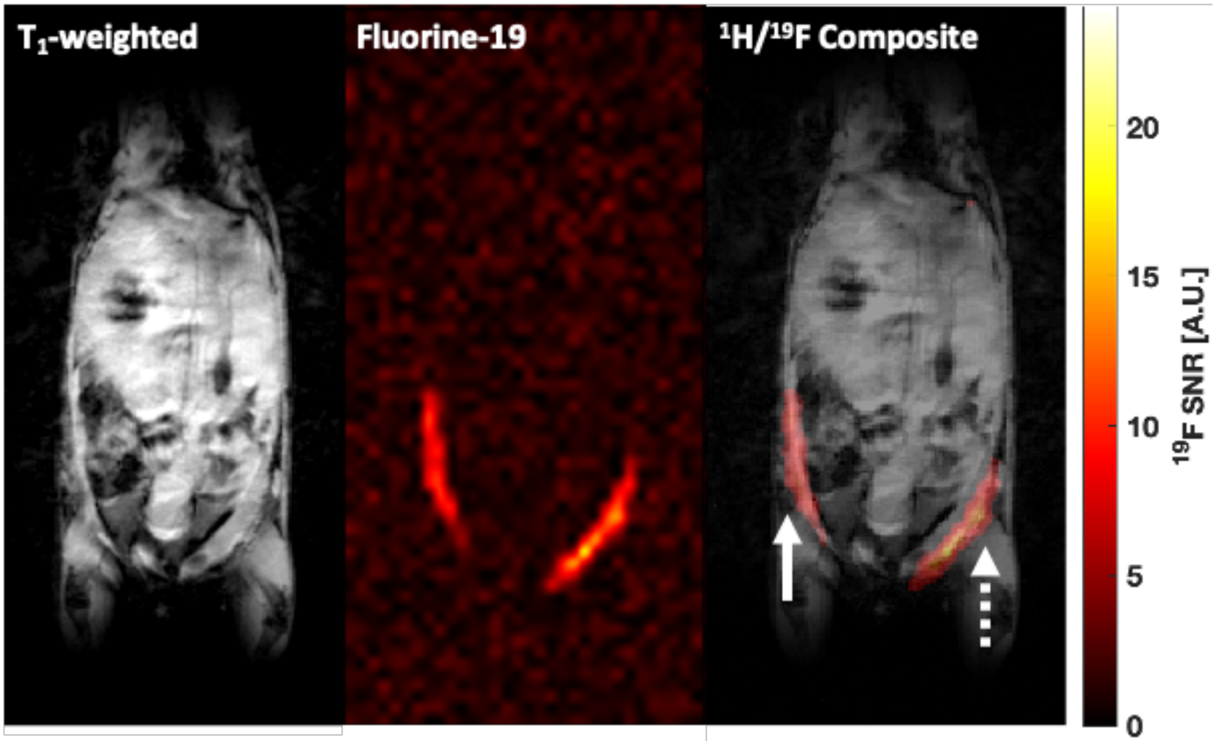

Figure 2.10: Representative composite $^1H/^{19}F$ image of T cell subcutaneous injected mouse. *A representative (left) anatomic, (middle) fluorine-19, and (right) composite coronal image slice of a B6 mouse injected in two locations with PFPE-red labeled T cells. The left site (solid white arrow) represents the 3.0E6 and the right (dashed white arrow) represent the 1.5E6 T cell injection sites, respectively.*

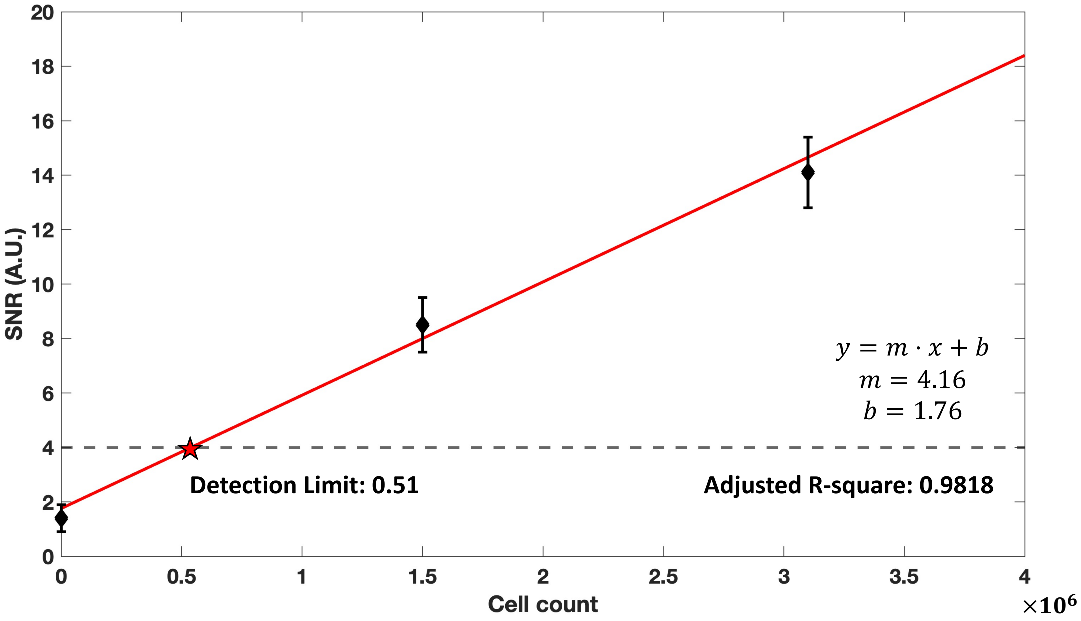

Figure 2.11: Linear regression of ^{19}F SNR versus injected T cell count. *A plot of the mean SNR within each of the two injections sites, where error bars represent the standard deviation in the ROI-derived values. A linear regression was performed (solid red line), and its intersection with the SNR cutoff = 4 (red and black star) indicates the approximate cell detection limit of 5.1E5 T cells, under the labeling and imaging protocol utilized.*

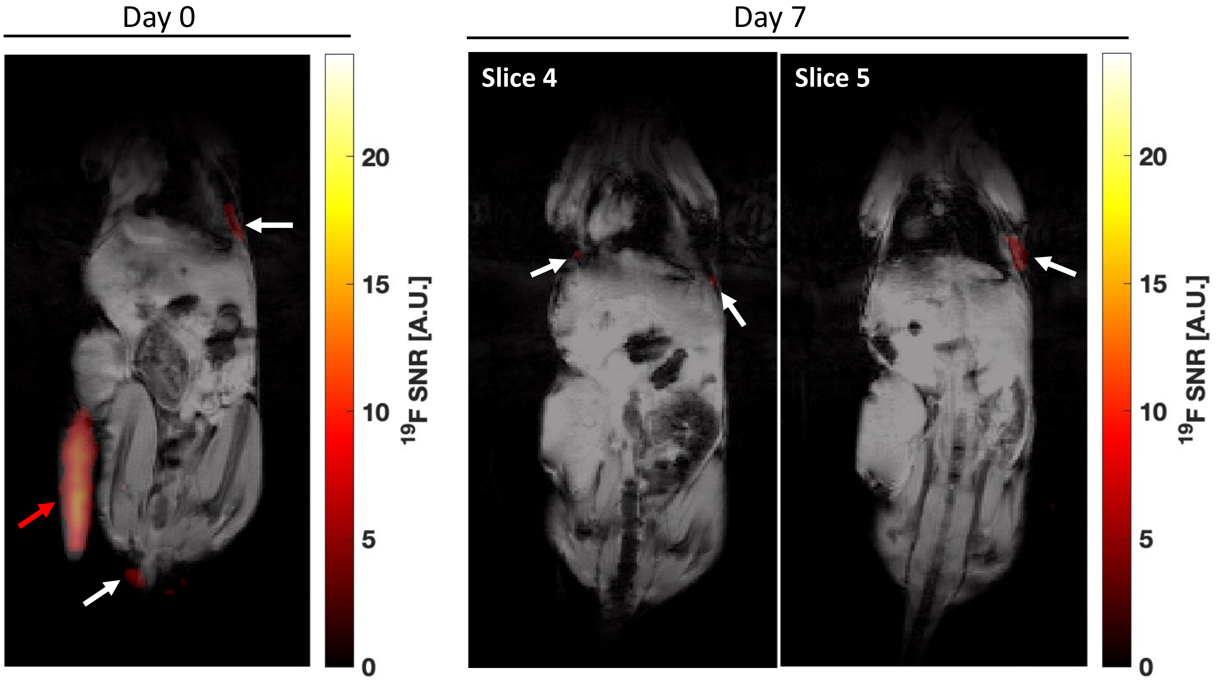

Figure 2.12: Representative composite ^{1}H/^{19}F image of IV injected tumor-bearing mouse at 2 time points. *Representative composite images of a mouse 2 hours (left) and 7 days (right) after IV delivery of 4.0E6 PFPE-red labeled T cells. White arrows indicate region of detected T cell signal in the lymph nodes and on the tail near the injection site. Red arrow denotes the location of the reference vial.*

Chapter 3 TRACK AND QUANTIFY PFC-LABELED GFP+ NATURAL KILLER CELLS IN A MURINE-LYMPHOMA CANCER MODEL WITH POST-MORTEM VALIDATION TECHNIQUES

Additional Contributors: Matthew Forsberg, PhD; Christian Capitini, MD

Note: This work was published in the NMR in Biomedicine in 2021 (Impact factor: 3.6).

3.1 Abstract

Natural Killer (NK) cell therapies are being increasingly used as an adoptive cell therapy for cancer because they can recognize tumor cells in an antigen-independent manner. While promising, the understanding of NK cell persistence, particularly within a harsh tumor microenvironment, is limited. Fluorine-19 (^{19}F) MRI is a non-invasive imaging modality that has shown promise in longitudinally tracking cell populations *in vivo*; however, it has not been studied on murine NK

cells. In this study, the impact of ^{19}F labeling on murine NK cell viability and function was assessed *in vitro* and then used to quantify NK cell persistence *in vivo*. While there was no noticeable impact on viability, labeling NK cells with ^{19}F did attenuate cytotoxicity against lymphoma cells *in vitro*. Fluorescent microscopy verified ^{19}F labeling in both the cytoplasm and nucleus of NK cells. Lymphoma bearing mice were given intratumoral injections of ^{19}F-labeled NK cells in which signal was detectable across the 6-day observation period via ^{19}F MRI**.** Quantification from the composite images detected 78-94% of the initially injected NK cells across 6 days, with a significant decrease between days 3 to 6. Postmortem flow cytometry demonstrated retention of ^{19}F intracellularly within adoptively transferred NK cells with less than 1% of ^{19}F-containing cells identified as tumor-associated macrophages that presumably ingested nonviable NK cells. This work demonstrates that ^{19}F MRI offers a specific imaging platform to track and quantify murine NK cells within tumors noninvasively.

3.2 Introduction

Over the past two decades, cancer immunotherapies have demonstrated great success against a wide range of cancers.[98,99] However, tumors can evade the immune response by downregulating antigen presentation, reducing immunogenicity, and creating a tumor microenvironment that is exclusive of immune effector cells.[100] To overcome these barriers, strategies have focused on expanding and activating immune effector cells *in vivo* with biologic compounds such as monoclonal antibodies (mAbs), immune checkpoint blockades, and adoptive cell transfers (ACT) of lymphocytes to augment cytotoxic activity and tumor infiltration.[101]

One method of ACT involves using natural killer (NK) cells, members of the innate immune system that preferentially target virally infected and malignant cells without prior sensitization.[31] NK cells offer distinct advantages over T cell therapies as they do not require human leukocyte antigen matching and do not contribute to graft-versus-host-disease.[102] NK cells also have the ability to attack malignant cells via antibody-dependent cellular cytotoxicity (ADCC), produce cytokines like interferon-gamma (IFN-g) and tumor necrosis factor-alpha (TNF-a), and have the potential to be highly activated and expanded *ex vivo*.[32,103] In the last decade, the number of clinical trials using NK cells has increased, but other than a promising recent study showing high remission rates observed with CD19 chimeric antigen receptor (CAR) NK cells[104], most prior work has shown only modest results.[105–110] This may be partially due to the inability to track and quantify NK cells within tumors after infusion, which may improve the efficacy of treatment.[100,111] In this field of study, animal models have been critical to furthering the understanding of *in vivo* function and antitumor effects of NK cells.[112,113]

Currently, most immunotherapies lack biomarkers to predict the treatment response in patients.[36] A growing body of evidence suggests that the presence of NK cells in solid tumors is associated with more favorable clinical outcomes.[8,114] However, the behavior and persistence of these NK cells after injection are largely unknown although they may hold predictive information[3] and inform the timing of cellular infusions.[61] Molecular imaging platforms can provide an avenue to answer these important concerns.[35]

Magnetic resonance imaging (MRI)-based cell monitoring is free of ionizing radiation and capable of noninvasive, intratumoral imaging throughout the body.[84] Fluorine-19 MRI (^{19}F MRI) is a multinuclear quantitative imaging technique of fluorinated molecules, such as perfluorocarbons (PFC). Among the most commonly imaged PFCs are perfluoropolyether (PFPE) and perfluoro-15-crown-5-ether (PFCE), which can be emulsified to either directly label specific cell populations *ex vivo,* on indirectly label cells *in vivo*. When PFCs are introduced *in vivo* the PFC agent will enter the reticuloendothelial system where phagocytic cells like monocytes and macrophages will take up the agent.[115] PFPE, which is of particular interest to our work, is a linear PFC that has a relatively simple NMR spectra and contains >40 magnetically equivalent ^{19}F nuclei in its main resonance peak.[13] *Ex vivo* ^{19}F-labeling of cells enables subsequent detection *in vivo* by ^{19}F MRI after adoptive transfer.[12,77] Due to the low endogenous concentration of ^{19}F *in vivo*, an unambiguous positive signal is detected from the PFPE-labeled cell population without a confounding background signal. Quantification of cell numbers can then be approximated directly from the spin-density weighted ^{19}F MR images[63] assuming PFPE relaxation times are similar for *in vivo* conditions and regional flip angle variations are small. These assumptions are reasonable for our pre-clinical application in a homogenous tumor environment but may not hold for larger fields of view and heterogeneous local environments expected clinically. Thus, more rigorous development of a rapid workflow for B1-field, and T1, and T2 mapping will be important for clinical translation. Furthermore, conventional proton (^{1}H) MRI can be acquired in the same imaging session to visualize cell populations in the correct anatomical context. This form of hot-spot ^{19}F MRI is already in clinical testing in cancer patients with the labeling of dendritic cells[65]; however, ^{19}F MRI tracking of NK cells is still in preclinical development.[61,116]

Previously, we demonstrated the ability to label human NK cells and detect and quantify the cells longitudinally in 3 different xenograft mouse models[61]. However, one limitation of xenograft models is the usage of immunodeficient mice that do not inform the impact of the complete endogenous immune system on cell viability and trafficking. The goals of this study were to optimize the labeling for murine NK cells and validate cell-specific label retention *in vivo*, while longitudinally monitoring and quantifying the persistence of NK cells within a syngeneic, immunocompetent murine lymphoma model. ^{19}F MRI, while very specific, suffers from relatively low sensitivity compared to nuclear imaging methods[35], placing an emphasis on maximizing cellular uptake of the PFPE ^{19}F label while mitigating overt toxicity to the NK cells. The use of a ^{19}F MRI-optical dual probe, PFPE-Red, allows for validation of labeling both before infusion and postmortem via flow cytometry and confocal microscopy. A green fluorescent protein (GFP) reporter mouse can be used to specifically co-localize GFP^{+} NK cells in conjunction with the PFPE-red label.

In this study, we performed *in vitro* experiments to verify PFPE-Red labeling of murine NK cells, monitored NK cells longitudinally with ^{19}F MRI *in vivo* in a murine lymphoma model, and verified cell viability 0, 3, and 6 days after injection via flow cytometry, and imaging flow cytometry (ImageStream). Injection of PFPE-labeled GFP+ murine NK cells into a syngeneic lymphoma tumor model indicated that NK cells can be successfully detected and quantified with NK cell-specific ^{19}F signal persistence up to 6 days post-injection.

3.3 Methods and Materials

3.3.1 *Study Design*

In vitro studies were performed to establish cell viability, labeling efficiency and effects on cytotoxicity after incubation with PFPE. A total of 5 replicates of *in vitro* cell cultures were incubated with 2,4, and 8 mg/ml of PFPE to find the optimal loading of PFPE per cell while maintaining cell viability. Viability was assessed in duplicate at PFPE-incubation times of 4 and

24 hours at 1, 2, 4, and 8 mg/mL. NK cell cytotoxicity was also evaluated using 6 replicates at 2, 4, and 8 mg/mL to compare to previous work in human NK cells.[61]

All protocols were approved by the Institutional Animal Care and Use Committee (IACUC) at the University of Wisconsin-Madison. *In vivo* studies included a total of 6 male C57BL/6NCr mice studied longitudinally at day 0, 3, and 6 post-injection of PFPE-red labeled murine GFP positive (GFP+) NK cells derived from male C57BL/6-Tg(UBC-GFP)30Scha/J mice with the goal of detecting exogenous NK cells using the PFPE-red label. Cell viability was then verified with the co-incidence of the PFPE-red fluorescence label with the GFP label on flow cytometry after sacrifice. Four animals completed all time points and were sacrificed on day 6 to harvest the tumors. Two additional animals were sacrificed 2 hours after injection and on day 3 to assess cell viability and label specificity at the intermediate imaging time points. Tumors were harvested on day 6 to stay within protocol limits for allowed tumor size. The overall study design has been summarized, graphically, in Figure 3.1.

3.3.2 *Purification, expansion, and labeling of NK cells*

Male C57BL/6NCr mice were purchased from the National Cancer Institute (NCI) Animal Production Program and Charles River Laboratories International (Frederick, MD) and used between 24-25 weeks of age. Male C57BL/6-Tg(UBC-GFP)30Scha/J mice were purchased from The Jackson Laboratory (Bar Harbor, ME) and used between the 6-12 weeks of age. Mice were stored in a pathogen-free facility throughout the entirety of the study.

NK cells were isolated by harvesting the spleen and bone marrow and processing them into single-cell suspensions. Erythrocytes were depleted using ACK lysing solution (Lonza, Walkersville, MD). NK cells were isolated by negative selection using magnetic cell separation beads (Miltenyi Biotec, cat#: 130-115-818), sorted using AutoMACS® Separator (Miltenyi Biotec, San Diego, CA), and cultured at 37°C in 5% CO_2 in complete mouse media[117] (CMM) supplemented with 100 IU/mL recombinant human IL-2 (NCI Biological Resources Branch, Frederick, MD).

3.3.3 *Quantification of PFPE-label uptake via ^{19}F-NMR*

To determine ^{19}F uptake, NK cells were labeled (n=5 replicates) with PFPE (Celsense, Pittsburgh, PA) added directly into the cell culture medium (1 x10^6 cells/mL) at 2, 4, or 8 mg/mL. After a 24-hour incubation at 37°C with 5% CO_2, cells were harvested and washed 3 times with 1x PBS (Fisher Scientific, Pittsburgh, PA). Cells were counted using a Coulter Counter (Beckman Coulter, Indianapolis, IN) and aliquoted into microcentrifuge tubes for lysis. Cells were centrifuged at 1200 RPM for 6 minutes. Dry cell pellets were lysed using a lysis buffer containing deuterium oxide (D_2O), 1% Triton X-100 (Sigma Aldrich, St. Louis, MO), and 0.1% trifluoroacetic acid (TFA, Sigma Aldrich). TFA served as a ^{19}F NMR chemical shift reference and fluorine quantification reference to determine the uptake of the PFPE cellular label. Samples were transferred into NMR tubes (Wilmad Lab Glass, Vineland, NJ) and further diluted with D_2O such that the cell lysate solution fit the entire detection region of the NMR coil.

NMR spectroscopy was performed on a Varian Unity-Inova 500 MHz NMR spectrometer (Agilent Technologies, Santa Clara, CA). A 1D FID was acquired with a TR = 9 s, θ = 90°, 14.075 kHz spectral range, and NEX = 64. TFA and PFPE resonant peaks were integrated at -76 ppm and -91 ppm, respectively. The spectral areas from the cells (I_C) and reference (I_R) peaks, moles of reference (M_R), and the number of NK cells (N_C) along with Avogadro's number (N_A), were used to determine the cellular loading density, or the number of ^{19}F nuclei per cell (F_C), according to Equation 3.1 below.

$$F_C = \frac{3 \cdot I_C \cdot M_R \cdot N_A}{I_R \cdot N_C} \tag{3.1}$$

The mean F_C was taken as the average of each sample (N = 5) and the uncertainty was estimated as the standard deviation of F_C. NMR peak integration was performed in VNMR 6.1C (Agilent, CA, USA) with plotting performed in Matlab (MathWorks, Natick, MA).

To confirm intracellular PFPE uptake, NK cells isolated from GFP+ mice were incubated with 4 mg/mL of a dual MRI-optical PFPE-red cellular label (Celsense, Pittsburgh, PA) for 24 hours. PFPE-Red contains the linear PFPE polymer covalently conjugated to the red fluorescent dye BODIPy-TR with 588/616 nm excitation/emission. PFPE-red labeled NK cells were stained for 5 minutes with 2mL of a 300 μM solution of DAPI (ThermoFisher, cat#: D1306) in 1x Dulbecco's PBS (DPBS), washed with 1x PBS, and plated on a collagen-coated 35 mm glass-bottom dish (MatTex Corp., Ashland, MA). Live-cell fluorescence microscopy was performed on a Nikon A1RS 4-channel inverted point scanning confocal microscope system (Nikon Inc., Japan) with a 60x objective lens. This system can utilize 4 lasers to simultaneously excite blue (408 nm), green (488 nm), red (561 nm), and far-red fluorophores (638 nm). Image processing was performed in ImageJ (v1.6.0, NIH, USA).

3.3.4 *NK cell viability and cytotoxicity post-labeling*

NK cell viability was tested by trypan blue (Thermo Scientific, cat#: SV300084.01) exclusion assay using a hemocytometer. Samples of NK cells were incubated at concentrations of 1, 2, 4, and 8 mg/mL PFPE-red, in duplicate, for a total of 4 and 24 hours with control groups that had no PFPE label added.

NK cell cytotoxicity was determined by a 4 hour [^{51}Cr]-release assay against the NK cell–sensitive lymphoma cell line Yac-1 (Sigma-Aldrich, cat#86022801) using either ^{19}F-labeled or unlabeled NK cells (effector). Yac-1 (target) cells were labeled with 50 μCi of ^{51}Cr (NEZ030S; Perkin Elmer, Hopkinton, MA) per 10^6 cells and incubated for 90 minutes at 37°C. Cells were then washed to remove extra ^{51}Cr and target cells were resuspended in media. Yac-1 targets (5×10^3) were added at different effector to target ratios in a 96-well plate and incubated at 37°C for 4 hours.

Each group was measured using 6 replicates (n=6). The γ-scintillation of supernatant was measured by a γ-counter (PerkinElmer). Maximum release was determined by adding 100μL of 1X-Triton X-100 detergent (Sigma-Aldrich, cat#: 9002-93-1) to target cells. Spontaneous release was determined by adding 100μL of media to 100μL of target cells. The percent lysis was determined by ^{51}Cr release calculated according to Equation 3.2.

$$\%\ \text{Lysis} = 100\% \times \frac{(\text{Experimental} - \text{Spontaneous})}{(\text{Maximum} - \text{Spontaneous})} \tag{3.2}$$

3.3.5 *Murine syngeneic tumor model*

EL4 lymphoma cells (ATCC® TIB-39, Manassas, VA) were grown in CMM at 37°C in 5% CO_2 and used after 3-5 passages in culture after thawing. Cell authentication was performed using short tandem repeat analysis (Idexx BioAnalytics, Westbrook, ME) and per ATCC® guidelines using morphology, growth curves, and *Mycoplasma* testing within 6 months of use using the e-Myco mycoplasma PCR detection kit (iNtRON Biotechnology Inc, Boca Raton, FL). To establish a syngeneic lymphoma model, EL4 cells were injected subcutaneously at 10 x10^6 cells in 0.1mL into the flank of (n=6) C57BL/6 male mice. Once tumors reached 5mm in diameter, GFP+ NK cells were injected intratumorally as described below.

3.3.6 *In vivo ^{1}H/^{19}F MRI*

GFP+ NK cells were labeled with PFPE-Texas Red (Celsense) at 4 mg/mL for approximately 24 hours. A total of n=6 EL4 T cell lymphoma-bearing mice were injected with 5.3x10^5 (n=3) and 1.0x10^6 (n=3) viable labeled NK cells in 50 μL. Injected mice were imaged directly after injection (day 0), day 3, and day 6. Mice were induced with 3% isoflurane (Abbott Laboratories, Abbott, IL), monitored with a respiration pad, and maintained at 37°C using a warm-air blower. Mice were placed prone into a home-built ^{1}H/^{19}F quadrature volumetric RF coil. An external PFPE phantom with known ^{19}F spin density (ρ_R) was placed within the imaging volume and used as a ^{19}F signal reference during image acquisition. MRI was performed using a horizontal bore 4.7T small animal

MRI (Agilent Technologies, Santa Clara, CA). Anatomic T_1-weighted images were acquired with a spoiled gradient-echo with a flip angle (FA) of 20°, 132.6/4.2 ms TR/TE, a field of view (FOV) of 72x36 mm^2 with 2 mm slice thickness, acquisition matrix of 256x128, 50 kHz receiver bandwidth (RBW), NEX = 3, and a scan time of 50 seconds. T_2-weighted images were acquired with a fast spin-echo (FSE), 3000/20 ms TR/TE, 16 echo train length (ETL), matching FOV and resolution, and a scan time of 1 minute 12 seconds. The coil was then tuned to match the resonant frequency of ^{19}F (188 MHz). ^{19}F images were acquired using an FSE with a 1250/20 ms TR/TE, ETL of 8, matching FOV and slice thickness, acquisition matrix of 64x32, in-plane resolution of 1.1x1.1 mm^2, 16 kHz RBW, 400 NEX, and an added chemical saturation pulse at +2150 Hz to mitigate any ^{19}F signal contamination from isoflurane, for a total scan time of 25 minutes.

3.3.7 ***^{19}F MRI Postprocessing and Cell Quantification***

Image postprocessing and cell quantification were performed using FIJI ImageJ (National Institutes of Health, USA, http://imagej. nih.gov/ij) and MATLAB 2018B. The first postprocessing step was to scale the images against their noise, on a per slice basis. Given that the magnitude operation is nonlinear, the noise will follow a Rician distribution instead of a Gaussian distribution; therefore, magnitude images were first corrected to their expected Gaussian value. Using MATLAB, regions of interest (ROIs) were placed in areas devoid of signal in each slice of the magnitude images, where the mean value was corrected to give the standard deviation of the expected Gaussian distribution (s_N). Voxel values were then corrected using the scheme outlined in Gudbjartsson and Patz 1995:[118]

$$\tilde{A} = \sqrt{|I^2 - 2\sigma_N^2|} \tag{3.3}$$

where I is the measured signal intensity and $\tilde{A}$ is the expected value. To limit noise propagation, images were thresholded at $4s_N$ to ensure an adequate signal-to-noise ratio (SNR). After correcting and scaling the images against their own noise, the quantification process can now take place using

ImageJ. For each slice, pixels within the manually segmented tumor were summed to represent the total ^{19}F signal within the volume (S_V). An ROI was then placed within the boundaries of the ^{19}F reference vial where the mean value ($\bar{S}_R$) was recorded along with its standard deviation. The known spin density of reference vials (^{19}F atoms/mL) was normalized against the voxel volume to give ^{19}F atoms/voxel. Using the mean loading density, F_C, (^{19}F atoms/cell) the apparent number of cells in the MR images was calculated as seen in Equation 3.4.

$$N_C = S_V \cdot \frac{\rho_R}{F_C \cdot \bar{S}_R} \tag{3.4}$$

The associated uncertainty in the apparent number of cells (s_{N_c}) was calculated according to Equation 3.5:

$$\sigma_{N_C} = N_C \cdot \sqrt{\left(\frac{\sigma_{S_V}}{S_V}\right)^2 + \left(\frac{\sigma_{F_C}}{F_C}\right)^2 + \left(\frac{\sigma_{\bar{S}_R}}{\bar{S}_R}\right)^2} \tag{3.5}$$

Where $\sigma_{S_V} = \sigma_N \cdot \sqrt{2 \cdot N}$ and N is the number of nonzero pixels in the tumor region. For display purposes, ^{19}F images were resampled (bicubic interpolation) via MATLAB to match the image size of the ^{1}H images and composite images were created for anatomic reference.

3.3.8 ***Postmortem Flow Cytometry***

Immediately after imaging on day 6, mice were euthanized, and their tumors were excised for either postmortem flow cytometry (n=3) or image flow cytometry (n=1) analysis. Tumors were cut into 2-3mm pieces and digested with 2 ml of 2 mg/ml collagenase D (Worthington Biochemical, Cat#: LS004188) for 10 minutes at 37^{o} C. 10 ml of 1x PBS was added to quench the collagenase D reaction, at which point the tumors were mechanically dissociated and passed through a 70µm cell strainer (Corning®, New York, New York). Tumor cell suspensions were then spun down in a centrifuge at 1200 RPM for 10 minutes. The cell suspensions were then digested with ACK lysing buffer. Cell suspensions were then washed and spun down again at 1200 RPM, and then resuspended in 10ml 1x PBS, 10µL of which was added to 10mL of Isoton® diluent and counted on a Coulter Counter® Z1 Series Particle Counter (Beckman Coulter, Brea, CA). From this count, 10^6 cells were added to flow cytometry tubes in staining buffer (PBS with 2% FBS, 0.05% sodium azide, and 0.05% EDTA) and stained with 5µL of Alexa Fluor 647 anti-mouse F4/80 antibody (Biolegend® catalog #) for 30 minutes at 4° C. The cells were then washed with 1x PBS, spun down, and 0.5µL of Ghost Dye™ Red 780 viability dye (Tonbo Biosciences) was added for 20 minutes at room temperature. Cells were then washed with staining buffer, spun down, and resuspended in 400µL of staining buffer. The cells were then run on either the Attune™ NxT Flow Cytometer (Thermo Fisher Scientific) or the Amnis™ ImageStream MKII (Luminex Corp, Madison, WI), with subsequent analysis being performed with FlowJo™ software (BD, Ashland, OR). The addition of the viability and antibody dyes to the 3 resected tumors, allow us to first isolate the viable from non-viable cells, then further classify the cells as either adoptively transferred (GFP+) or endogenous (GFP-), labeled (PFPE-red+) or unlabeled (PFPE-red-), and endogenous macrophage (GFP-, F4-80+) or not.

3.3.9 ***Statistics***

Statistics were performed using GraphPad Prism version 9.0 (GraphPad Software, San Diego, CA). MRI-based cellular quantification data were expressed as mean ± SD, whereas all other data were expressed as mean ± SEM. For analysis of the three cell quantification groups, a mixed-effects model was implemented. For significant results, a post hoc Tukey's multiple comparison test was performed. A P-value (p) less than 0.05 was considered statistically significant.

3.4 Results

3.4.1 ***PFPE labeling optimization of NK cells***

PFPE labeled NK cells showed similar viability to that of the unlabeled controls at both 4- and 24-hours using concentrations of 1, 2, 4, and 8 mg/mL PFPE (Figure 3.2A). A reduced NK-mediated cytotoxicity was detectable at high effector: target ratios in the presence of 2, 4, and 8 mg/mL of PFPE compared to unlabeled control at 24-hours post-labeling (Figure 3.2B). NMR results (Figure 3.2C) indicated a mean PFPE labeling on the order of 10^{12} ^{19}F atoms/cell for all three labeling concentrations. Thus, while the ^{19}F-PFPE label did not impact the viability of murine NK cells and led to a high number of ^{19}F atoms on a per cell basis, there was a measurable reduction of cytotoxic potential across the labeled groups compared to control. For this reason, 4 mg/mL PFPE-Red was chosen as our labeling concentration for *in vivo* experiments, which achieved an average PFPE-red loading of $2.0\pm0.5 \times 10^{12}$ ^{19}F atoms/cell.

3.4.2 *Live-cell confocal microscopy validation of cellular labeling*

Live-cell confocal microscope images of DAPI-stained, PFPE-red labeled GFP$^+$ NK cells demonstrated intracellular labeling could be detected in the presence of an endogenous fluorescent transgene (Figure 3.3). This data indicated that ^{19}F is taken up by murine NK cells, can be detected intracellularly, and can be detected simultaneously in the presence of another fluorescent marker.

3.4.3 *In vivo ^{1}H/^{19}F MRI and cellular quantification*

To assess the detectability of PFPE-labeled GFP$^+$ murine NK cells in a syngeneic tumor model, EL4 lymphoma cells were injected into the flank and allowed to establish solid tumors with a minimum size of 5x5 mm^2. Then intratumoral injections of ^{19}F labeled GFP$^+$ NK cells were performed and ^{1}H/^{19}F MRI was acquired at 0, 3, and 6 days post NK cell transfer. As seen in a representative mouse (Figure 3.4), labeled NK cells were successfully detectable in all mice at each imaging time point. To assess the remaining NK cells in the tumor at each time point, quantification was performed from the composite images, indicating an average of 91% of the initially injected cells were detected on day 0 (1-2 hours post-intratumoral injection), 94% on day 3, and 78% were detected at day 6 (Figure 3.5), where a statistically significant decrease was detected in NK cell number from days 1 to 6 and days 3 to 6 ($p < 0.05$).

3.4.4 *Postmortem flow cytometry*

At days 0, 3, and 6 imaging time points, 1 mouse was euthanized, and its tumor resected for analysis by image flow cytometry. As depicted in Figure 3.6A, cross-sectional images for brightfield, green, red, and green-red composite channels of a GFP+ PFPE-red+ cell show internalization of the imaging agent at each timepoint. ImageStream also demonstrated (Figure 3.6B-C) that greater than 60% of the GFP+ NK cells and less than 7% of the endogenous cells (GFP-) contained PFPE-red label at all imaging time points. However, between days 3 and 6, we see a rapid decline in the percentage GFP-, PFPE-red+ and an increase in the percentage of labeled GFP+, PFPE-red+ present within the tumor, suggesting clearance of non-viable cells and free imaging agent between these time points.

In addition to the imaging flow cytometry, on Day 6, the remaining 3 tumors were resected and analyzed by conventional flow cytometry, which demonstrated a mean of 52±8% of the remaining adoptively transferred GFP$^+$ NK cells contained ^{19}F PFPE-red (Figure 3.7A). The mean GFP+ viability for these tumors was approximately 39.7±17%. In contrast, less than 0.3±0.1% of the endogenous tumor GFP$^-$ cells contained ^{19}F PFPE-red. Within the 3 tumors analyzed a mean of 29±3% of the endogenous ^{19}F PFPE-red$^+$ cells were F4/80$^+$ tumor-associated macrophages (Figure 3.7B). The median fluorescent intensity (MFI) of the ^{19}F PFPE-Red was decreased ($p < 0.01$) in endogenous cells within the tumor by a factor of 2.3 compared to the adoptively transferred NK cells (Figure 3.7C) indicating the primary cell population that is detected and quantified by ^{19}F-MRI are viable, adoptively transferred NK cells.

3.5 Discussion

NK cells continue to be an emerging cell therapy for the treatment of relapsed and refractory cancers, including lymphoma.[104] Developing cellular imaging methods to monitor and assess NK cells *in vivo* will address one of the challenges associated with the translation of immunotherapies from preclinical animal models to humans. Without quantitative image guidance, the clinician is blinded as to where the effector cells migrate to, how long they persist, and if they reach the target tissue[3], which can make treatment timing and assessment challenging.[32,119] The field also does not know what minimum threshold of NK cells is needed to reside in a tumor to elicit a clinical response. Thus, pre-clinical development of a platform incorporating ^{19}F-MRI with murine NK cells can leverage immunocompetent tumor models to test the feasibility for *in vivo* cell detection, the persistence of ^{19}F-label, and quantification using MRI to further develop this technique for future clinical trials.

Cell tracking with ^{19}F MRI, in general, will benefit from data acquisition strategies that improve the detection sensitivity to monitor cell behavior *in vivo*. Here, we focused on improving the quantification and labeling strategy. The signal strength is determined in part by the number of ^{19}F nuclei infused into the cells during incubation with ^{19}F-PFPE. We found a balance between ^{19}F-PFPE concentration and labeling efficiency in terms of cell viability and killing effectiveness, which allowed for a greater average signal per cell and thus, a more MRI-sensitive acquisition while maintaining the cell-killing capacity. Previous work by us[61] and others[116] have shown PFPE labeling of human NK cells is feasible, non-toxic, and does not appear to affect viability, cytotoxicity, or cytokine secretion by NK cells. Here we show that the cellular uptake or labeling efficiency can then be quantified by ^{19}F NMR, where the mean PFPE uptake showed a linear increase in loading (^{19}F nuclei/cell) with increasing PFPE labeling concentration. Moreover, the observed cellular labeling efficiency (^{19}F nuclei/NK cell) for murine NK cells in this study by NMR is nearly 10-fold greater than those reported previously by our group using human NK cells[61] which is advantageous for detection by MRI. However, ^{19}F-PFPE labeling of murine NK cells showed a modest but statistically significant impact on the cytotoxic function of the labeled NK cells, unlike our previous analysis of human NK cells[61], suggesting a species-specific, cell subset sensitivity to ^{19}F as no impact on cytotoxicity has been observed with murine[64] or human[10] T cells.

Our study demonstrates viable NK cell detection delivered via intratumoral injection *in vivo* over 6 days, where a significant decrease in labeled NK cells was detected after the day 3 imaging timepoint. The use of the ^{19}F-PFPE-red and the secondary GFP label confirmed cellular uptake before infusion via confocal microscopy and assessment of label retention and cellular viability via postmortem flow cytometry. The postmortem analysis indicated that an overwhelming majority of the ^{19}F MRI signal was specific to viable adoptively transferred ^{19}F-labeled NK cells retained in the tumor after 6 days. The results from the imaging flow cytometry indicate that at days 0 and 3, the majority of GFP+ cells within the tumor still contained their label and provides visual confirmation that the PFPE-red agent is contained within the cell membrane. Furthermore, the reduction in the percentage of endogenously labeled cells and increase in the percentage of labeled adoptively transferred cells from days 3 to 6 suggest clearance of endogenously labeled cells from the tumor. Less than 0.5% of the endogenous cells within the tumor presented with the ^{19}F label, supporting the conclusion that the signal detected by ^{19}F-MRI remains specific to the adoptively transferred NK cells. Overall, GFP+ NK cell viability at Day 6 was widely variable, with an average of 39.7±17%. While the source of this large range is unknown, we suspect it could be related to inherent biological variability and/or differences in tumor processing time after collagenase digestion for the respective tumors. This result may warrant further research. The presence of ^{19}F^{+} tumor-associated macrophages is consistent with the expected makeup of the tumor microenvironment in that any nonviable ^{19}F^{+} NK cells would be likely phagocytosed by tumor-associated macrophages but given the relatively small amount detected and their lower mean fluorescent intensity, the presence of phagocytic cells within the tumor had minimal effect on the appearance of ^{19}F images and their quantification.

Several imaging modalities with higher cell detection sensitivity than ^{19}F MRI have previously utilized in pre-clinical settings to monitor NK cell infusions, including positron emission tomography (PET), single-photon emission computed tomography (SPECT), optical imaging (OI) (bioluminescence and fluorescence imaging) and MRI.[35,120] While superparamagnetic iron oxide nanoparticle (SPIO) based MRI methods provide greater sensitivity, they rely on indirect detection of the cells by measuring negative contrast.[121,122] These methods are therefore less specific and due to the non-linear relationship between iron concentration and signal loss, quantification is much more complicated.[123] PET/SPECT isotopes such as Fluorine-18 (^{18}F), Carbon-11 (^{11}C), and Indium-111 (^{111}In) offer high detection sensitivity to allow detection of smaller cell populations labeled with receptor-targeted radioactive isotopes; however, labeling NK cells with long half-life radioactive isotopes exposes patients to ionizing radiation, and could have toxic effects on NK cell viability. Additionally, PET and SPECT lack the high resolution of anatomical structures and only offer a limited imaging window due to radioactive decay of the isotope, preventing detection of long-term NK cell persistence.[40,111] Furthermore, detachment of the cell-bound radioisotope from the cell may give false positives for the true location of NK cells.[124] Optical imaging using fluorescent and bioluminescent techniques has previously provided insight into NK cell trafficking patterns in preclinical models[125,126], but optical methods have limited light penetration, severely impeding the clinical applicability of these techniques.[35,38]

However, there are three important limitations in the work presented here. The first limitation is the small sample size, although each animal serves as its own control increasing the statistical power and the in-depth study to evaluate NK cell viability using flow cytometry is unprecedented. Second, we have not optimized the pulse sequence used suggesting further improvement in sensitivity is possible. Specifically, balanced steady-state free precession (bSSFP) and ultra-short echo time (UTE) have been explored for PFC-based ^{19}F MRI to increase sensitivity.[127,128] With PFPE relaxation times at 4.7 T, Faber and Schmid deduced that a bSSFP approach would produce the optimal sensitivity or SNR-efficiency.[96] However, in this study we chose to use a 2D FSE to reduce potential artifact presence. Other methods using T_1-shortening agents like gadolinium-based contrast agents or superparamagnetic iron oxide (SPIO) nanoparticles to boost SNR-efficiency have also been studied.[121,129,130] While these improvements to the ^{19}F contrast agents are promising, cellular toxicity and corresponding safety profiles have yet to be fully explored. The work presented here, and ^{19}F MRI in general, could also benefit from acceleration techniques like parallel imaging[131] or compressed sensing (CS) approaches.[132,133] CS techniques, which undersample k-space to reduce the amount of data required, have achieved acceleration factors of up to 8 without loss in SNR in ^{19}F MRI applications.[134,135] These acceleration techniques can be used to decrease scan times for translational applications or allow for high signal averaging to increase maximum achievable SNR. The third limitation is that most clinical trials using adoptively transferred cells are administered intravenously. However, clinical trials testing intratumoral injection of immune cells like dendritic cells or CAR T cells have emerged in the last decade.[136–142] In the majority of cases, lymphomas occur in deep lymph nodes within the patient, where intratumoral injection is not feasible. For clinical translation, intratumoral injection of NK cells needs to be applied on large, superficial lymph nodes (e.g. cervical or supraclavicular) or advance to intravenous injection of NK cells with homing of ^{19}F-labeled NK cells to deep regions of lymphomatous involvement. Nonetheless, the presented work establishes a timeline for adoptively transferred NK cell viability within the tumor microenvironment of an immunocompetent mouse, and thus is a first step to quantifying longitudinal cell-specific labeling *in vivo* for future IV injection experiments.

In this study, we optimized cellular labeling and quantification of murine NK cells with ^{19}F *in vitro* and unambiguously detected and quantified ^{19}F-labeled NK cells within an established syngeneic lymphoma tumor *in vivo* longitudinally across 6 days. Furthermore, we validated ^{19}F label persistence and viability within adoptively transferred murine NK cells and found minimal potential false-positive readings from endogenous phagocytic cells within the tumor over the same time period. This work demonstrates the feasibility of tracking murine NK cells as a therapeutic adoptive cell therapy for cancer and will inform preclinical models of cancer immunotherapy.

3.6 Acknowledgements

This work was supported by grants from a National Cancer Institute/National Institutes of Health (NCI/NIH) R01 CA215461 (L.M.L, S.B.F., and C.M.C.), National Heart, Lung, and Blood Institute/NIH (NHLBI/NIH) T32 HL07899 (K.L.W.), NIH TR000429 (K.D.L.), Hyundai Hope on Wheels, American Cancer Society Research Scholar grant RSG-18-104-01-LIB (S.B.F. and C.M.C.), St. Baldrick's – Stand up to Cancer Pediatric Dream Team Translational Research Grant SU2C-AACR-DT-27-17 and the MACC Fund (C.M.C). We would like to thank the UWCCC Experimental Animal Pathology and Flow Cytometry core facilities, which are supported in part through NCI/NIH P30 CA014520. The St. Baldrick's Foundation collaborates with Stand Up to Cancer. Stand Up to Cancer is a division of the Entertainment Industry Foundation. Research Grants are administered by the American Association for Cancer Research, the Scientific Partner of SU2C. The contents of this article do not necessarily reflect the views or policies of the Department of Health and Human Services, nor does mention of trade names, commercial products, or organizations imply endorsement by the US Government.

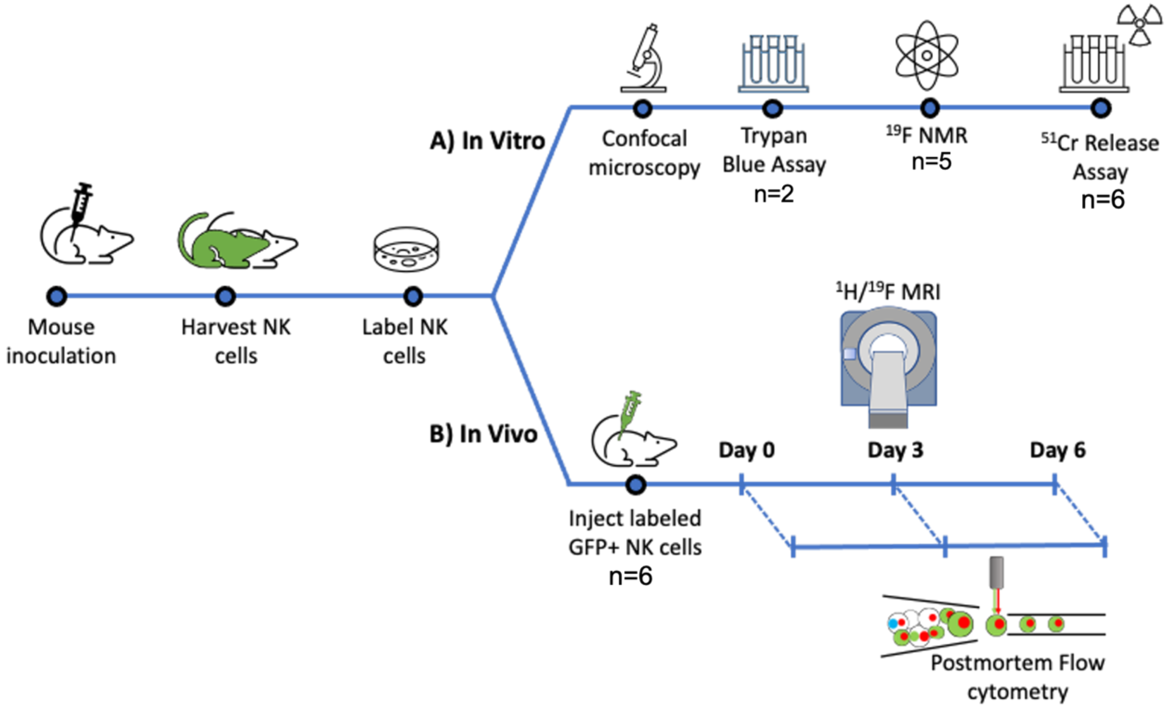

Figure 3.1: Graphical summary of the experimental design. *A graphical overview of the experimental design that starts with the establishment of the syngeneic tumor, purification of NK cells, and subsequent labeling with PFPE-red agent. (**A**) The in vitro arm of the experiment was used to characterize the cytotoxic effects of the labeling procedure (n=6), characterize the viability (n=2) and label uptake (n=5), and confirm labeling with optical imaging methods. (**B**) The in vivo arm of the experiment carried out with (n=6) intratumoral injections of either 1.0x10^{6} or 5.3x10^{5} PFPE-red labeled GFP+ NK cells into tumor-bearing mice that were imaged at days 0, 3, and 6 post injection. One mouse was euthanized at the baseline and day 3 timepoint, followed by 4 mice at the conclusion of day 6 of imaging. The tumors (n=6) were excised and analyzed via flow or imaging flow cytometry to assess label retention and cell viability.*

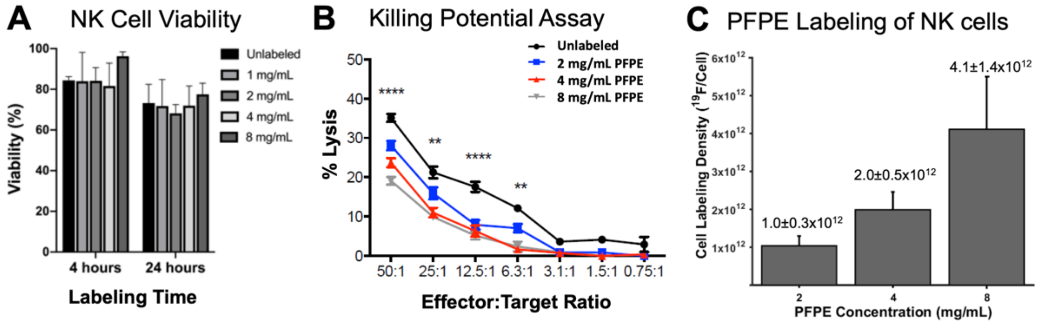

Figure 3.2: Viability, cytotoxic potential, and PFPE loading of murine NK cells after labeling. *(**A**) Trypan blue exclusion assay results of mouse-derived NK cellular viability post-labeling with 4 different concentrations of PFPE compared to control, in duplicate (n=2). All bars were normalized to a viability measurement at 0 hours for all groups. (**B**) A [^{51}Cr] release assay for NK (effector) cell cytotoxic function against a NK cell sensitive tumor cell line, Yac-1, is shown after incubation with different concentrations of PFPE label. Each group was performed with six replicates (n=6). (**C**) NK cell labeling density in terms of ^{19}F atoms per cell (F_c) as measured by ^{19}F NMR from five replicates (n=5). Statistical difference indicators: * = p<0.05, ** = p<0.01, *** = p<0.001, **** = p<0.0001.*

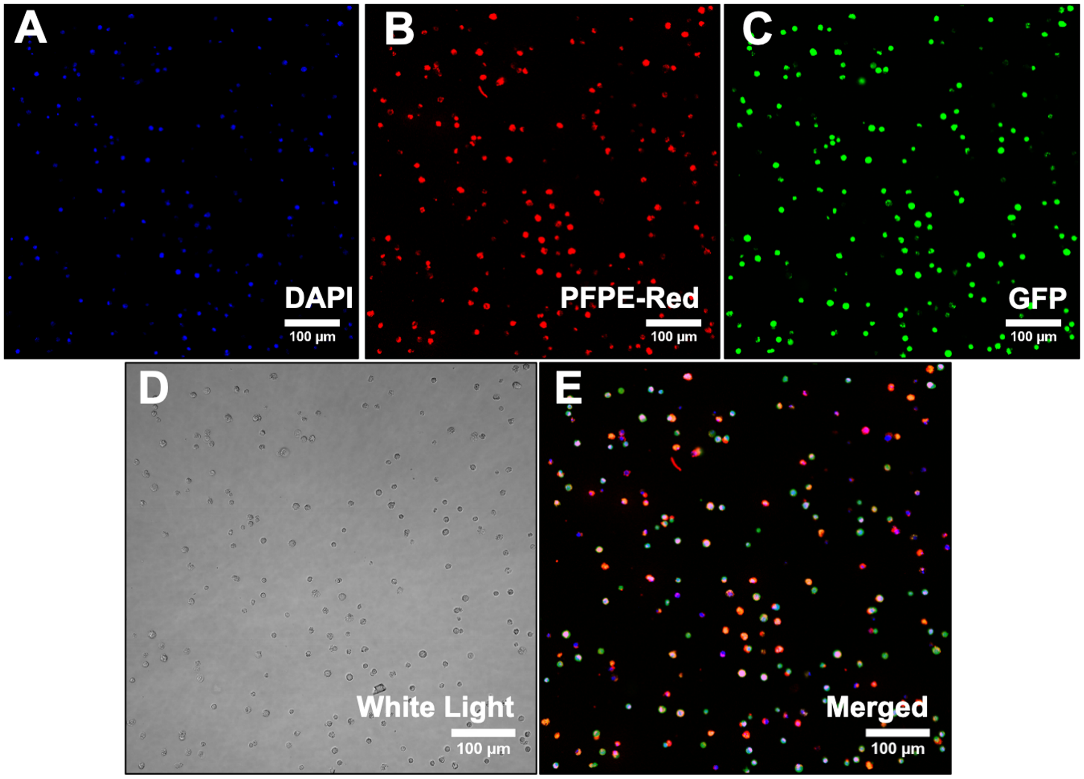

Figure 3.3: Live cell fluorescence microscopy images shows NK cell labeling. *Live cell fluorescence microscopy images of PFPE-Red labeled GFP+ NK cells, showing the fluorescent signal from* ***(A)*** *DAPI staining,* ***(B)*** *PFPE-Red,* ***(C)*** *GFP, and* ***(D)*** *white light individually, where* ***(E)*** *the merged image shows colocalization of the various labels. A 100 µm scale bar is included.*

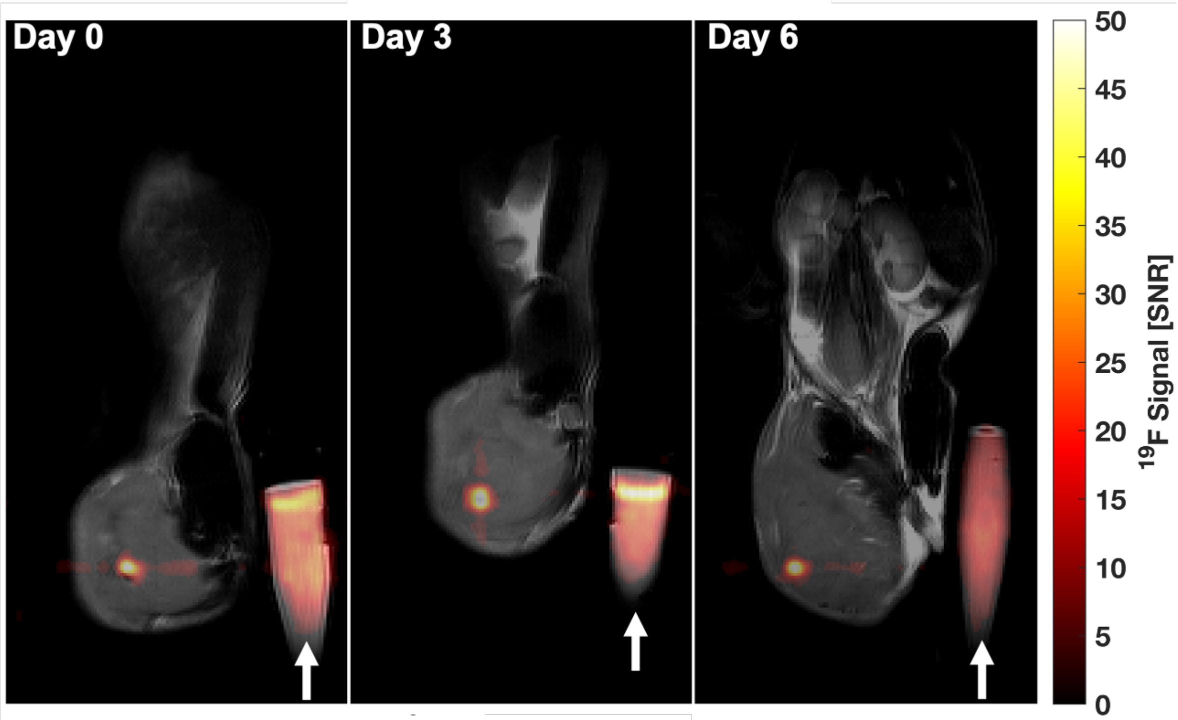

Figure 3.4: $^1H/^{19}F$ composite images showing signal across the 3 imaging timepoints. *Representative magnitude images across the 3 imaging time points. ^{19}F Images were scaled on a per slice basis against their own corrected noise. The ^{19}F signal ("hot metal" color and color bar) from the labeled cells is visible within the tumor in all three images with an average SNR within the tumor of 11±2, 14±3, and 13±4. White arrow indicates the reference vial of known ^{19}F spin density.*

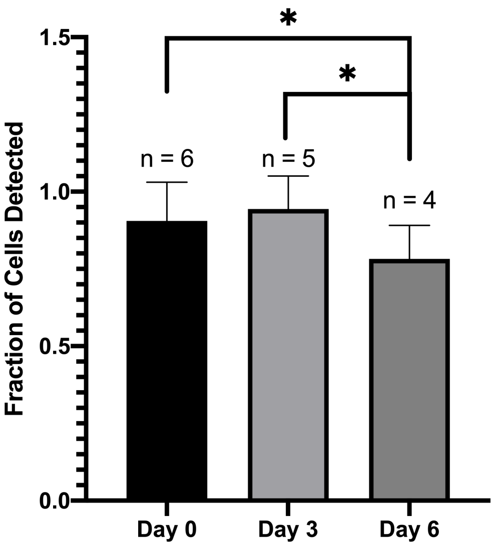

Figure 3.5: ^{19}F MRI murine NK cell quantification verifies NK cell persistence over 6 days. *In vivo MRI NK cell quantification results indicate the percentage of initially injected GFP+ NK cells within the boundaries of the mice tumors. The percentage of initially injected cells from days 0 to day 6 is shown where a significant decrease is detected from days 3 to 6 ($p<0.05$). Error bars are represented as the standard deviation of the NK cell quantification calculation.*

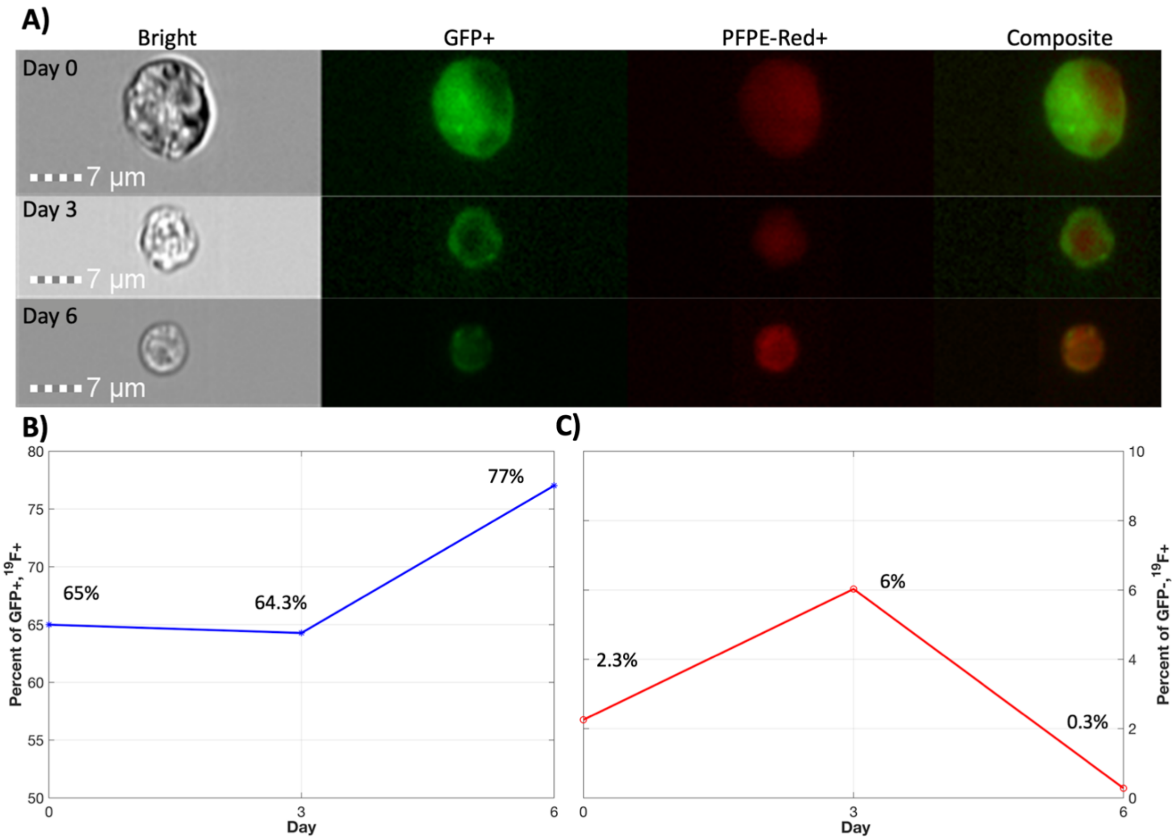

Figure 3.6: Postmortem ImageStream flow cytometry validation of cell label retention across 3 time points. (A) *ImageStream flow cytometry showing the brightfield, green, red, and composite channels for a representative GFP+ PFPE-red labeled murine NK cell that was detected in the resected tumors at days 0, 3, and 6 post injection, where each time point represents a tumor from a single mouse.* ***(B)*** *The resultant percentage of GFP+ that were* ^{19}*F+ (labeled adoptively transferred population) and* ***(C)*** *GFP- that were* ^{19}*F+ (endogenous labeled population) have been plotted in blue and red, respectively. A peak in non-specific labeling is seen at day 3, followed by both a sharp increase in percentage of labeled GFP NK cells and a decrease in percentage of endogenously labeled cells.*

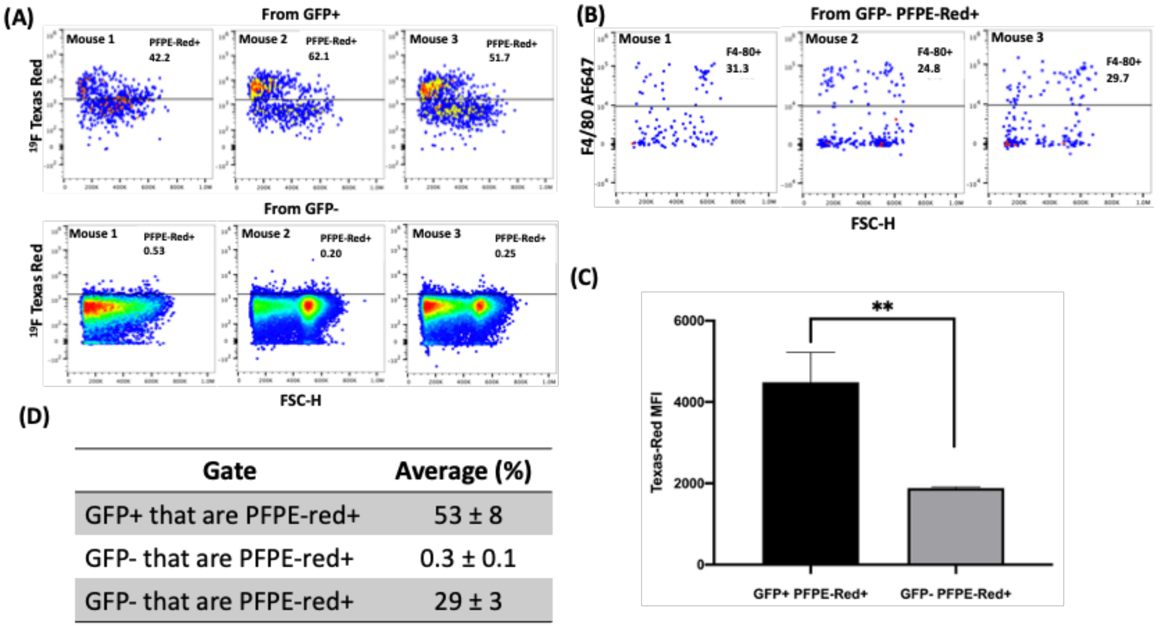

Gate	Average (%)
GFP+ that are PFPE-red+	53 ± 8
GFP- that are PFPE-red+	0.3 ± 0.1
GFP- that are PFPE-red+	29 ± 3

Figure 3.7: Postmortem flow cytometry indicates viable, PFPE-labeled NK cells at day 6 post-injection. *Flow cytometric analysis at day 6 post-intratumoral injection of NK cells from 3 excised murine syngeneic EL4 lymphoma tumors showing* ***(A)*** *the percentage of cells from GFP+ and GFP- that contain the PFPE-red label for each mouse,* ***(B)*** *the quantified MFI for GFP+ and GFP- PFPE-red containing cells, where the error bars represent the standard deviation in the measure,* ***(C)*** *the percentage of GFP- PFPE-red containing cells that are macrophages, and* ***(D)*** *a summary of the mean values found by flow cytometry across the tumors. The post-processing GFP+ viability was 64.7%, 29.0%, and 25.5% for mice 1, 2, and 3, respectively. Mean GFP+ viability was 39.7%. Note: ** = p-value < 0.01.*

Chapter 4 INVESTIGATION OF IN VIVO STABILITY AND PASSIVE TUMOR TARGETING OF A NOVEL ^{19}F CONTRAST AGENT

Additional Contributors: Alexa Heaton, PhD; Montira Tangsangasaksri, PhD; Sandro Mecozzi, PhD

Note: Portions of this work is currently being prepared for submission in ACS Biomaterials: Science and Engineering (Impact Factor: 4.79).

4.1 Abstract

Purpose: Fluorine-19 (^{19}F) MRI is an alternative method that can utilize certain stable and biologically compatible compounds known as perfluorocarbons (PFCs) as MRI contrast agents for cancer detection. These PFC agents are encapsulated in nanoemulsions (NE). The purpose of this work was to implement a novel nanoemulsion with improved PFCE loading and stability to test the ^{19}F MRI detection abilities in both a phantom and in vivo tumor model and to assess passive tumor targeting, likely via increased vascular permeability.

Methods: Tumor-bearing mice, injected with the NE (n = 5), were imaged with ^{1}H/^{19}F MRI at 5 time points over the course of 14 days and the PFCE NE signal in tumor and liver was quantified. The NE was intravenously administered via tail vein. To quantify passive targeting in the tumor, ROIs were drawn within the tumor and in the left lobe of the liver.

Results: *In vivo* ^{19}F-MRI provided information on NE biodistribution in all mice. At 6 hours post-injection, NE is seen primarily in the liver and spleen and a substantial amount in other organs. After day 0, accumulation at the tumor site is clearly visible, while at day 14, signal decreases uniformly in the tumor, liver, and spleen, suggesting clearance from the body.

Conclusions: *In vivo* images were acquired for 5 tumor-bearing mice across 14 days. All mice appeared to tolerate the large dose of PFCE NE, as no adverse effects were observed. This study demonstrates repeatable ^{19}F MRI of a novel NE that passively targeted the cancer tumor with improved stability and increased overall loading compared to typical NEs.

4.2 Introduction

Currently, there is a demand for improved techniques to diagnose and treat cancers. Various methods such as positron emission tomography (PET), computed tomography (CT), and MRI are utilized as diagnostic imaging tools to detect cancerous lesions. PET imaging offers a unique ability to both detect cancers and metastases at very high sensitivity and to probe functional information from the lesion. However, PET imaging offers fairly low resolution and relies upon injection of radiolabeled pharmaceuticals that delivers harmful ionizing radiation to the patients, limiting its ability to be utilized on a repeated, longitudinal basis. CT imaging is quick and provides excellent resolution, but suffers from lower soft tissue contrast and, like PET, delivers ionizing radiation to the subject. MRI techniques, on the other hand, do not rely on ionizing radiation and have excellent soft tissue contrast and resolution, which allows for visualization and biological quantification *in vivo*.

Conventionally, MRI generates signal by magnetizing the proton (^1H) nuclei (water or fat) in the subject by way of strong magnetic fields with subsequent RF excitation and signal readout. The time frames of magnetization signal decay and regrowth, or relaxation times, are leveraged in order to generate contrast between various types of soft tissue (i.e. fat/water, gray/white matter).[143] Paramagnetic contrast agents like Super Paramagnetic Iron Oxide (SPIO)[44], Gadolinium(III)[43], or Manganese(II)[144] chelates can also be utilized to further manipulate the relaxation times of the ^1H nuclei in their proximity. SPIO-based MRI creates strong fluctuations in the local magnetic field, which ultimately lead to a hypointense signal, or negative contrast, in regions of high SPIO concentration. Gadolinium (Gd) techniques create signal enhancement in regions of high Gd agent concentration through T_1 shortening. Gd or SPIO contrast enhanced anatomic images, while sensitive, are often difficult to interpret and can require pre- and post-contrast images to analyze tumor volumes.[145] Furthermore, there are concerns that certain Gd contrast agents can pose a safety risk to various patient populations. Those patients with impaired kidney function are at increased risk of developing nephrogenic systemic fibrosis (NSF) after delivery of the contrast agents.[146,147] Moreover, various studies have shown gadolinium-based contrast agent accumulation within the brain and kidneys.[148,149]

One emerging set of techniques to generate contrast include MRI of alternate nuclei, such as fluorine-19 (^{19}F) MRI, which is attractive for multiple reasons. Fluorine nuclei offer 100% natural abundance, 82% sensitivity compared to conventional ^{1}H MRI, and is found at negligible concentrations *in vivo*.[54] Thus, ^{19}F MRI provides a noninvasive and nonionizing imaging modality that provides positive contrast "hot spot" images that can be utilized for cancer imaging. The most common agents used in ^{19}F MRI are fluorinated compounds known as perfluorocarbons (PFCs). These fluorinated compounds have a carbon backbone and the resultant C-F bonds are extremely strong.[50] This chemical resilience makes PFC agents biologically inert in animals and humans, with no metabolism being observed *in vivo*.[51,52] PFCs are taken up into the reticuloendothelial system (RES), which is comprised of phagocytic cells like monocytes and macrophages, and are subsequently cleared by exhalation in the lungs.[96] One particular PFC of interest, perfluoro-15-crown-5-ether (PFCE), is a relatively small commercially available PFC that has 20 magnetically equivalent ^{19}F nuclei that results in a desirable, single resonance frequency.[150]

These PFC agents are very fluorophilic and are not miscible in water or hydrophobic substances; therefore, PFCs need to be emulsified for intravenous (IV) delivery.[54] In these nanoemulsions (NE), the PFC acts as that core and along with the emulsifier, typically phospholipids or poloxamers, they can be formed into a nanoemulsion (NE), using sonication, high-pressure homogenization, or microfluidization, with a typical target droplet size being 100-200 nm in diameter.[53,145] PFC nanoemulsions < 500 nm have been extensively studied for application in various biomedical applications, such as blood substitutes and ultrasound contrast agents.[51,52] As explained by Flögel and Ahrens 2017, these PFCs can accumulate at sites of inflammation through uptake into the reticuloendothelial system, but also through "passive targeting” as the PFCs leave the blood stream into the tissue through leaky endothelial barriers. Given their relative size, PFC extravasation through fenestrated endothelium in the liver sinusoid, spleen, and inflamed tissue or tumor can occur.[89,96,151] PFCs can transiently accumulate within tumors or inflamed tissue due to the increased blood flow and decreased drainage to the lymphatics.[96] This effect, known as enhanced permeability and retention (EPR), has been studied for use in cancer drug delivery and cancer imaging[152,153], and specifically using ^{19}F MRI to monitor PFC uptake into tumors.[154]

In this study, a novel, highly concentrated PFCE-loaded nanoemulsion, developed by our collaborators, was tested for its tolerance, detection, and passive tumor targeting in tumor-bearing mice. More specifically, mice we given IV injections of the novel PFCE agent, imaged over the course of 14 days via ^{1}H/^{19}F MRI, and analyzed for agent distribution in organs of interest.

4.3 Methods

4.3.1 *Study design and instrumentation*

In this study, shown graphically Figure 4.1, (n=5) six- to eight-week-old 4T1-Luc tumor-bearing BALB/c mice were given IV injections of the novel PFCE NE, described in previous work[155], and tracked across 5 separate time points out to 14 days, where the transient ^{19}F signal within organs of interest and tumor were assessed. All ^{1}H/^{19}F MRI was performed using a 4.7T horizontal bore small animal MRI (Agilent Technologies, Santa Clara, CA). All image post processing was performed via MATLAB 2015b (Mathworks, Natick, MA).

4.3.2 ***^{19}F MRI experiments***

4.3.2.1 Phantom imaging

^{1}H/^{19}F MRI were acquired using a home-built ^{1}H/^{19}F quadrature volume coil with a 1.5″ diameter and a 3″ length for detection. A custom-made phantom described previously[156], was loaded with 5 microcentrifuge tubes (1.1 mL) containing serially-diluted PFCE-NE of concentrations 1070, 770, 460, 150, and 0 mM (water). ^{1}H images of the phantoms were acquired using a multi-slice gradient echo pulse sequence with 0.19 × 0.19 × 2.0 mm^3 in-plane resolution, 48 × 48 FOV, TR/TE = 89.6/4.4 ms, 20° flip angle, NEX = 3, and 1 min 9 s imaging time. ^{19}F images were acquired, without disturbing the setup, using a multi-slice FSE with a 0.25 × 0.25 × 2.0 mm^3 in-plane resolution, 48 × 48 mm^2 FOV, 222.4 /20.0 ms TR/TE, echo train length (ETL) of 8 echoes, NEX=128, and 7 min 35s imaging time.

4.3.3 *In vivo imaging*

The *in vivo* mouse MRI experiments were performed using protocols approved by the University of Wisconsin Institutional Animal Care and Use Committees (IACUC), where six to eight-week-old female BALB/c mice were obtained from Harlan Laboratories (Envigo, Indianapolis, IN). Tumor-bearing mice (n=5) were given IV tail vein injections of the PFCE NE (35% v/v, 1.07 M PFCE, 200 μL) where ^1H (anatomic) and ^{19}F MRI was acquired one day prior to injection, then at 0.25, 1-, 4-, 7-, and 14-days post injection.

For imaging set up, mice were induced with 3% isoflurane and placed in a supine position in the $^1H/^{19}F$ quadrature coil. During imaging, mice were maintained at 37°C via a warm air blower and 1.5% isoflurane. ^1H images were acquired using a T_2-weighted FSE with a 0.28 × 0.28mm^2 in-plane resolution, 72 × 36 mm^2 FOV, 3000/20 ms TR/TE, 2 mm slice thickness, NEX = 3, and a total scan time of 1 min and 12 sec. ^{19}F images were attained with a FSE with a 1.1 × 1.1 mm^2 in-plane resolution, 1250/20.0 ms TR/TE, echo train length of 8 echoes, NEX = 128, and a matching FOV and slice thickness for a total of 10 min 40 s imaging time. Furthermore, to avoid isoflurane (ISO) anesthetic signal contamination that has been seen in other studies[157,158], a gaussian chemical saturation pulse at +2150 Hz (relative to the ^{19}F center frequency of PFCE) was added prior to RF excitation.

4.3.4 *Image Postprocessing and Analysis*

All image post processing was performed via MATLAB 2015b (Mathworks, Natick, MA). Phantom and *in vivo* images were first scaled to units of pixel signal-to-noise ratio (SNR) as expressed in Equation 4.1,

$$SNR = (0.655) \cdot S/\sigma \qquad [4.1]$$

where S is the pixel intensity value of the magnitude image, σ is the standard deviation of a noise measurement obtained from a region of interest (ROI) in the image background, and 0.655 is a correction factor to account for the Rician noise distribution of the background noise. Once scaled to SNR, the ^{19}F images were resized via a bicubic interpolation kernel to match the anatomic image size and overlaid with the ^{1}H images to produce composite images. For phantom images, the signal linearity with ^{19}F concentration with the PFCE containing vials was tested by plotting the nominal ^{19}F concentration against the mean SNR achieved in each of the 5 vials. Subsequently, a linear regression was performed to scale images to ^{19}F spins per voxel volume.

For the *in vivo* images, SNR-scaled ^{1}H/^{19}F images were first conservatively thresholded at an SNR of 4, to mitigate potential noise contributions to the signal measurements. The PFCE accumulation measurements were then calculated by first drawing ROIs along the visible boundaries of the tumor and within the liver for each mouse at all imaging time points. The mean SNR value within the tumor and liver was then calculated for each mouse at every imaging time point. To approximate the contrast agent clearance half-life and the time-to-peak concentration, the mean signal within the tumor and liver for the mice at each time point was then calculated and fit to a basic pharmacokinetic equation[159] (Equation 4.2), which relates the drug concentration at the site of interest with the time and absorption and elimination rates from the site.

$$y(t) = C\frac{\lambda_a}{\lambda_a - \lambda_e} \cdot \left(e^{-\lambda_e \cdot t} - e^{-\lambda_a \cdot t}\right) \qquad (4.2)$$

where y represents the estimated signal, which is proportional to the concentration, at some time, t, in days, λ represented the absorption and elimination rates from the site of interest, and C is a constant that describes the amount of the agent available to be absorbed.

4.4 Results

4.4.1 $^{1}H/^{19}F$ MRI

4.4.1.1 Phantom imaging

The ^{1}H phantom images (Figure 4.2A), as expected, demonstrated decreased ^{1}H signal with increased PFCE concentration, and thus decreased concentrations of water. ^{19}F phantom images, and accompanying plot (Figure 4.2B-C), highlight the linear relationship (R^2 =0.994) between the ^{19}F/PFCE NE concentration and the achieved ^{19}F signal within the vials. From the achieved SNR in each vial, a conservative detection limit of 8.8 mM PFCE was found for these particular scan parameters and voxel size.

4.4.1.2 In vivo imaging

Immunocompetent, female BALB/c mice were selected for this study along with murine 4T1-Luc cells in order to prepare a syngeneic mouse model. For this study an *in vivo* system with its full immune system was utilized to gain a comprehensive assessment of our collaborator's nanoemulsion formulation and obtain a natural, heterogeneous tumor environment without species incompatibility. Following tail vein injection of the novel PFCE NE, the mice displayed typical behavior without visible signs of pain or lethargy, suggesting a positive safety profile for our collaborator's formulation. Qualitatively, global spectroscopy indicated that the *in vivo* ^{19}F signal from the PFCE NE was much larger than the ISO signal, as can be seen in Figure 4.3. The resultant ^{19}F images indicated successful detection of the PFCE NE in all 5 mice across all timepoints, as seen in Figure 4.4.

These ^{1}H/^{19}F images provided detailed temporal information on the PFCE NE circulation, organ distribution, and tumor accumulation. As seen in the representative time course images from a single mouse (Figure 4.5), PFCE NE signal was clearly detected in the tumor, inferior vena cava, kidneys, spleen, liver, and heart. More specifically, at 6 hours post injection, ^{19}F signal was visible in many of the main organs following after a 10.5-minute acquisition. The greatest signal was seen in the liver and spleen but was also visible within the vasculature and highly perfused organ systems, including the inferior vena cava and the heart. In addition, a modest accumulation within the tumor and kidneys was observed.

At day 1 post injection, the PFCE NE was clearly seen within the tumor volume. At this point, the mouse kidneys and vasculature had cleared most of its transient NE accumulation; however, increased accumulation was seen within the tumor, liver, and spleen. After day 1, the PFCE NE signal was reduced, yet still visible within the tumor, in all mice out to day 14 post injection. Additionally, signal in the liver and spleen was decreased, yet still substantial in all mice, indicating some clearance by the reticuloendothelial system.

The PFCE NE concentration time course in the liver and tumor was quantified (Figure 4.6) and fit to simple pharmacokinetic equations (Figure 4.7A and B), to estimate the approximate time-to-peak and clearance half-life for both sites. The results suggest that the tumor and liver reach peak concentrations at 1.0- and 0.9-days post injection, respectively. Furthermore, we estimate that the PFCE NE has an estimated clearance half-life of 6.6 and 94.6 days post injection within the tumor and liver, respectively, which is over 50% shorter than reported in the literature for other PFCE NE formulations.[160]

4.5 Discussion

In this study, we have tested the *in vivo* tolerance and ^{19}F MRI detection of a novel PFCE nanoemulsion formulation in 4T1-Luc-bearing immunocompetent mice out to 14 days post injection. Furthermore, the passive tumor-targeting and liver accumulation was quantified, on average, for the 5 imaged mice. The prolonged PFCE signal accumulation within the tumor is a favorable characteristic that may allow longitudinal tumor imaging and analysis over with only minimal injections of the ^{19}F contrast agent. In brief, this novel NE formulation was able to stably encapsulate fluorine contents up to 35% (vol:vol) at 210 ± 32 nm particle size, where minimal to no particle growth (232 ± 39 nm) was seen out to 98 days post preparation.

The stability of our collaborators nanoemulsion, coupled with its high fluorine concentration is a unique feature. Typical lipid nanoemulsions undergrow relatively rapid particle growth due to Ostwald ripening, and other processes, like sedimentation or coalescence.[94,96,161] This NE's long term stability increases its potential for translation and use in cancer diagnostics, where a stable particle size can increase shelf life and imaging consistency. Furthermore, research suggests[151,162] that if the nanoemulsion particle size was adjusted to approximately 100-150 nm in diameter, recognition and sequestration by the reticuloendothelial system (RES), and thus uptake into the liver and spleen will be greatly reduced.

While this agent performed well during *in vivo* imaging and showed high stability across weeks of measurements, there are some limitations in this study. First, the *in vivo* sample size is fairly small, with only 5 subjects, which limits our statistical power, and thus analysis potential. Second, the *in vivo* imaging timeline was limited to 14 days, which could be extended further to include time points out to several weeks to characterize the PFCE NE clearance kinetics more accurately from the tumor, spleen, and liver. Several avenues can also be explored to improve the utility of this PFCE NE, like inclusion of a fluorescent dye to enable optical imaging techniques for validation of NE presence in the tumor and organs of interest.

In future collaborations, we will look to expand upon this work by actively targeting the tumor and exploring its potential as a theranostic agent. The first potential avenue of expansion will look to incorporate a tumor-targeting ligand to improve accumulation within the tumor volume and reduce accumulation in other vital organs like the liver or spleen. The second avenue will include research into the *in vivo* potential to both provide diagnostic imaging abilities as well as delivering a chemotherapeutic payload. Furthermore, the inclusion of a targeting ligand could potentially reduce the systemic toxicity associated with chemotherapy by both increasing uptake within the tumor volume and decreasing it within vital organs.

This work demonstrates the feasibility to incorporate our collaborator's stable, high fluorine content PFCE nanoemulsion in tumor-bearing mice for repeatable ^{19}F MRI over the course of 14 days. Furthermore, this work demonstrated a degree of passive tumor targeting via the EPR effect and approximates tumor and liver uptake/clearance timelines via ^{19}F MR image analysis. Future work will look to implement ^{19}F MRI for imaging of modified versions of our collaborator's formulation to assess active tumor targeting and/or theranostic potential.

4.6 Acknowledgements

This project was a collaborative effort led by Drs Sandro Mecozzi and Sean Fain. Postdoctoral researchers, Drs. Alexa Heaton and Montira Tangsangasaksri conducted were responsible for the nanoemulsion synthesis, dilution preparation, mouse tumor model development, and IV infusions. Additionally, they also provided expertise in pharmacology, chemistry, and cellular biology to assist in the interpretation of the experimental results. My (Lawrence Lechuga) responsibilities and contributions were to 1) conduct all phantom imaging experiments 2) handle and physically image all mice at all time points, 3) design, process, and interpret the phantom, spectroscopic, and *in vivo* fluorine MRI data of mice, and 4) provide my preclinical imaging expertise to interpret and aid in the design of the study. This project was supported in part by an AOF/SciMed GRS Fellowship to Lawrence M. Lechuga by the Office of Graduate Education, University of Wisconsin-Madison.

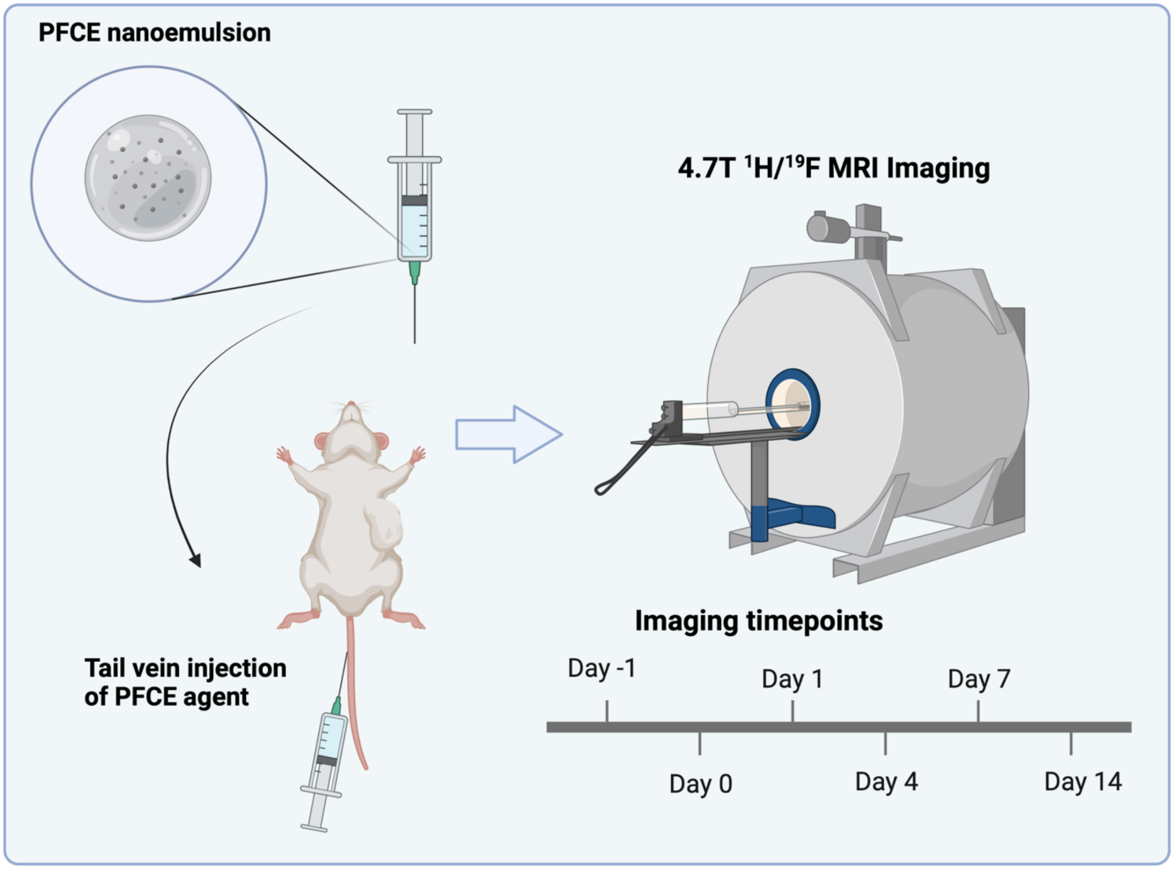

Figure 4.1: Graphical depiction of study design. *A graphical depiction is shown, where the PFCE nanoemulsion is delivered to (n=5) 4T1-Luc tumor-bearing BALB/c mice via IV tail vein injection, where they were imaged with* $^{1}H/^{19}F$ *MRI at 6 separate time points.*

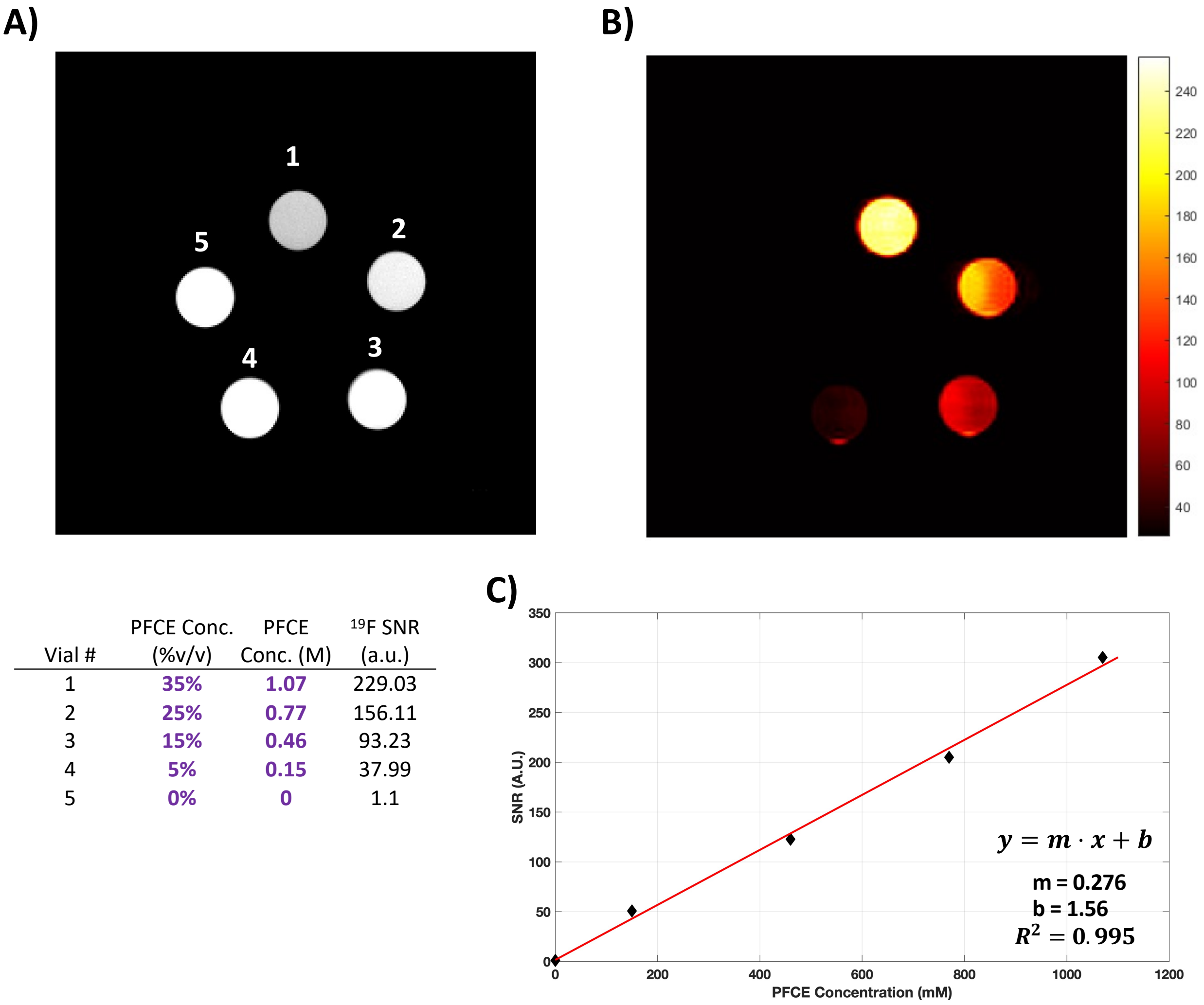

Vial #	PFCE Conc. (%v/v)	PFCE Conc. (M)	^{19}F SNR (a.u.)
1	**35%**	**1.07**	229.03
2	**25%**	**0.77**	156.11
3	**15%**	**0.46**	93.23
4	**5%**	**0.15**	37.99
5	**0%**	**0**	1.1

Figure 4.2: ^{1}H/^{19}F MRI of PFCE nanoemulsion phantoms. *A) Proton (^{1}H) and ^{19}F MR images of diluted PFCE nanoemulsion formulations, with the concentrations listed in the table on the bottom right panel. C) Linearity of the achieved SNR vs nominal ^{19}F concentration is shown via linear regression (R^2 >0.99).*

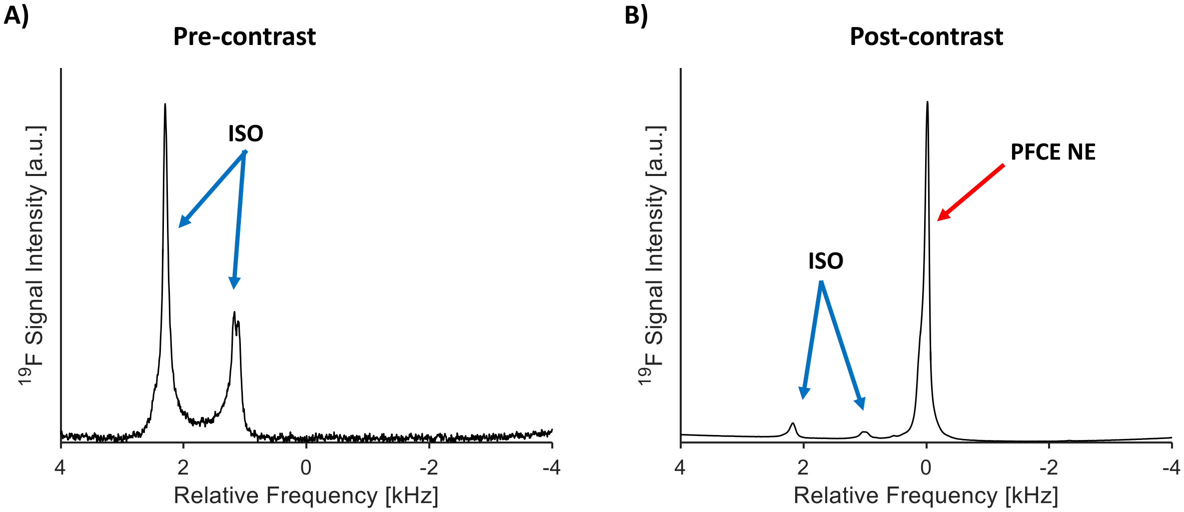

Figure 4.3: Pre- and Post-contrast in vivo ^{19}F PRESS spectroscopy. *In vivo spectra of 4T1-Luc bearing mice A) prior to and B) after contrast injections. The pre-contrast spectrum shows two peaks (blue arrows) from the isoflurane anesthetic uptake in tumor bearing mice. The post-contrast spectrum shows a much larger single resonance from the PFCE nanoemulsion (red arrow) relative to the isoflurane resonances.*

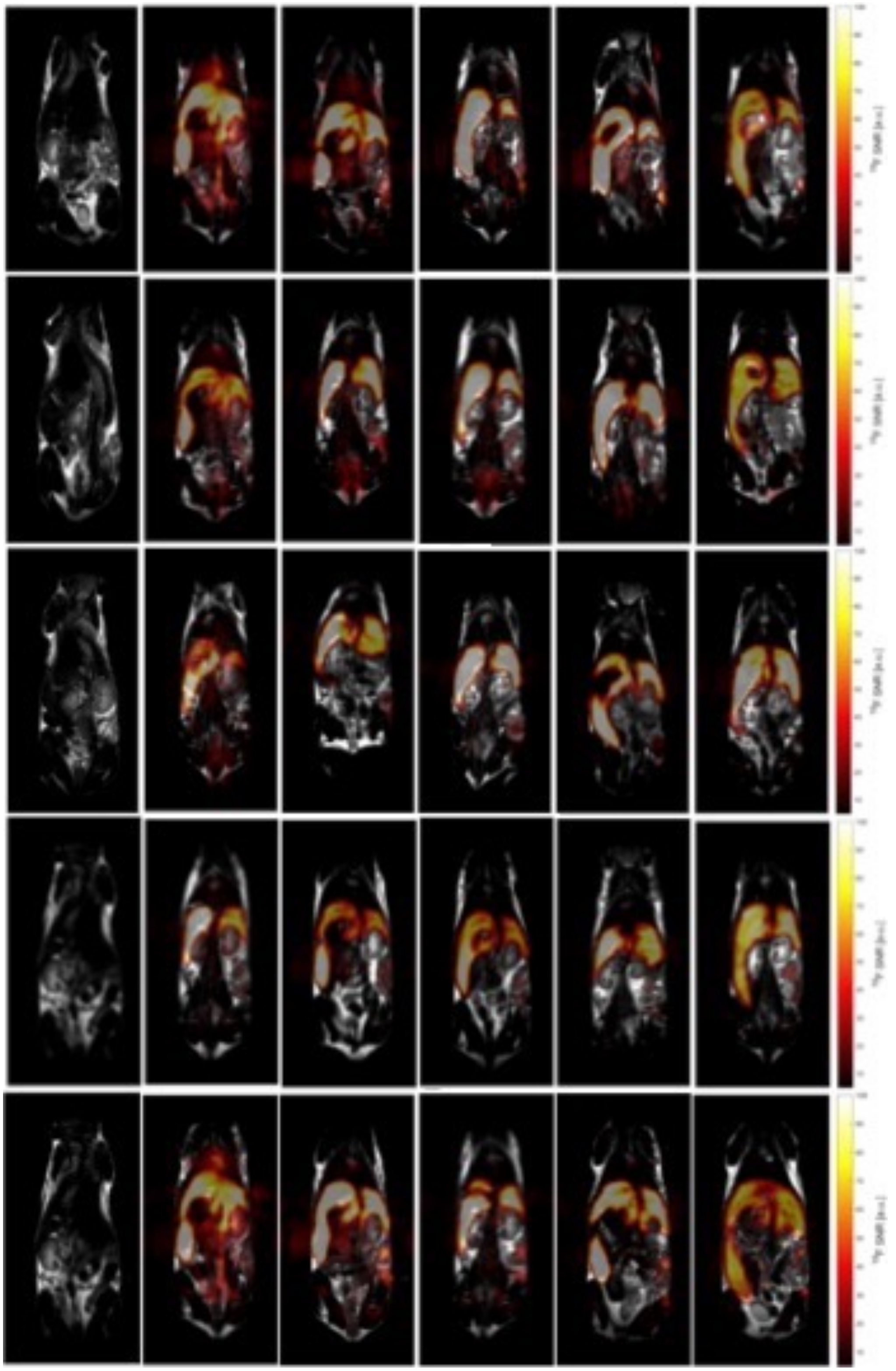

Figure 4.4: In vivo composite ^{1}H/^{19}F MRI of mice at several time points post-injection. *In vivo ^{1}H/^{19}F composite images of tumor-bearing BALB/c immunocompetent mice (n=5) pre- and post-injection of the PFCE nanoemulsion formulation. The anatomical, T_2-weighted ^{1}H MR images, are shown in grayscale with the SNR-scaled ^{19}F images shown in the 'hot' colorscale at six imaging time points. From left to right, the time points are -1 day, 6 hours, 1, 4, 7, and 14 days post injection, where each row represents a different mouse subject.*

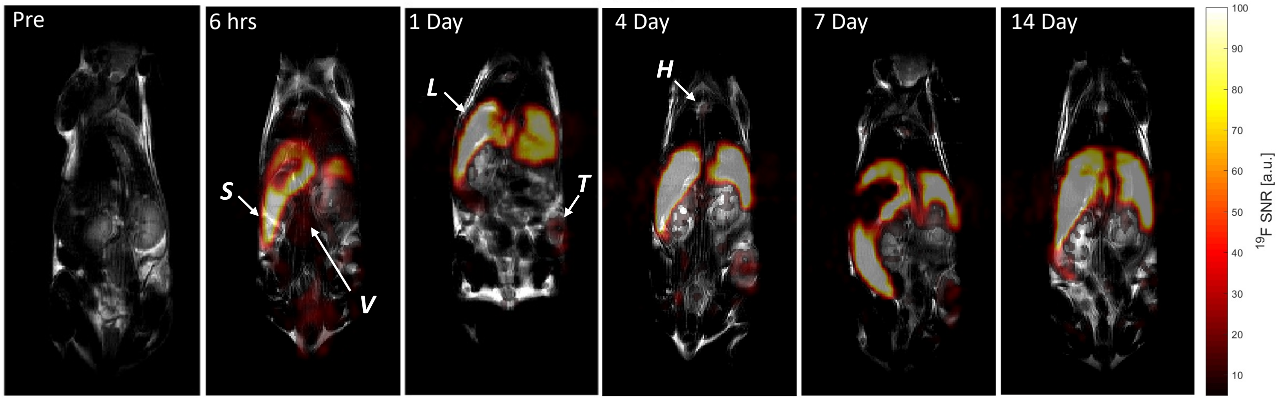

Figure 4.5: Representative coronal composite ^{1}H/^{19}F MRI of tumor-bearing mouse at multiple timepoints. *A representative coronal composite ^{1}H/^{19}F MR images of a 4T1-Luc bearing immunocompetent BALB/c mice after IV injection of a PFCE nanoemulsion, at 6 different time points. Accumulation of the agent within the spleen (S), inferior vena cava (V), liver (L), heart (H), and tumor (T), is indicated by the white arrows within the image.*

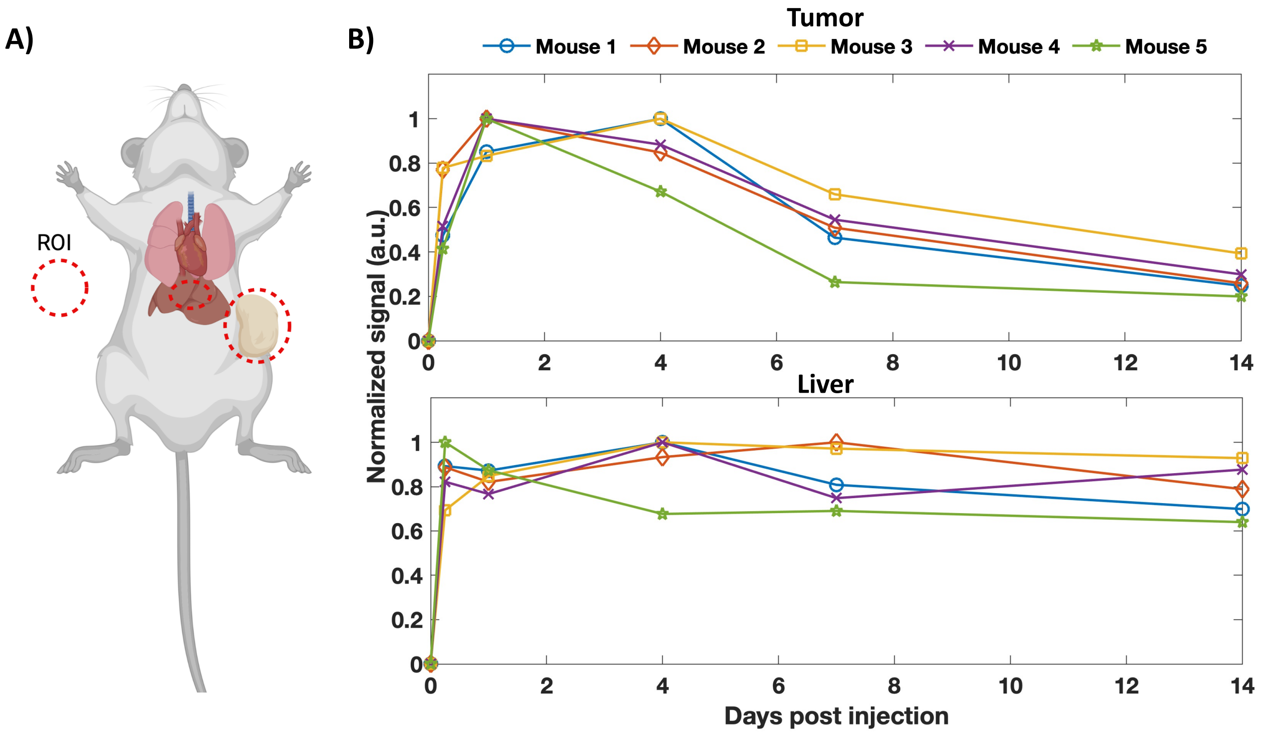

Figure 4.6: ROI selection and quantification plots of PFCE nanoemulsion uptake within the tumor and liver of mice across time. *A) Graphic illustrating the ROI selection and relevant mouse anatomy to aid liver and tumor measurements. B) Plots demonstrating the tumor uptake within the tumor (top) and liver (bottom) for tumor-bearing mice (n=5), across 14 days. Uptake within these sites were quantified using ROI analysis, as seen represented in the mouse illustration (right).*

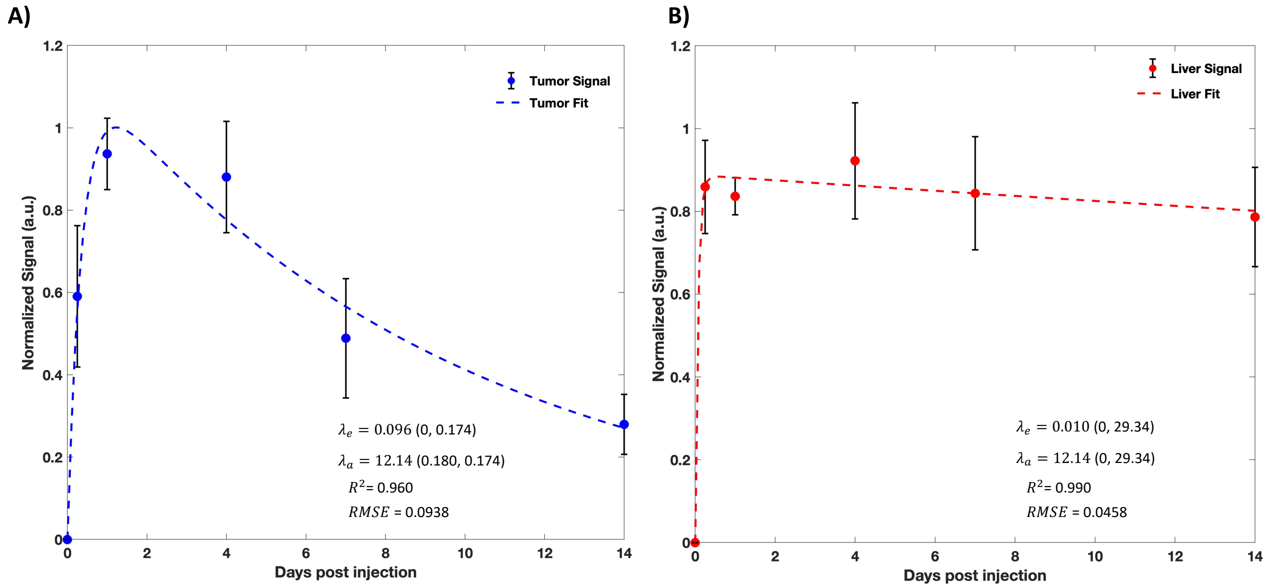

Figure 4.7: Average time course ^{19}F signal within tumor and liver of mice injected with PFCE emulsion. *The average 19F signal accumulation (solid circles) in the A) tumor and B) liver of the (n=5) mice injected intravenously with PFCE NE at each time point. The experimental data was fit to a basic pharmacokinetic equation (dashed lines) to determine the approximate absorption (λ_a) and elimination (λ_e) rates in the liver and tumor site.*

Chapter 5 PULSE SEQUENCES AND OPTIMIZATION PARAMETERS FOR CELL TRACKING USING FLUORINE-19 MRI AT 3T

Additional Contributors: Paul Begovatz, PhD; Monica Cho; Christian Capitini, MD

Note: Portions of this work is currently being prepared for submission in Journal of Magnetic Resonance in Medicine (MRM impact factor: 4.67).

5.1 Abstract

Purpose: The purpose of this work is threefold: 1) present methodology to perform fluorine-19 (^{19}F) MRI on a 3T clinical MRI system, 2) optimize and validate the parameter selection for a ^{19}F agent to maximize the SNR-efficiency for SPGR, bSSFP, phase-cycled bSSFP (bSSFP-C), and accelerate GRAPPA-enabled bSSFP-C, and 3) demonstrate detection feasibility *ex vivo*.

Methods: Bloch simulations were conducted for PFPE to determine the theoretical parameter choices to maximize SNR-efficiency for two gradient echo-based sequences. Theoretical parameter choices were then experimentally verified and the sensitivity of the 3 sequences of interest were compared head-to-head for a 10-minute acquisition. Feasibility of GRAPPA-based acceleration was also demonstrated in both a phantom and *ex vivo* model for the bSSFP-C acquisitions.

Results: Simulations predicted that flip angles (FA) of approximately 12 and 64 degrees would maximize the signal for SPGR and bSSFP. Validation of optimal FA and receiver bandwidth showed close agreement with Bloch simulation. Under the optimal parameters, a sensitivity of 2.47, 5.81, and 4.44 $\text{ms}^{-0.5}\text{mM}^{-1}$ and a detection limit of 20.3, 1.5, and 20.3 mM was achieved for SPGR, bSSFP, and bSSFP-C, respectively. bSSFP and bSSFP-C achieved significantly greater sensitivity than SPGR. A scan time reduction of 2.1 was achieved *ex vivo* with the parallel imaging accelerated bSSFP-C with minimal image quality degradation.

Conclusions: bSSFP, demonstrated significantly greater SNR-efficiency than the other sequences, but was prone to off-resonance banding artifacts. bSSFP-C was able to greatly reduce banding but

requires additional time. This time penalty was mitigated by implementing bSSFP-C with parallel imaging.

5.2 Introduction

Immunotherapies and adoptive cell transfer (ACT) therapies have grown in popularity in recent decades.[90,163] While there are many clinical trials around the world conducting ACT therapies, there remains high variability in clinical outcomes[164] and limited success in solid tumors.[165] This may be partially due to the inability to track and assess the biodistribution of the adoptively transferred cell population after treatment.[100,111] The United States Food and Drug Administration (FDA) has published guidelines[11] highlighting the need to incorporate a form of cellular imaging to assess cell survival and biodistribution at all stages of therapeutic product development. Currently, there is a lack of immunotherapeutic-specific biomarkers that can assess treatment efficacy, early on.[36] This further suggests that the development of a non-invasive molecular imaging platform to track and quantify these cells *in vivo* throughout treatment can provide useful information to improve efficacy.[35]

Fluorine-19 (^{19}F) MRI is one imaging modality that can be utilized to track and monitor *ex-situ* or *in situ* labeled lymphocytes for days to weeks at a time. Labeling of these cells is accomplished by way of injection or *ex vivo* incubation with biologically inert perfluorocarbon (PFC) nanoemulsions.[13] Given the low endogenous fluorine concentration in host tissue, resultant images will provide specific, positive contrast images, not corrupted by background signal. In the preclinical setting, this imaging modality has successfully tracked and labeled various immune cells such as macrophages[59,72], T- and chimeric antigen receptor (CAR)-T cells[10,12,63,166], natural killer (NK) cells[61,62,116], and dendritic cells (DC).[75] While there are considerably fewer cell tracking studies performed in a clinical setting, one particular study[65] demonstrated clinical applicability by tracking labeled adoptively transferred DCs in 5 patients over 24 hours post-injection.

Although ^{19}F MRI has intrinsically high specificity, the fluorine concentration that can be reasonably achieved *in vivo* leads to low sensitivity. Efforts to improve sensitivity have included the use of high ^{19}F molarity agents, such as perfluoropolyether (PFPE)[63], compressed sensing[134], and sequence optimization. Among the clinically suitable ^{19}F agents, PFPE is particularly attractive because of its high fluorine content, simple resonance spectrum, and commercial availability. To maximize the signal-to-noise ratio (SNR) efficiency or SNR_{eff}, pulse sequences and their respective parameters need to be chosen carefully. Recent work from Colotti et al. characterized the relaxation times of 3 common PFCs under various conditions and provided a theoretical parameter optimization of multiple pulse sequences at 3T using a small 35 mm birdcage coil.[167]

One such sequence strategy is to employ the use of fast, SNR-efficient sequences, such as fast spin-echo (FSE), variants of gradient recalled echoes (GRE), ultrashort echo time (UTE), and balanced steady-state free precession (bSSFP). In bSSFP imaging[42], the balanced gradients across a TR create a large steady-state magnetization that is particularly appealing for ^{19}F MRI. As theoretically demonstrated in previous work[96], bSSFP produced the greatest SNR-efficiency for acquisitions under relaxation times in the ranges of the most common ^{19}F contrast agents, like PFPE and PFCE. While bSSFP's signal efficiency and utility has been demonstrated for small animal MRI systems and birdcage coil designs in previous works[128,167], implementation for large field of view imaging on clinical MRI systems and for transmit/receive multi-channel ^{19}F MRI coil designs may present challenges due to B_1 and B_0 inhomogeneities. Given the well-known sensitivity to off-resonance artifacts of bSSFP[168], signal-nulls can become problematic for longer TRs and less than ideal field homogeneity. One strategy to mitigate the off-resonance banding in bSSFP is known as phase cycling[169], where 2 or more acquisitions at different RF phase combinations are used to shift the location of signal nulls. Upon completion, the two acquisitions are combined in either a maximum intensity projection (MIP) or sum-of-squares reconstruction.[170]

The feasibility of and sequence optimization for ^{19}F MRI using cellular tracking probes on clinical MRI systems is under-studied, especially for body imaging applications using a multi-channel array coil. Human-sized single-channel birdcage coils for brain applications allow for simpler direct quantification, but they are not suitable for typical body imaging applications due to limited bore size and SNR. Moreover, given the low intrinsic sensitivity of ^{19}F MRI, the scan time can often be exceedingly long. However, with multichannel coils parallel imaging (PI) techniques, like GRAPPA[171], can provide a significant reduction in scan time with minimal image quality degradation. The purpose of this work is to: 1) present a methodology to perform ^{19}F MRI on a 3T clinical MRI platform with modified product sequences, 2) optimize and validate the parameter selection for PFPE to maximize the SNR-efficiency for SPGR, bSSFP, phase-cycled bSSFP (bSSFP-C), and accelerated GRAPPA enabled bSSFP-C.

5.3 Methods

5.3.1 *PFPE Phantoms Construction*

PFPE (Celsense, Pittsburgh, PA) phantoms were constructed by first mixing low melting point agarose powder (Sigma Aldrich; St Louis, MO) and water at 2% (w/w) and combining with PFPE at various concentrations. After dissolution of the agar, 1.5 mL aliquots of 16.0, 8.0, 4.0, 2.0 mg/mL of PFPE agar solution were added to 1.5 mL centrifuge tubes. Each vial was vortexed for 1 minute to ensure adequate mixing and stored upright while cooling. The approximate ^{19}F concentration of reference vials 1-4 are 166.1, 70.0, 41.5, and 18.3 mM, respectively.

5.3.2 *Numerical Simulations*

To determine the parameters that would maximize signal acquisition efficiency for SPGR and bSSFP, numerical simulations were conducted via MATLAB 2020a (Mathworks, Natick, MA). The theoretical signal response was modeled for on-resonance acquisitions for a TR range of 1-100 ms and flip angles (FA) spanning 1-90° at the previously measured room temperature relaxation times. The theoretical signal acquisition efficiency, ϵ, was calculated for the range of TR and FA, according to Equation 5.1:

$$\epsilon \propto \frac{\xi(\alpha, TR)}{\sqrt{TR}} \quad [5.1]$$

Where $\xi(\alpha, TR)$ is the maximum theoretical signal achieved by the sequence for a flip angle, α, and repetition time, TR. Heatmaps of the efficiency were generated to determine the theoretical Optimal flip angle and TR that maximized the efficiency and to compare the relative performance between the sequences. Given the sensitivity of bSSFP to off-resonance banding artifacts, the signal as a function of phase accumulated across an arbitrary TR was modeled for phase alternating and non-alternating bSSFP.

5.3.3 ***Relaxation Measurements***

All imaging data were acquired using a 3.0T Discovery MR750w MRI scanner (GE Healthcare, Waukesha, WI) with an 8-channel $^{1}H/^{19}F$ transmit/receive torso coil (MRI.TOOLS, Berlin, Germany), shown in Figure 1A-C. To characterize the longitudinal (T_1) and transverse (T_2) relaxation times for PFPE (Celsense, Pittsburgh, PA), a concentrated 2 mL vial of room temperature PFPE was placed inside the field of view (FOV), along with 15 liters of sealed agar bags (2% w/w, KCl: 30 mM). To measure T_1, a spectroscopic inversion recovery (IR) FID sequence was prescribed with a TR = 3000 ms, NEX = 64, and 12 inversion times ranging from 19 to 3000 ms. Similarly, the transverse relaxation time (T_2) was measured using a spectroscopic spin-echo sequence with matching TR and NEX, and echo times ranging from 20-1000 ms. The T_1 and T_2 data were then processed by phasing, apodizing with a Lorentzian filter, zero-filling, and baseline correcting each spectrum. The main resonance peak of the processed PFPE spectra was then integrated to give the total signal achieved. The total signal was then plotted against its respective IR or TE to generate the characteristic T_1 and T_2 relaxation curves. Using a nonlinear least-squares fitting, the T_1 and T_2 curves were fit to Equations 5.2A-B, respectively.

$$M(IR) = M_0\left(1 - A \cdot e^{-\frac{IR}{T_1}}\right) \qquad [5.2A]$$

$$M(TE) = M_0 \cdot e^{-\frac{TE}{T_2}} + C \qquad [5.2B]$$

5.3.4 ***Manual prescan procedure***

Before the acquisition of any ^{19}F images, a manual prescan procedure was performed to set the center frequency and the transmit gain (TG) setting. The central frequency was set using a 1D free induction decay (FID) sequence, FID CSI. A nominal 90° selective RF pulse was used to excite a highly concentrated vial of PFPE. With the ^{19}F power spectrum displayed, the operating frequency was then adjusted until the main PFPE peak was on resonance. Within the built-in manual prescan (MPS), a 1-cycle sinc pulse with a nominal flip angle of 90-degrees and pulse width of 3.2 ms was used to excite the PFPE vial. Using the console-displayed power spectrum, the TG was increased until a maximum signal amplitude was achieved, signifying that a 90° flip has been achieved. After this 90° flip angle calibration, the ^{19}F sequences can be prescribed, where the scan RF pulse will be automatically attenuated to the desired FA, according to Equation 5.3.

$$\eta = -200 \cdot \log\left[\frac{\alpha}{90^\circ}\right] \qquad [5.3]$$

Where η is the required RF attenuation, in units of 0.1 dB, and α is our desired flip angle.

5.3.5 ***Optimal flip angle and receiver bandwidth validation***

To ensure a realistic and reproducible setup with consistent loading and impedance matching, the 15 liters of agar were placed within the coil along with the 4 reference PFPE phantom vials and a highly concentrated vial (approx. 1.0 M) for calibration purposes, as shown in Figure 5.1D. To ensure that the experimental Optimal flip angles are near their predicted locations, validation studies were performed. Conventional images were acquired using a 2D ^{1}H SPGR with a FA of 20°, TR/TE = 34/3.288 ms, FOV of 400×400 mm^2, $256 \times 256 \times 12$ acquisition matrix, and 3.2 mm slice thickness. Multinuclear-enabled 3D bSSFP, hereafter referred to as FIESTA, and SPGR sequences were prescribed with an rBW = 10 kHz, matching FOV and slice thickness, 128 × 128 × 12 acquisition matrix, and minimum TR/TE. For each successive acquisition, the flip angle was increased to span flip angles between 0-30° and 30-90° for SPGR and FIESTA, respectively. Additional scan parameters can be found in Table 5.1. From the resulting images, the SNR within Vial 1, corrected for its multichannel bias, was calculated. The resulting FA with the greatest achieved SNR, for each sequence, will be used in all future acquisitions at that combination of TR/TE and rBW.

Table 5.1: Relevant sequence parameters for SPGR, FIESTA, and FIESTA-C. *Sequence parameters are listed for the theoretical sequence parameter validation.*

Sequence	Predicted Angle	Flip Angles	TR/TE (ms)	rBW
SPGR	11.8	5-30	9.2/3.9	10 kHz
FIESTA	63.9	40-90	8.4/4.1	

Similarly, various rBW values were then tested to determine which choice produced the most SNR-efficient acquisition, while minimizing any artifacts. For SPGR and FIESTA, 5 receiver bandwidths ranging from 3-50 kHz were acquired with the minimum TR/TE at their respective predicted optimal flip angle. The qualitative image quality and both the SNR and SNR_{eff} were evaluated in Vial 1 to determine the most efficient and robust choice.

5.3.6 *Sequence Comparisons*

Using the ideal imaging parameters found for SPGR and FIESTA, the sequences were compared for their maximum achieved SNR efficiency. The 2 sequences, including a phase-cycled version of FIESTA, also known as FIESTA-C, were prescribed with the previously determined optimal FA, TR/TE, and rBW, where their NEX was set such that the scan time was approximately 10 minutes, the scan time deemed clinically practical. Conventional images were acquired using a 2D ^{1}H SPGR with a FA of 20°, TR/TE = 34/3.288 ms, FOV of 400 × 400 mm^2, 256 × 256 × 30 acquisition matrix, and 3.2 mm slice thickness. All ^{19}F acquisitions were performed with a matching FOV and slice thickness, and an acquisition matrix of $128 \times 128 \times 30$. Additional sequence parameters for these acquisitions are listed in Table 5.2. The resulting images were processed and the normalized SNR_{eff}, hereafter "the sensitivity", was assessed for each of the 4 PFPE vials and compared against one another. Additionally, the linear relationship between SNR and ^{19}F concentration was exploited and a linear regression was performed to extrapolate the lower limit of detection for each of the 3 sequences, where an SNR of 4 was defined as a conservative detection cutoff limit.[172]

Table 5.2: Relevant sequence parameters for SPGR, FIESTA, and FIESTA-C comparisons. *Sequence parameters are listed for the optimized sequences for sensitivity assessment and comparison.*

Sequence	NEX	Flip Angle	TR/TE (ms)	rBW	Scan Time
SPGR	13	12	9.2/3.9	10 kHz	9:42
FIESTA	15	65	8.4/4.1		10:14
FIESTA-C	7	65	8.4/4.1		9:32

5.3.7 ***Accelerated ^{19}F FIESTA-C MRI***

To demonstrate the feasibility of acceleration with parallel imaging (PI) techniques on a clinical multichannel coil, Autocalibrating Reconstruction for Cartesian (ARC) enabled FIESTA-C was performed. ARC is similar to Generalized Autocalibrating Partially Parallel Acquisitions (GRAPPA)[171]; the signal is acquired for each coil element where multiple phase encoding steps are skipped, based upon the nominal acceleration factor (R), to reduce scan times. For the ARC implementation, the center of k-space is sampled fully and additional lines within the region, known as the autocalibration signal (ACS) are acquired during the image acquisition. The ACS is then used to automatically generate weighting factors for each coil element, which along with a local 3D kernel, are used to iteratively estimate the missing k-space lines.

In a similar fashion to the non-accelerated sequence comparison acquisitions, the ARC-enabled ^{19}F FIESTA-C data was acquired by loading the coil with the agar bags and the 4 PFPE reference vials. Conventional reference images were acquired using a 2D ^{1}H SPGR with a FA of 20°, TR/TE = 34/3.288 ms, FOV of 400×400 mm^2, $256 \times 256 \times 38$ acquisition matrix, and 3.2 mm slice thickness. ^{19}F FIESTA-C images were acquired with 2 phase cycles at nominal acceleration factors between R = 1 (control reference) and 4 with FOV, acquisition matrix, and slice thickness matched to the SPGR sequence, TR/TE = 8.4/4.076 ms, FA = 65°, NEX = 7, and an rBW = 10 kHz, where additional imaging parameters can be found in Table 5.3. As described in the postprocessing section, ^{19}F images were registered to ^{1}H images, and masks were generated to segment out each vial in the ^{19}F image. Given the spatially varying noise enhancement seen in parallel imaging acquisitions, SNR measurements are nontrivial; therefore, to assess the perceived image quality of the accelerated image relative to the unaccelerated control, the structural similarity index (SSIM), according to Equation 5.4, was calculated for each accelerated acquisition.

$$SSIM(x,y) = \frac{(2\mu_x \cdot \mu_y + c_1)(2\sigma_{xy} + c_2)}{(\mu_x^2 + \mu_y^2 + c_1)(\sigma_x^2 + \sigma_y^2 + c_2)} \qquad [5.4]$$

The SSIM was computed between the control x and the accelerated image y, where μ is the average, σ^2 is variance, σ_{xy} is the covariance, and c_1 and c_2 are constants set to stabilize the denominator. The SSIM is a metric designed to provide a quantitative image quality assessment in comparison to a reference or control image, where studies have demonstrated that it performs similarly to trained human observers on evaluating perceived image quality.[173,174]

Table 5.3: Experimental acceleration factors tested for ^{19}F ARC-enabled FIESTA-C phantom acquisitions, where an acceleration factor of 1.0 serves as the control.

Phase encode (y) acceleration	Phase encode (z) acceleration	Nominal Acceleration (R)	Scan Time	Scan Time Reduction Factor
1.0	1.0	1 .0	9:32	1.0
1.25	1.0	1.25	7:54	1.21
1.5	1.0	1.5	6:56	1.38
1.75	1.0	1.75	6:16	1.52
2.0	1.0	2.0	5:40	1.68
2.5	1.25	2.5	5:04	1.88
3.0	1.5	3.0	4:55	1.94
3.5	1.75	3.5	4:46	2.00
4.0	2.0	4.0	4:38	2.06

5.3.8 *Image Postprocessing*

5.3.8.1 Registration and vial segmentation

All image postprocessing and analyses were performed using MATLAB 2020a. Composite ^{1}H/^{19}F images were created for the sequence comparison acquisitions using control point registration with a similarity transform that allowed for translation, rotation, and scaling. To create masks for each of the 4 vials in the FOV, ^{1}H images were smoothed with an edge-preserving median filter and an edge image was subsequently generated with a Sobel filter. Morphological operators were then applied to close, fill, erode, and label each of vial masks.

5.3.8.2 Multichannel SNR bias corrections

From the resultant masks, the mean value, $\overline{M_\iota}$, was calculated for each vial within the FOV of the non-accelerated ^{19}F images. Raw magnitude noise measurements were taken by placing a large rectangular ROI in a region devoid of signal where the average value, $\overline{N}_8$, was then calculated. As discussed in Constantinides et al.[175], under the assumption of no noise correlations the noise magnitude theoretically follows a central chi-squared (χ^2)-distribution with $2n$ degrees of freedom, given by Equation 5.5:

$$p_c(N_n) = \frac{2}{(\sigma\sqrt{2})^{2n}(n-1)!} N_n^{2n-1} e^{-\frac{N_n^2}{2\sigma^2}} \tag{5.5}$$

Where N_n is the pixel intensity in a region noise only, and n is the number of channels in the coil. The mean value for this χ^2-distribution for n = 8 channels is $\bar{N} = 3.94\sigma$, where σ is the estimate of the true noise variance. The average value within the noise ROI, $\bar{N}$, was then corrected using this relationship to arrive at an estimate for the true noise variance.

While this correction addresses the bias seen in the central χ^2- distributed noise, the bias seen in regions containing signal will need to be corrected as well. Due to the root-sum of squares (RSS) combination of the data from each channel in the coil, the resultant ^{19}F magnitude images will overestimate the true SNR achieved in low signal regions. The uncorrected SNR within our vial ROIs, $\frac{\overline{M_\iota}}{\sigma}$ will be subject to a noncentral χ^2-distribution[175,176] given by Equation 5.6:

$$p(M_n) = \frac{A_n}{\sigma^2}\left(\frac{M_n}{A_n}\right)^n e^{-\frac{[(A_n^2+M_n^2)}{2\sigma^2}]} I_{n-1}\left(\frac{M_n \cdot A_n}{\sigma^2}\right) \tag{5.6}$$

Where $I_{n-1}$is modified Bessel function of the first kind and A_n represents the total pixel intensity in the absence of noise contributed by all n-elements. The relationship between the mean uncorrected SNR and the estimate for the true SNR, $\frac{A_8}{\sigma}$, can be exploited by calculating the first moment of Equation 5.6, given by:

$$\frac{\bar{M}_n}{\sigma} = \frac{\prod_{i=1}^{n} 2n-1}{2^{n-1}\cdot(n-1)!}\sqrt{\frac{\pi}{2}}\ {}_1^1F\left(-\frac{1}{2},\ n,\ -\frac{A_n^2}{2\,\sigma^2}\right) \tag{5.8}$$

Where ${}_1^1F$ is the confluent hypergeometric function. Given the transcendental nature of the equation, the estimate of the true SNR can be solved numerically for a given measured SNR. As seen in Figure 5.2A, the bias seen in the measured SNR becomes increasingly large at lower measured SNR but is relatively small at SNR > 15; therefore, correction factors (Figure 5.2B) will be applied to measured SNRs ≤ 15 where the bias is greater than 5%. Using the corrected true SNR estimate, the normalized SNR-efficiency, hereafter referred to as sensitivity, was calculated for each detected vial according to Equation 5.9:

$$S = \frac{SNR}{C_F \cdot V_{vox} \cdot \sqrt{TR \cdot NEX}} = \frac{SNR_{eff}}{C_F \cdot V_{vox}} \quad [ms^{-0.5} \mu mol^{-1}] \qquad [5.9]$$

Where C_F is the concentration of PFPE in µmol/mm^3 for each vial, V_{vox} is the volume of the voxel, and NEX is the number of excitations or averages.

5.3.8.3 Ex vivo feasibility

An *ex vivo* canine limb was utilized as an experimental phantom to demonstrate the ability to detect PFPE within soft tissue. The limb was donated after the canine patient underwent osteosarcoma treatment and subsequent tumor biopsy and limb amputation. Four 200 µL PFPE injections of varying concentrations were injected into the rear canine limb along the proximal tibia. The concentrations of injection sites 1-4, shown in Figure 5.1F, were approximately 11, 32, 69, and 142 mM of PFPE in phosphate-buffered saline (PBS), respectively. Directly after injection, the limb was placed within the coil, as seen in Figure 5.1E, with the agar bags and reference vials 3 and 4 (41.5 and 18.3 mM, respectively) were taped to the surface of the limb.

Anatomic ^{1}H images were acquired using a 2D coronal Fast Spin Echo (FSE) with a TR/TE = 533/5.848 ms, four echoes, FOV of 400 × 400 mm^2, 256 × 256 × 20 acquisition matrix, and 3.2 mm slice thickness**.** Afterward, without disturbing the imaging setup, the ^{1}H module was replaced with the ^{19}F module and the multinuclear manual prescan was conducted. Non-accelerated and accelerated ^{19}F FIESTA-C images were acquired with matching FOV and slice thickness. Both accelerated and non-accelerated images were acquired, with additional scan parameters listed in Table 5.4.

Table 5.4: Relevant sequence parameters for FIESTA-C ex vivo acquisitions. *The sequence parameters for ^{19}F FIESTA-C with and without ARC acceleration are listed for the ex vivo imaging sessions.*

Sequence	NEX	Flip Angle	TR/TE (ms)	rBW	Scan Time
SPGR	13	12	9.2/3.9	10 kHz	9:42
FIESTA	15	65	8.4/4.1		10:14
FIESTA-C	7	65	8.4/4.1		9:32

5.3.9 *Statistics*

All statistical analyses were performed using GraphPad Prism (GraphPad Software; San Diego, CA). For comparison of 3 or more groups, a one-way ANOVA was performed. Any statistically significant findings underwent Tukey's honestly significant differences post hoc tests. Any findings with a p-value < 0.05 were considered statistically significant. Reported measurements represent the mean value ± SD.

5.4 Results

5.4.1 *Numerical simulations*

The resulting Bloch simulations for SPGR and bSSFP, shown in Figure 5.3, demonstrate that the signal acquisition efficiency for a fixed scan time will be maximized with the lowest possible TR. Empirically, TR_{min} is determined by the lowest possible rBW without creating artifacts, and the FA is chosen accordingly. Therefore, TR_{min} becomes a function of the chosen rBW for a set acquisition matrix. Meanwhile, FIESTA demonstrated a stable optimal angle of 63.8° that was independent of the choice of TR. SPGR's Optimal flip angle varied between 8-16° for TRs between 4.1-15.6 ms, where the range of TRs chosen for simulation represent the minimum TRs available on the 3T scanner used for experiments with an acquisition matrix of $128 \times 128 \times 30$.

5.4.2 ***Relaxation measurements***

The results of the curve fitting ($R^2 > 0.99$), shown in Figure 5.4, demonstrate the characteristic relaxation curves, where T_1 and T_2 were determined to be 424 and 165 ms, respectively, which is in close agreement with previous work by Colotti et al.[167]

5.4.3 ***Flip Angle Validations***

The resultant corrected SNR measurements from the Optimal flip angle and bSSFP optimized flip angle validation scans were then plotted against their manually calibrated flip angles, along with the theoretical signal curve on a relative axis, shown in Figure 5.5. The results indicate experimental optimal flip angles of 11° and 65° at a fixed TR/TE of 9.2/3.9 ms and 8.4/4.1 ms for SPGR and FIESTA, respectively. The results show close agreement with theoretical predictions. These experimental FA values were used for the remaining experiments.

Receiver bandwidth testing revealed that all receiver bandwidths tested produced some banding artifact; empirically, much more significant banding was seen at rBW < 10kHz. Although SPGR demonstrated increased SNR with decreased rBW as expected, where the choice of rBW = 5 kHz demonstrated the best SNR_{eff}, rBW = 10 kHz presented the best tradeoff between SNR_{eff} and artifact, as seen in Figure 5.6, and was used for the remainder of the studies.

5.4.4 ***Sequence Comparisons***

The performance of SPGR, FIESTA, and FIESTA-C is demonstrated in Figure 5.7A-C, where SPGR produced images with minimal artifact but demonstrated lower SNR over all of the vials in the FOV. As expected, FIESTA demonstrated very high levels of SNR across the vials but had visible off-resonance banding artifacts. FIESTA-C produced images with minimal banding artifacts compared with its non-phase cycled counterpart at reduced. However, FIESTA-C had substantially improved SNR relative to SPGR.

As seen in Figure 5.7D, FIESTA produced the highest sensitivity of 5.81 $ms^{-0.5}\mu mol^{-1}$, followed by FIESTA-C with a mean sensitivity of 4.44 $ms^{-0.5}\mu mol^{-1}$, with SPGR having the lowest sensitivity of 2.47 $ms^{-0.5}\mu mol^{-1}$. Results of the multiple comparisons determined that FIESTA-C produced significantly greater sensitivity than SPGR by a factor of 1.8 ($p<0.01$) and that FIESTA outperformed both SPGR and FIESTA-C by a factor of 2.3 ($p<0.001$) and 1.3 ($p<0.05$), respectively. The lower limit of detection was then determined, as seen in Figure 5.7E, for each of the sequences. For a 10-minute scan time under the optimized parameters, FIESTA, FIESTA-C, and SPGR, produced ^{19}F detection limits of 1.5, 6.2, and 20.3 mM, respectively.

5.4.5 ***Accelerated ^{19}F FIESTA-C***

ARC-enabled ^{19}F FIESTA-C acquisitions, seen in Figure 5.8A-D, were tested over a nominal acceleration range from 1 to 4 for nominal scan times ranging from approximately 10-4 minutes. Qualitatively, images show no discernible differences in the detection of any of the 4 vials within the FOV. The resultant SSIM (Figure 5.8E) for each accelerated acquisition, were >0.99, demonstrated the close similarity between the accelerated and non-accelerated control images. Furthermore, a maximal scan time reduction of 2.1 was achieved without any discernible image quality degradation.

5.4.6 ***Ex Vivo Canine ^{19}F FIESTA-C***

Results from the *ex vivo* canine ^{19}F FIESTA-C MRI without acceleration are shown in Figure 5.9A and demonstrate the ability to detect injection sites 2-4, which ranged from 32-142 mM of PFPE in PBS. However, the 10-minute acquisition was unable to detect signal from injection site 1 (11 mM) for any scan. A mean SNR of 4.8, 8.3, and 15.5 was achieved for injection sites 2, 3, and 4, where a linear regression ($R^2>0.999$) predicted a minimum detection limit of 24 mM of PFPE in this *ex vivo* imaging model.

For R = 2 (Figure 5.9B), similar performance to the non-accelerated acquisitions was demonstrated while reducing scan times by a factor of 1.7. Acceleration was limited to R = 2 due to the small slice encoding matrix required for coverage of the upper limb. The SSIM index averaged across the 3 slices containing signal was 0.997, demonstrating high perceived similarity in the images.

5.5 Discussion

To our knowledge, this is the first study to demonstrate a workflow for optimizing product sequences and parallel imaging for ^{19}F MRI cell labeling and body imaging applications on a clinical 3T platform. In this study, bSSFP sequences were shown to outperform SPGR for a common PFC nanoemulsion measured at the clinically relevant field strength of 3T. Specifically, experimentally verified relaxation times for PFPE, along with Bloch simulations were used to determine the optimal TR and FA to maximize the signal acquisition efficiency for PFPE using both SPGR and FIESTA sequences. Simulations were verified experimentally for feasible high performing choices of FA, TR, TE, and rBW, and compared head-to-head for a fixed 10-minute scan time where relative sensitivity and detection limits were quantified and compared. The achieved sensitivities clearly show the benefit of a bSSFP/FIESTA approach for PFPE, but the presence of severe banding artifact present across a wide range of rBW choices necessitated adoption of phase-cycling. The Phase-cycled SSFP technique, or FIESTA-C, showed a modest reduction in sensitivity compared to FIESTA, demonstrating an approximately 1.8-fold increase in sensitivity compared to SPGR and the ability to mitigate the banding artifacts. The feasibility of ARC parallel imaging detection was further demonstrated in both phantoms and *ex vivo* using FIESTA-C, where this choice was motivated by the strong performance with respect to SNR_{eff} with minimal banding artifact.

PFPE was chosen for this study due to its high ^{19}F content, the lowest T_1 of the more common PFC agents, and exhibits a relatively simple resonance structure. For this reason and its relatively rapid clearance, the PFPE agent has been utilized in various cell tracking and inflammation studies.[177–179] However, an alternative agent, perfluoro-15-crown-5-ether (PFCE), has a single resonance line and high ^{19}F content and has been used in many preclinical studies.

Moreover, Colotti et al. showed that PFCE has a greater T_2/T_1 relaxation ratio, which makes it more suitable for a bSSFP approach.[167] Potential toxicity due to PFCE's long persistence in the liver and spleen precludes its use in clinical imaging studies[160] although recent work has shown the ability to reduce the *in vivo* biological half-life 15-fold by modifying the nanoemulsion structure making this agent of potential interest for future clinical development.[180]

FA calibration utilizing a modified version of GE's built-in manual prescan (MPS), was reliably achieved for the commercially available PFPE agent and multi-channel ^{19}F torso coil which was able to realize stable optimized FA's matched to predicted values within 1-1.5°. Practical tradeoffs in rBW and TR in the presence of B0 inhomogeneities were demonstrated, with banding artifact mitigated effectively using the FIESTA-C acquisition. While the acquisition of multiple phase cycles improved image quality for FIESTA-C, the increased acquisition time inherently reduces the sensitivity under a maximum intensity projection combination of the two phase-cycles. An alternate approach to boost the achieved sensitivity would seek to combine the multiple phase cycles using a sum of squares approach.[181,182] As expected, a reduction in sensitivity was seen moving to an *ex vivo* model. However, as the *ex vivo* PFPE detection limit is within a biologically relevant range, these results support the motivation to advance this work to an adoptive cell transfer feasibility study in an *ex vivo* canine model. Furthermore, with the application of the ARC acceleration techniques to the FIESTA-C acquisitions, the time commitment was significantly reduced without any discernible image quality degradation in either phantom or *ex vivo* acquisitions.

This presented work also has its limitations. First, the theoretical optimizations and validations of sequence parameters are demonstrated for PFPE at room temperature, but given the relaxation times' temperature dependence, the optimal parameters will likely shift accordingly. However, the provided methodology could be extended to a more relevant biological temperature, and even different PFC emulsions, such as PFCE. Secondly, the parallel imaging evaluation is fairly qualitative and therefore impedes the use of quantitative metrics of performance like SNR or CNR. The non-trivial spatial noise amplification that occurs during the reconstruction in GRAPPA and SENSE acquisitions requires the use of the g-factor.[183] Future work will aim to determine g-factor maps that will allow for a more comprehensive analysis of the ARC-enabled FIESTA-C performances in phantom and *ex vivo* setups. Finally, given the more complex nature of a clinically sized phased array coil, it was imperative to implement a flip angle calibration procedure to ensure the nominal flip angle was in close agreement with the desired flip angle. Although this MPS process can be performed in as little as 5-10 minutes, an automated Bloch-Siegert approach[184] would be more efficient and precise and is left for future work.

In conclusion, this work demonstrates the greater relative SNR-efficiency of bSSFP with phase-cycling (FIESTA-C) compared to bSSFP and SPGR sequences for PFPE acquisitions at 3T. Improved SNR performance with FIESTA-C was confirmed in an *ex vivo* model using parallel imaging.

5.6 Acknowledgements

Acknowledgements

This project was a collaborative effort led by Dr Sean Fain. Postdoctoral researcher, Dr. Paul Begovatz was responsible for developing the agar phantoms that were used for the imaging studies. Dr. Begovatz also provided his expertise in translational imaging to assist in experimental design, study coordination, and troubleshooting. My (Lawrence Lechuga) responsibilities and contributions were to 1) perform pulse sequence development of the 3D GRE-based sequences, 2) develop a manual prescan protocol for quality assurance, 3) design, gather, and process phantom and *ex vivo* fluorine MRI data, 3) develop a quality assurance protocol for *in vivo* imaging of labeled cells, and 4) provided my imaging expertise to assist in the interpretation and design of the study.

This work was supported by grants from the a National Cancer Institute/National Institutes of Health (NCI/NIH) R01 CA215461 (L.M.L, S.B.F., and C.M.C.), University of Wisconsin Carbone Cancer Center Cancer Immunotherapy/Tumor Immunology pilot grant (D.M.V., C.M.C., and S.B.F.), Hyundai Hope on Wheels, American Cancer Society Research Scholar grant RSG-18-104-01-LIB (S.B.F. and C.M.C.), St. Baldrick's – Stand up to Cancer Pediatric Dream Team Translational Research Grant SU2C-AACR-DT-27-17 and the MACC Fund (C.M.C). We would like to thank the UWCCC Small Animal Imaging and Radiotherapy core facility, which is supported in part through NCI/NIH P30 CA014520. The St. Baldrick's Foundation collaborates with Stand Up to Cancer. Stand Up to Cancer is a division of the Entertainment Industry Foundation. Research Grants are administered by the American Association for Cancer Research, the Scientific Partner of SU2C. The contents of this article do not necessarily reflect the views or policies of the Department of Health and Human Services, nor does mention of trade names, commercial products, or organizations imply endorsement by the US Government.

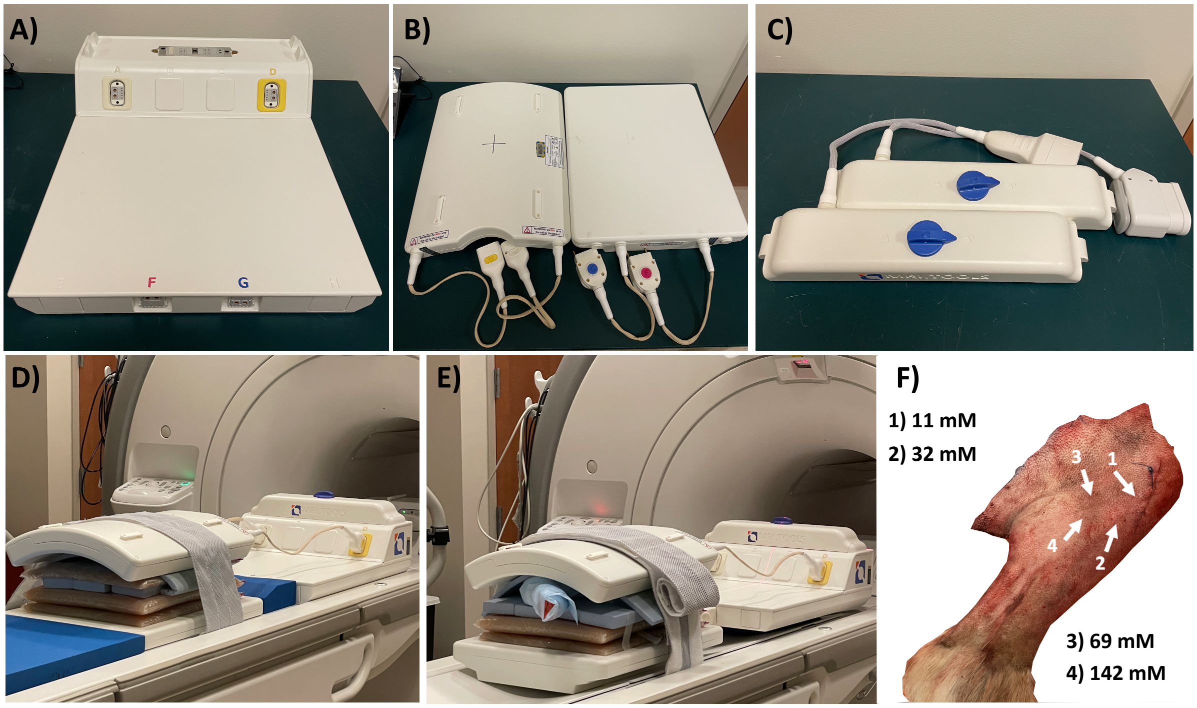

Figure 5.1: Dual-tuned ^{1}H/^{19}F MRI coil and setup. *The 8-channel dual tuned ^{1}H/^{19}F transmit/receive **A)** coil interface, **B)** anterior and posterior coils, and **C)** ^{1}H and ^{19}F modules. **D)** The phantom measurements setup, **E)** the canine ex vivo setup, and **F)** the approximate location of the 4 injection sites within the canine limb.*

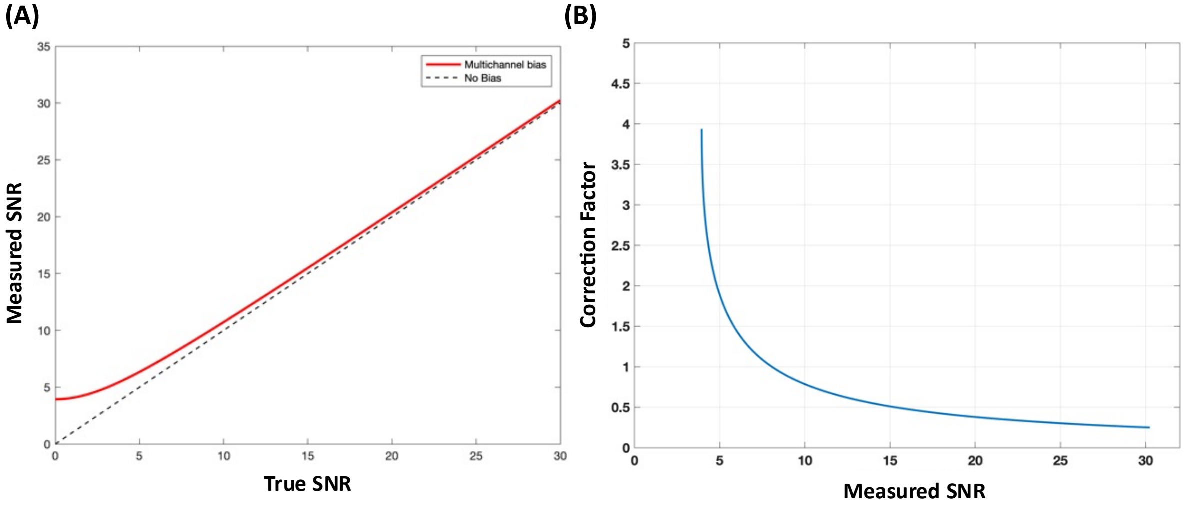

Figure 5.2: Bias in measured SNR for multichannel coils. *(A) The multichannel bias (red) increasingly deviates from the unbiased scenario (dashed) as the measured SNR decreases. (B) The correction factor required to adjust the measured SNR to the true SNR estimate*

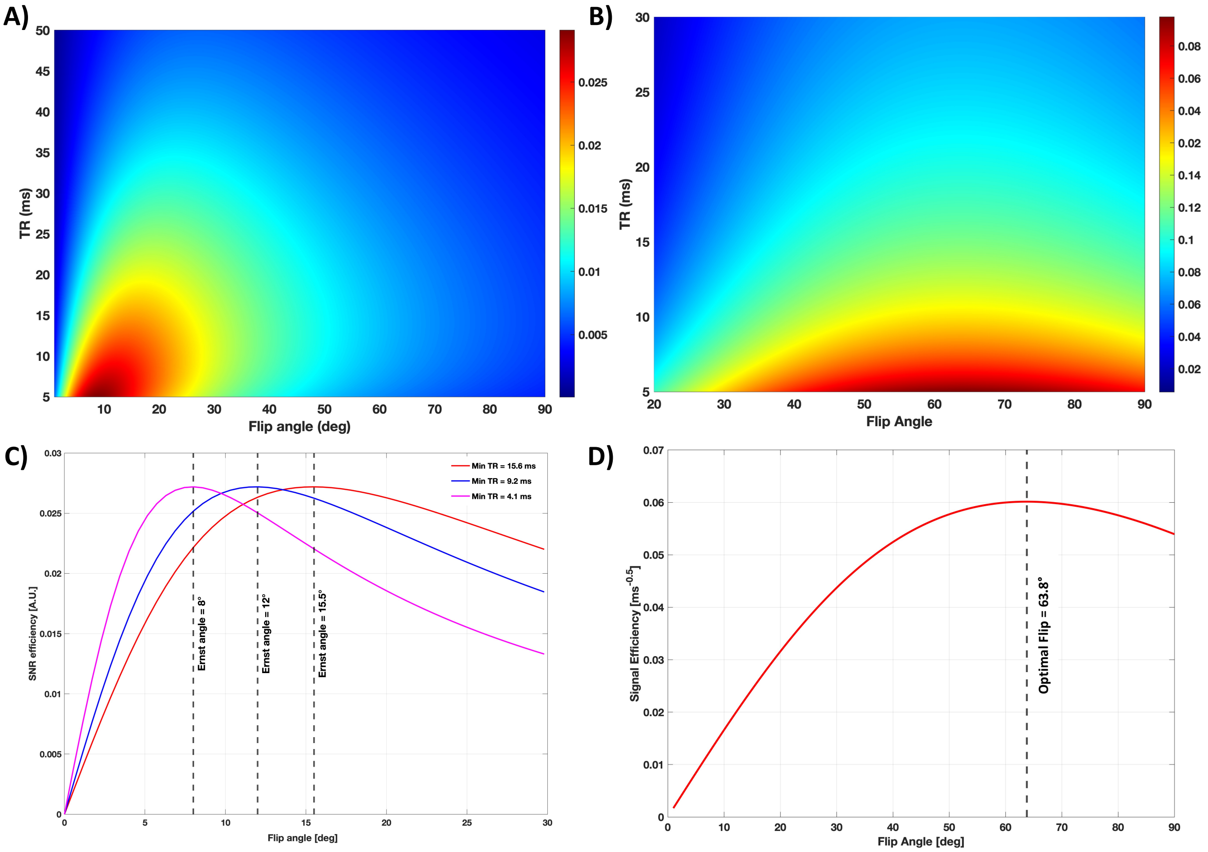

Figure 5.3: Bloch Simulations for SPGR and FIESTA of room temperature PFPE agent at 3T. *A theoretical signal acquisition efficiency colormap was generated via Bloch simulations to determine the optimal theoretical flip angle and repetition time for* ***(A)*** *SPGR and* ***(B)*** *FIESTA pulse sequences for room temperature PFPE at 3T, where the scale bar represents the efficiency in units of* $ms^{-0.5}$. ***(C)*** *Profiles of SNR efficiency at 3 different TRs were plotted against flip angle to demonstrate the dependency of TR on the theoretical optimal flip angle for SPGR sequences.* ***(D)*** *Profile of SNR efficiency for a TR to demonstrate the optimal flip angle for the FIESTA sequence. Maximal SNR efficiency is seen at minimal TR and between 8-16 degrees for SPGR and 64 degrees for FIESTA.*

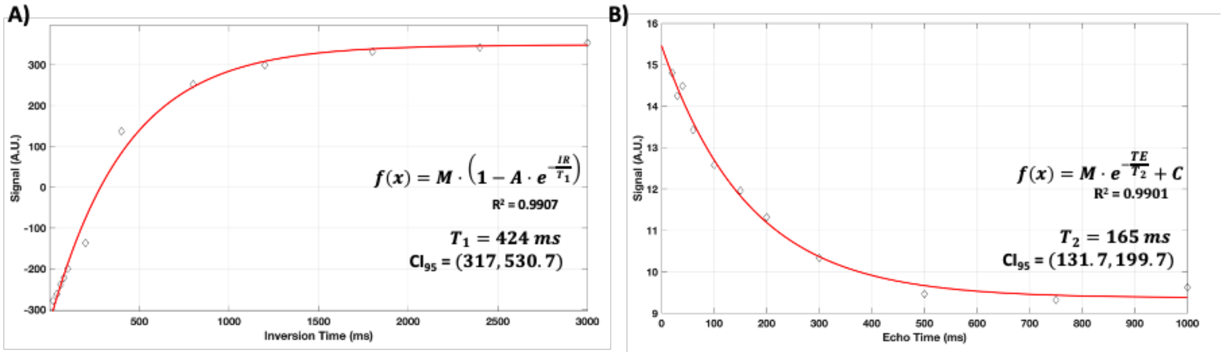

Figure 5.4: Relaxation measurements of room temperature (24℃) PFPE at 3T. (A) *Longitudinal relaxation times* (T_1) *were measured using a spectroscopic inversion recovery (IR) FID sequence with inversion times* (τ) *ranging from 15- 3000 ms and a TR of 3000 ms.* ***(B)*** *Transverse relaxation times* (T_2) *were measured (n=11) using a spectroscopic spin-echo sequence with echo times (TE) ranging from 20-1000 ms with a TR of 3000 ms. The main PFPE resonance line was integrated over in the resulting spectra and plotted against its corresponding* τ *or TE, where monoexponential curve fitting was performed*. T1 and T2 were found to be 424 and 165 ms, respectively. *Note: R-squared values > 0.99.*

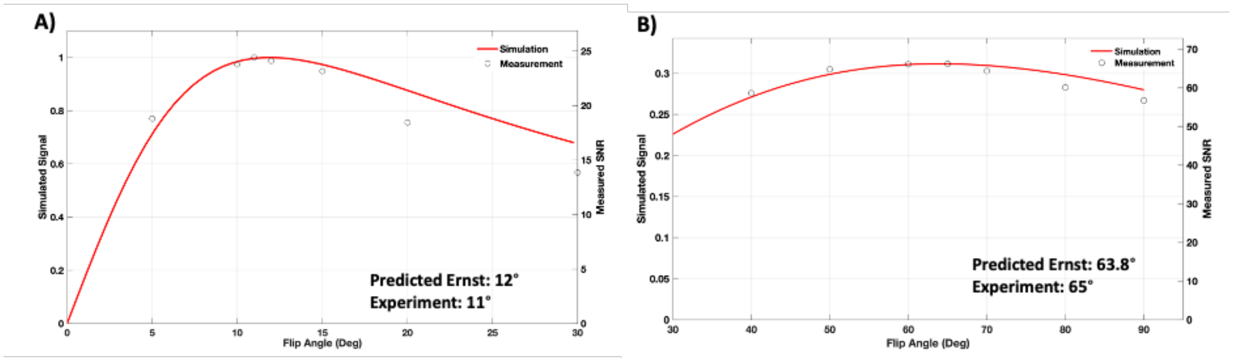

Figure 5.5: Flip angle validation for SPGR and FIESTA acquisitions of room temperature PFPE at 3T. *Validation of theoretical optimal flip angle predictions for **(A)** SPGR with TR/TE = 9.2/3.9 ms and optimized flip angle for **(B)** FIESTA acquisitions (TR/TE = 8.4/4.1 ms), where SNR was measured in a single vial of room temperature PFPE agent across a range of flip angles. Theoretical predictions (red line left scale) and experimental results (black circles right scale) show close agreement with a predicted Optimal flip angle of 12 degrees and optimal flip angle of 63.8 degrees and measured optimal flip angle of 11 and optimal flip angle of 65 degrees for SPGR and FIESTA, respectively.*

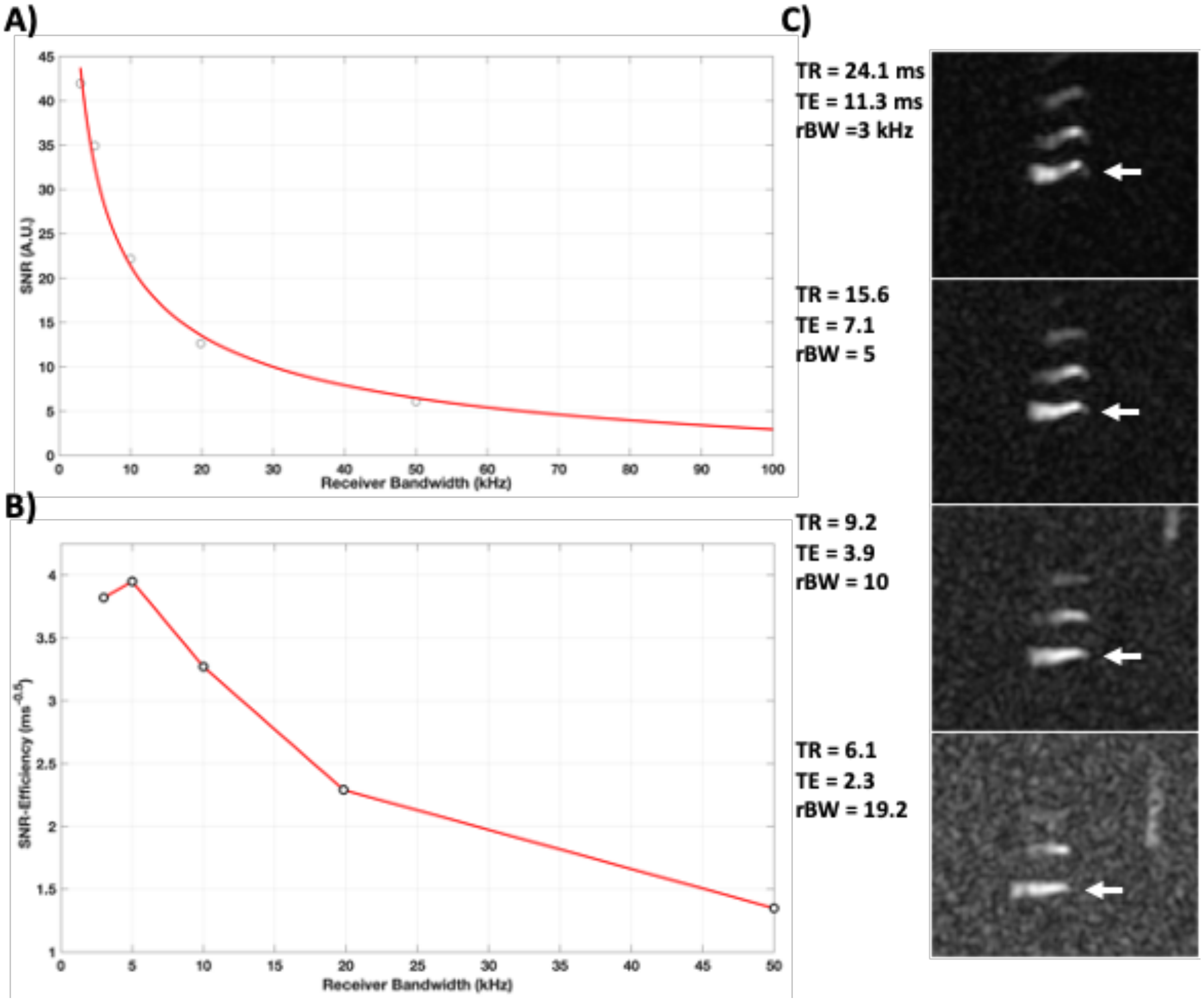

Figure 5.6: Selection of receiver bandwidth to maximize SNR efficiency for SPGR. (A) *SNR and* ***(B)*** *SNR-Efficiency for PFPE at 3T was measured at receiver bandwidths ranging from 3-50 kHz at the minimum TR/TE achievable.* ***(C)*** *^{19}F images demonstrate increased SNR with decreased rBW, but SNR-efficiency reaches a maximum at 5 kHz. Geometric distortions of the vials (white arrow) are also seen when rBW ≤ 5 kHz; therefore, an rBW of 10 kHz will be used to maximize SNR without introducing artifact.*

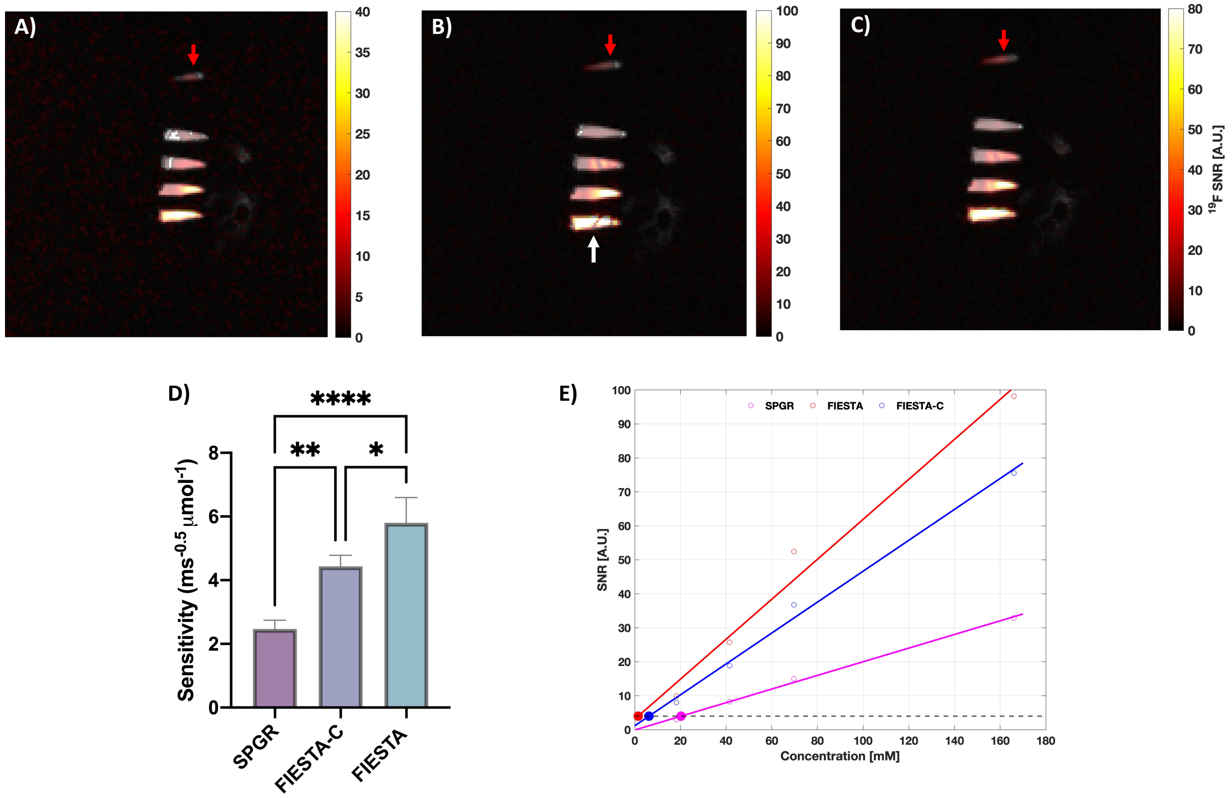

Figure 5.7: Assessment of SNR-efficiency SPGR, FIESTA, and FIESTA-C. *Zoomed, SNR-scaled registered coronal* ***(A)*** *SPGR,* ***(B)*** *FIESTA, and* ***(C)*** *FIESTA-C composite ^{1}H/^{19}F images were acquired using optimal parameters for a 10-minute scan.* ***(D)*** *The apparent SNR$_{eff}$ was calculated for each of the 4 PFPE vials and compared using a non-parametric repeated measures ANOVA test. Tukey's multiple comparisons test indicated a statistically significant increase in SNR$_{eff}$ for FIESTA-C compared with an SPGR acquisition. The white arrow indicates a region of significant banding artifact and red arrows represent a small reference vial of PFPE.* ***(E)*** *Detection limits, where an SNR of 4 was considered the limit, were calculated for each sequence. Note: * represents $p<0.05$, ** represents $p<0.01$, and **** represents $p<0.0001$.*

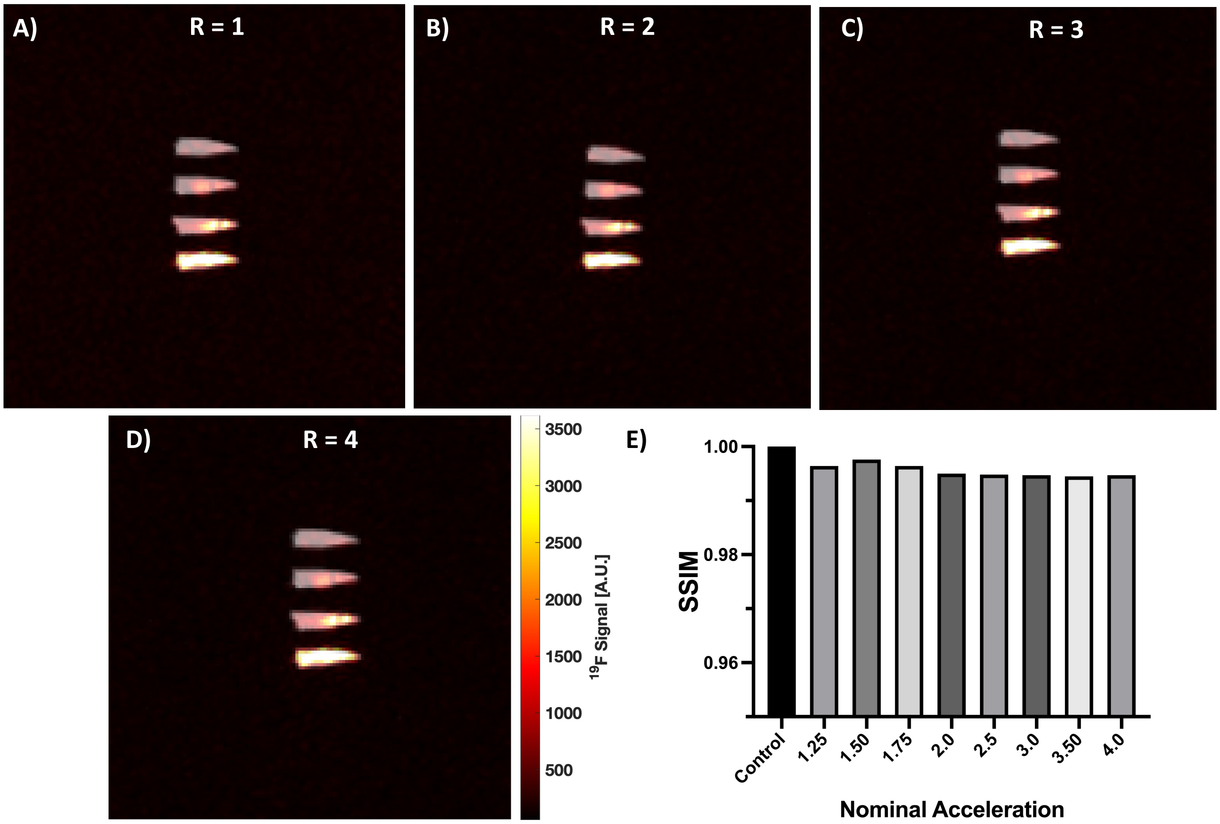

Figure 5.8: Composite ^{19}F ARC-enabled FIESTA-C phantom images. (A-C) *Composite ^{1}H/^{19}F MR images for ARC-enabled FIESTA-C acquisitions for nominal acceleration values, R, ranging from 1 (control) to 4 for four PFPE phantoms of varying concentration.* ***(E)*** *Structural similarity index (SSIM) demonstrated similarity in each of the accelerated images relative to control, with SSIM values greater than 0.99 for each.*

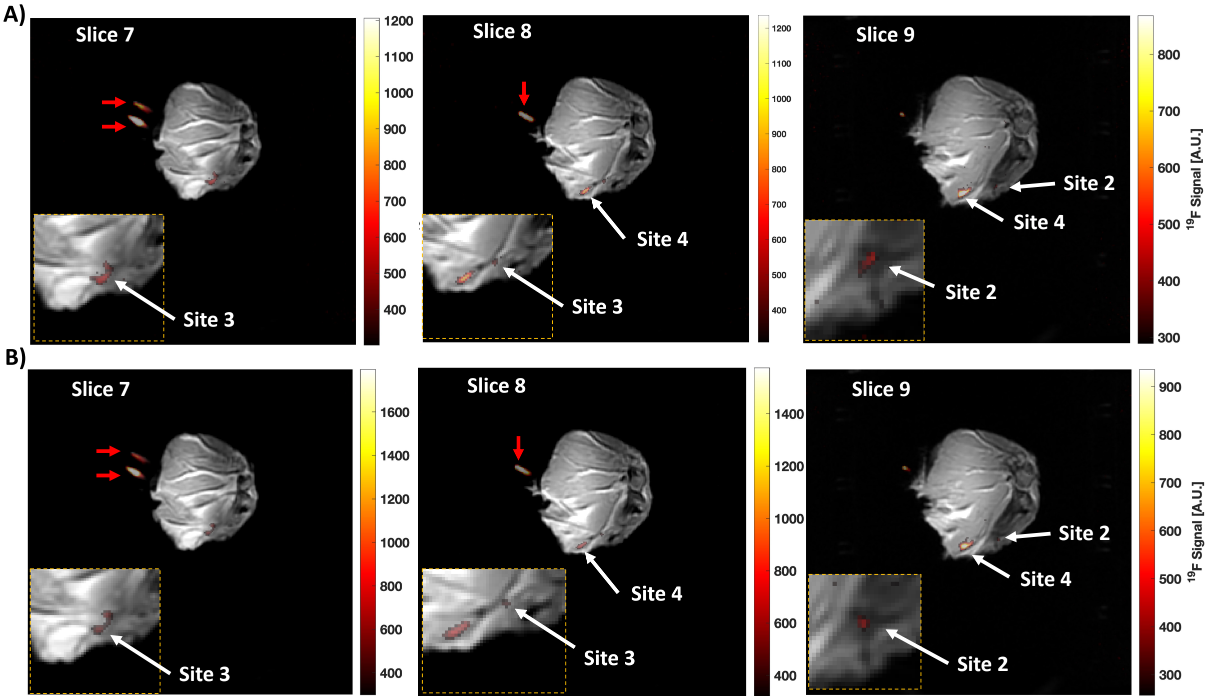

Figure 5.9: Ex vivo non-accelerated and accelerated FIESTA-C composite images. *^{1}H/^{19}F FIESTA-C composite images of **A)** non-accelerated and **B)** accelerated (R = 2) ARC-enabled FIESTA-C acquisitions in an ex vivo canine limb. In slices 7-9, injections sites 2, 3, and 4 were detectible, as denoted with white arrows; however, site 1 was not visible in any of the acquisitions. Orange-dashed cutouts in each slice depict zoomed-in window leveled images of the injection sites. Red arrows depict the location of 2 reference vials taped to the limb. Each slice was window leveled individually for visualization purposes.*

Chapter 6 SUMMARY AND FUTURE WORK

6.1 Summary

Cancer is one of the leading causes of death worldwide. As immunotherapy has emerged as a new paradigm for treatment of metastatic and refractory cancers, implementing *in vivo* cellular imaging techniques has become more vital for its continued growth and application. Cellular imaging in ACT can provide valuable prognostic information that can inform treatment decisions, such as dose and treatment timing, tumor infiltration, and evaluation of treatment efficacy early into treatment. This dissertation document details the development, translation, and application of cellular tracking techniques. More specifically, the contributions from our preclinical collaborative projects include:

- Characterization and tracking of ^{19}F-labeled murine T cells within a metastatic melanoma model after subcutaneous and intravenous injections.
- Evaluation of the enhanced permeability and retention (EPR) effect and estimation of the clearance and uptake times of a new PFCE nanoemulsion formulation in fast growing 4T1-Luc mammary carcinomas.
- Characterization of *in vitro* labeling effects, ^{19}F MRI detection, *in vivo* quantification, and postmortem validation of ^{19}F-labeled murine NK cells within EL4 lymphoma out to 6 days intratumoral post injection.

In addition to the preclinical projects, translational projects on a clinical 3T system have also been conducted with contributions that include:

- Conversion and development of multinuclear pulse sequences and manual prescan protocols to enable fluorine-19 MRI on an 8 channel transmit receive coil at 3T.

- Parameter optimization and assessment of performance and sensitivity of a spoiled gradient echo (SPGR), balanced SSFP (bSSFP), and phase-cycled bSSFP for common ^{19}F contrast agent at 3T
- Feasibility demonstrations to detect and accelerate a ^{19}F-enabled 3D phase-cycled bSSFP in a PFPE phantom and *ex vivo* canine model.

Overall, this dissertation demonstrates advancements in preclinical ^{19}F MRI for cellular tracking and provides both the foundational development and workflow necessary to begin ^{19}F MRI projects on a clinical multichannel platform at 3T.

6.2 Future Work

6.2.1 *Human monocyte tracking*

This future aim seeks to apply ^{19}F MRI cellular tracking techniques to adoptively transferred monocytes in an acute radiation syndrome (ARS) mouse model. ARS is an 'acute' illness caused by high doses of ionizing radiation to the entire, or most, of the body within a short period of time, on the order of minutes or hours.[185] The high doses of radiation to the body can damage and kill mitotically-active cells that are more radiosensitive, such as lymphocytes, erythrocytes, and GI cells.[186] ARS can manifest in a variety of ways, but can be divided into 3 subsyndromes which include hemopoietic, gastrointestinal, and neurovascular syndrome.[187] Patients receiving approximately 4 Gy of radiation only have a 50% chance of survival with current treatment protocols[188], which highlights the need for improved therapies for hematopoietic ARS (H-ARS).

Recent work from our collaborators have demonstrated a cellular therapy approach to treat H-ARS and extend survival in lethally irradiated mice.[189,190] Our collaborator's approach, in brief, was to first educate human monocytes with specialized mesenchymal stem cells (MSC), then deliver these MSC's to xenogeneic mice after they received a lethal dose of 4 Gy. Mice receiving this treatment showed improved hematopoietic recovery and overall survival relative to control, suggesting potential clinical translation. To better understand the cell tracking behavior of these therapeutic educated monocytes, ^{19}F MRI can be applied. Utilizing the methodology described in this dissertation document, we would aim to label with a PFCE agent (Cenya Imaging, Amsterdam, NL), characterize the effects, track cell migration, and quantify these human monocytes within lethally irradiated mice.

Our preliminary data has demonstrated the ability to label and image these human monocytes with ^{19}F MRI. The average labeling, shown in Figure 6.1, was found to be 0.6, 1.4, 3.7, and 4.9×10^{11} ^{19}F nuclei/cell at 2, 4, 8, and 10 mg/mL for 4 hours. Feasibility of human monocyte detection with ^{19}F MRI after intravenous injection into a lethally irradiated mouse was demonstrated at day 0 and 3 post injection. As shown in the representative composite images in Figure 6.2, signal was initially detected near the right axial lymph node, with signal appearing in subsequent time points near the heart and left axial lymph nodes. Future efforts in this project area would look to expand this feasibility study to show *in vivo* proof of principle to track and quantify injected human MSC's within multiple irradiated mice and compare with control non-irradiated mice.

6.2.2 *Canine NK cell tracking at 3T*

This future aim looks to extend the 3T translational multichannel ^{19}F MRI techniques to *in vivo* canine osteosarcoma (OSA) patients. OSA is the most common bone cancer in both humans and dogs, with a 10-fold increased frequency in canines.[191] While some progress has been made in treatment, little improvement in survival has been achieved, where 30-40% of children and >90% of canines do not survive this disease.[192] Canines offer a few distinct advantages over other animals, as a model for human OSA due to the biological complexity of the dogs, similar environmental factors, potential molecular similarities[193], and the existence of dog breeds which can provide advantages in genomic analysis.[194] Additionally, from a veterinary medicine standpoint, pet owners wish to improve and prolong the lives of their dogs.

Due to the immunogenicity of OSA tumors, development of immunotherapies can improve treatment outcomes.[191] Our collaborators are aiming to develop an adoptive cell therapy treatment for canine OSA patients using donor NK cells. To improve our understanding of the canine cell's behavior, ^{19}F MRI can be applied to a treatment model at 3T to track migration and persistence of adoptive cell therapy using NK cells. Utilizing the methodology described in this dissertation document, we aim to label expanded donor NK cells with a PFCE agent (Cenya Imaging, Amsterdam, NL), characterize the effects of cytotoxicity and viability, and track these cells *in vivo*.

To this end, NK cell labeling has been quantified via NMR and a ^{19}F limit for detection has been established in an ex vivo limb (see Chapter 5). Given the lower field strength of the clinical magnet (3T) in comparison with typical small animal systems, we anticipate that SNR will be reduced such that cell label uptake will need to be improved to ensure reliable detection *in vivo*. Recent work with our collaborators has demonstrated improved NK cell uptake of the ^{19}F PFPE and PFCE label in B6 mice when mechanical agitation of the incubator is included during the labeling process relative to non-agitated controls. Exemplary results, shown in Figure 6.3, indicate an average increase in cellular uptake of 15% relative to the non-agitated labeling groups. These advancement in cell labeling can improve the ability to detect smaller cell populations, and thus increase the overall achieved SNR. Future work will aim to test the improved labeling in canine donor NK cells and the ability to detect these labeled cells in both *ex vivo* limbs and *in vivo* canine patients.

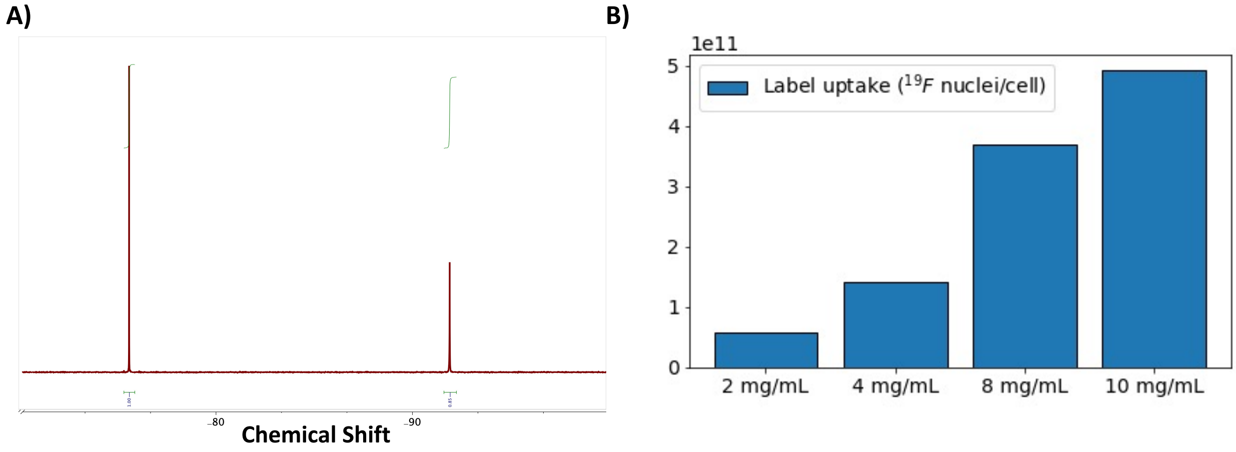

Figure 6.1: Spectra and PFCE label quantification for human monocytes. *A) A representative PFCE-labeled NK cell lysate NMR spectrum indicating PFCE uptake at approximately -92 ppm. B) Cell labeling repeated at 2, 4, 8, and 10 mg/mL for approximately 4 hours with the Cenya Imaging PFCE agent. Strong linearity (*R^2*>0.995) in label uptake is seen with increased incubation concentration.*

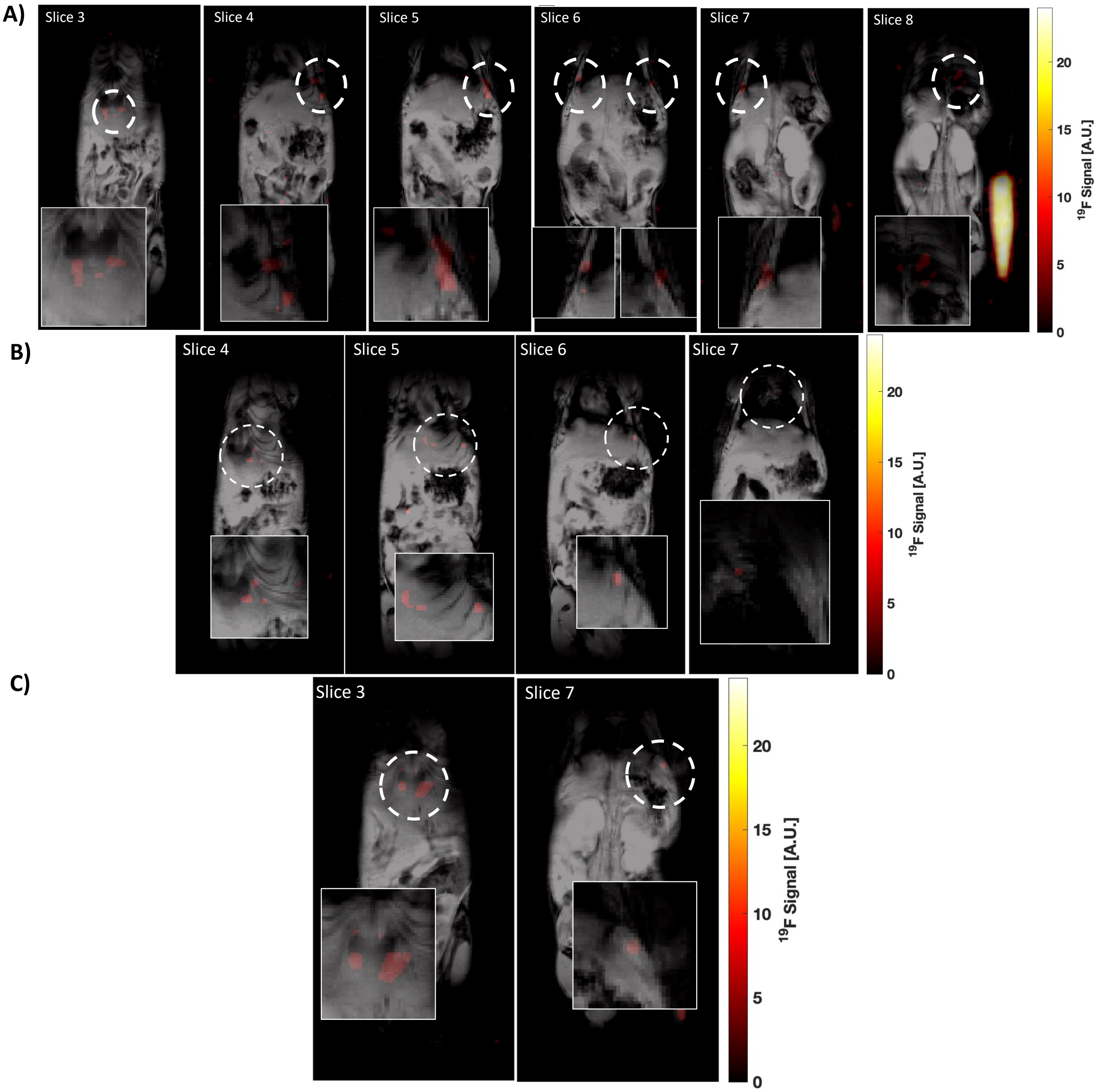

Figure 6.2: Coronal composite images demonstrating human monocyte tracking across multiple timepoints. *Coronal $^{1}H/^{19}F$ composite images from a single mouse across days 0 (top row), 1 (middle row), and 3 (bottom row) post-IV infusion of ^{19}F-labeled human monocytes. Images were thresholded at an SNR = 4, where regions with signal are indicated by the white dashed circles and accompanying zoomed pop-outs. Signal was primarily seen within the lymph nodes near the armpit.*

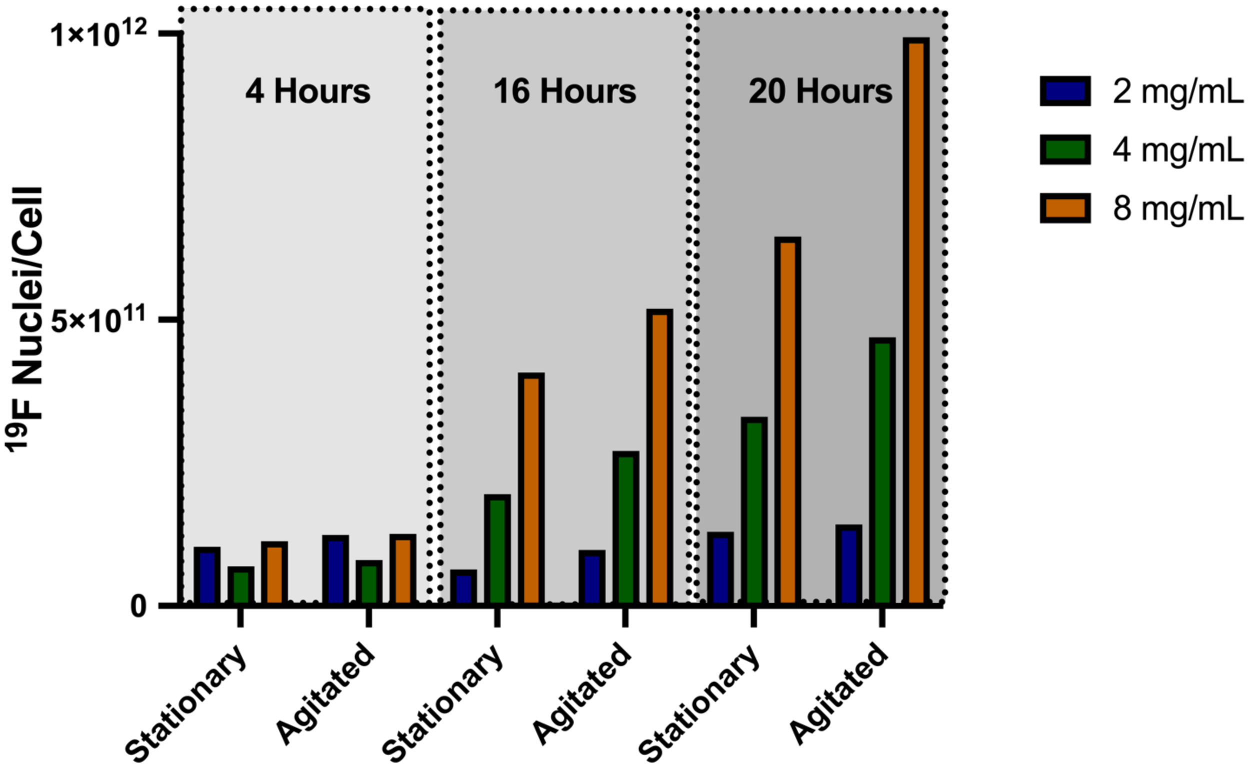

Figure 6.3: ^{19}F NMR label uptake quantification for mechanical agitated and non-agitated cells. *The NMR label uptake quantification results for B6 NK cells labeled at three ^{19}F concentrations across three time points for both mechanically agitated and non-agitated ("stationary") cell labeling conditions. Agitation was found to increase label uptake each concentration and time group.*

Chapter 7 PUBLICATIONS, PRESENTATIONS, AND TEACHING

7.1 Accepted Peer-Reviewed Journal Articles

- **Lechuga, Lawrence M.**, et al. "Detection and viability of murine NK cells in vivo in a lymphoma model using fluorine-19 MRI." *NMR in Biomedicine* 34.12 (2021): e4600.
- **Lechuga, Lawrence**, and Georg A. Weidlich. "Cone beam CT vs. fan beam CT: a comparison of image quality and dose delivered between two differing CT imaging modalities." *Cureus* 8.9 (2016).
- Weidlich, Vincent, **Lechuga, L**, Weidlich, G. "Concept for a Fan-beam Computed Tomography Image-guided Radiotherapy Device." *Cureus* 11.6 (2019).

7.2 Peer-Reviewed Journal Articles (Submitted or In Preparation)

- **Lechuga, L**, et al. “Pulse Sequences and Optimization Parameters for Cell Tracking Using Fluorine-19 MRI at 3T.” Magn Reson Med. (2022). *In preparation.*
- Barres A, **Lechuga L**, Tangsangasaksri M, Ludwig K, Fain S, Mecozzi S. “A stable, highly fluorous nanoemulsion formulation for in vivo cancer imaging via ^{19}F MRI”. ACS Biomater Sci Eng. 2020. *(In Preparation).*

7.3 Oral Presentation/Invited Talks

- **Lechuga, L.** “Preclinical Development and Translation of Fluorine-19 MRI”. Iowa Institute for Biomedical Imaging (IIBI). University of Iowa. Iowa City, IA, USA. April 28, 2022.
- **Lechuga, L.** “Translation of Fluorine-19 MRI to a Clinical 3T Platform”. Radiological Sciences Training Grant Symposium. University of Wisconsin – Madison. Madison, WI, USA. March 10, 2022.
- **Lechuga, L.** “Fluorine-19 MRI: Quantitative In Vivo Tracking of Murine Natural Killer Cells Within Lymphoma”. Radiological Sciences Training Grant Symposium. University of Wisconsin – Madison. Madison, WI, USA. January 16, 2021. (Presented virtually).

7.4 Conference Proceedings

- **Lechuga, L.**, Begovatz, P., Collick, B., Fain, S. (2022, May). “Optimization of a Phase-Cycled bSSFP for Improved SNR-efficiency in Fluorine-19 MRI at 3T”. Digital poster presented at the International Society of Magnetic Resonance in Medicine 2022 annual meeting.
- **Lechuga, L.**, Forsberg, M., Capitini, C., Fain, S. (2021, May). “In-Vivo Cell Tracking of Murine Natural Killer Cells in Lymphoma by Fluorine-19 MRI”. Digital poster presented virtually at the International Society of Magnetic Resonance in Medicine 2021 annual meeting.
- Begovatz, P., **Lechuga, L.**, Cho, M., Olsen, M., McMahon, R., Vail, D., Capitini, C., Fain, S. (2021, May). “Feasibility of Fluorine Magnetic Resonance Imaging for Natural Killer Cell Tracking with a Dual Tuned 1H/19F Torso Coil at 3T”. Research talk presented virtually at the International Society of Magnetic Resonance in Medicine 2021 annual meeting.
- **Lechuga, L.**, Forsberg, M., Ludwig, K., Capitini, C., Fain, S. (2020, Aug). “In Vivo Tracking and Quantification of Murine Natural Killer Cells via Fluorine-19 MRI”. Digital poster presented virtually at the International Society of Magnetic Resonance in Medicine 2020 annual meeting.
- Begovatz, P., Cho, M., **Lechuga, L.**, Olsen, M., McMahon, R., Vail, D., Capitini, C., Fain, S. (March 2021). “Canine Natural Killer Cell Tracking via Fluorine Magnetic Resonance Imaging (^{19}F-MRI) with a Clinical ^{1}H/^{19}F Torso Coil at 3T”. Virtual oral presentation at the 2021 University of Wisconsin Carbone Cancer Center Research Retreat.
- **Lechuga, L.**, Barres, A., Tangsangasaksri, M., Begovatz, P., Mecozzi, S., Fain, S. (2020, Aug). Assessment of Passive Tumor Targeting of a Novel PFCE-Loaded Nanoemulsion

via 19F-MRI. Digital poster presented virtually at the International Society of Magnetic Resonance in Medicine 2020 annual meeting.

- **Lechuga, L.**, Barres, A., Tangsangasaksri, M., Jin, W., Mecozzi, S., Morris, Z., Capitini, C., Fain, S. (March 2020). Fluorine-19 MRI: Translation of Cellular-Based Imaging to Clinical Application (Preliminary Insights). Digital poster presented at the 2020 University of Wisconsin Carbone Cancer Center Research Retreat.
- Ayars E., Lund D., and **Lechuga L.** "Real-Time Thermodynamic Experiments with High Resolution". AAPT National Meeting. Philadelphia PA, July 2012.
- Ayars E., Lund D., and **Lechuga L.** "Apparatus for Quantitative Measurement of Heat Flow in Two Dimensions", apparatus submitted for the AAPT apparatus competition, July 2012.

7.5 Teaching Experience

- Teaching assistant for Medical Physics 573 – Medical Image Science: Mathematical and Conceptual Foundations from August 2019 – January 2021.
- Teaching assistant for Medical Physics 574 – Imaging in Medicine: Applications from January 2020 – May 2021.

REFERENCES

1. The Union International Cancer Control. New Global Cancer Data: GLOBOCAN 2018 | UICC. *Geneva, Switzerland, 12 Sept 2018* . 2018;(September):1. https://www.uicc.org/new-global-cancer-data-globocan-2018.
2. Borghaei H, Smith MR, Campbell KS. Immunotherapy of cancer. *Eur J Pharmocology*. 2009;625(4):41-54. doi:10.1016/j.ejphar.2009.09.067.Immunotherapy
3. Chapelin F, Capitini CM, Ahrens ET. Fluorine-19 MRI for detection and quantification of immune cell therapy for cancer. *J Immunother Cancer*. 2018;6(1):1-11. doi:10.1186/s40425-018-0416-9
4. Miller JS, Soignier Y, Panoskaltsis-Mortari A, et al. Successful adoptive transfer and in vivo expansion of human haploidentical NK cells in patients with cancer. *Blood*. 2005;105(8):3051-3057. doi:10.1182/blood-2004-07-2974
5. Lang P, Handgretinger R. Haploidentical SCT in children: An update and future perspectives. *Bone Marrow Transplant*. 2008;42(SUPPL. 2):54-59. doi:10.1038/bmt.2008.285
6. Modak S, Le Luduec JB, Cheung IY, et al. Adoptive immunotherapy with haploidentical natural killer cells and Anti-GD2 monoclonal antibody m3F8 for resistant neuroblastoma: Results of a phase I study. *Oncoimmunology*. 2018;7(8):1-10. doi:10.1080/2162402X.2018.1461305
7. Cheng M, Chen Y, Xiao W, Sun R, Tian Z. NK cell-based immunotherapy for malignant diseases. *Cell Mol Immunol*. 2013;10(3):230-252. doi:10.1038/cmi.2013.10
8. Coca S, Perez-Piqueras J, Martinez D, et al. The prognostic significance of intratumoral natural killer cells in patients with colerectal carcinoma. *Cancer*. 1997;79(12):2320-2328. doi:10.1002/(SICI)1097-0142(19970615)79:12<2320::AID-CNCR5>3.0.CO;2-P
9. Ishigami S, Natsugoe S, Tokuda K, et al. Prognostic value of intratumoral natural killer cells in gastric carcinoma. *Cancer*. 2000;88(3):577-583. doi:10.1002/(SICI)1097-0142(20000201)88:3<577::AID-CNCR13>3.0.CO;2-V
10. Chapelin F, Gao S, Okada H, Weber TG, Messer K, Ahrens ET. Fluorine-19 nuclear magnetic resonance of chimeric antigen receptor T cell biodistribution in murine cancer model. *Sci Rep*. 2017;7(1). doi:10.1038/s41598-017-17669-4
11. Preclinical Assessment of Investigational Cellular and Gene Therapy Products | FDA. https://www.fda.gov/regulatory-information/search-fda-guidance-documents/preclinical-assessment-investigational-cellular-and-gene-therapy-products. Published 2013. Accessed January 23, 2020.
12. Srinivas M, Turner MS, Janjic JM, Morel PA, Laidlaw DH, Ahrens ET. In vivo cytometry of antigen-specific T cells using 19F MRI. *Magn Reson Med*. 2009;62(3):747-753. doi:10.1002/mrm.22063
13. Janjic JM, Ahrens ET. nanoemulsions for MRI cell tracking. *Nanomedicine*. 2009;1:492-501. doi:10.1002/wnan.035
14. Dunn GP, Bruce AT, Ikeda H, Old LJ, Schreiber RD. Cancer immunoediting: From immunosurveillance to tumor escape. *Nat Immunol*. 2002. doi:10.1038/ni1102-991
15. Khalil DN, Smith EL, Brentjens RJ, Wolchok JD. The future of cancer treatment: immunomodulation, CARs and combination immunotherapy. *Nat Rev Clin Oncol*. 2016;13(6):394. doi:10.1038/nrclinonc.2016.65
16. Bubeník J. Tumour MHC class I downregulation and immunotherapy (Review). *Oncol Rep*. 2003.
17. Strebhardt K, Ullrich A. Paul Ehrlich’s magic bullet concept. *Nat Rev Cancer*.

2008;8(june):473-480.

18. Jiang T, Zhou C, Ren S. Role of IL-2 in cancer immunotherapy. *Oncoimmunology*. 2016;5(6):1-10. doi:10.1080/2162402X.2016.1163462
19. Klapper JA, Downey SG, Smith FO, et al. High-dose interleukin-2 for the treatment of metastatic renal cell carcinoma: A retrospective analysis of response and survival in patients treated in the Surgery Branch at the National Cancer Institute between 1986 and 2006. *Cancer*. 2008;113(2):293-301. doi:10.1002/cncr.23552
20. Buss NAPS, Henderson SJ, McFarlane M, Shenton JM, De Haan L. Monoclonal antibody therapeutics: History and future. *Curr Opin Pharmacol*. 2012;12(5):615-622. doi:10.1016/j.coph.2012.08.001
21. Pierpont TM, Limper CB, Richards KL. Past, present, and future of Rituximab-The world's first oncology monoclonal antibody therapy. *Front Oncol*. 2018;8(JUN). doi:10.3389/fonc.2018.00163
22. Darvin P, Toor SM, Sasidharan Nair V, Elkord E. Immune checkpoint inhibitors: recent progress and potential biomarkers. *Exp Mol Med*. 2018;50(12):1-11. doi:10.1038/s12276-018-0191-1
23. Szöőr Á, Szöllősi J, Vereb G. From antibodies to living drugs: Quo vadis cancer immunotherapy? *Biol Futur*. 2021;72(1):85-99. doi:10.1007/s42977-021-00072-6
24. Jin S, Sun Y, Liang X, et al. Emerging new therapeutic antibody derivatives for cancer treatment. *Signal Transduct Target Ther*. 2022;7(1). doi:10.1038/s41392-021-00868-x
25. Rosenberg SA et al. Use of tumor Infiltrating Lymphocytes for the treatment of melanoma. *N Engl J Med*. 1988;319(25):1676-1680.
26. Rosenberg, Steven A. et al. Gene transfer into humans--immunotherapy of patients with advanced melanoma, using tumor-infiltrating lymphocytes modified by retroviral gene transduction. *N Engl J Med*. 1990;323(9):570-578. http://content.nejm.org/cgi/content/abstract/329/14/977%5Cnhttp://www.nejm.org/doi/abs/10.1056/NEJM199309303291401.
27. Gross G, Waks T, Eshhar Z. Expression of immunoglobulin-T-cell receptor chimeric molecules as functional receptors with antibody-type specificity. *Proc Natl Acad Sci U S A*. 1989;86(24):10024-10028. doi:10.1073/pnas.86.24.10024
28. Neelapu SS, Locke FL, Bartlett NL, et al. Axicabtagene Ciloleucel CAR T-Cell Therapy in Refractory Large B-Cell Lymphoma. *N Engl J Med*. 2017;377(26):2531-2544. doi:10.1056/nejmoa1707447
29. Schuster SJ, Bishop MR, Tam CS, et al. Tisagenlecleucel in Adult Relapsed or Refractory Diffuse Large B-Cell Lymphoma. *N Engl J Med*. 2019;380(1):45-56. doi:10.1056/nejmoa1804980
30. Ghobadi A, Dipersio JF. *Gene and Cellular Immunotherapy for Cancer*. Humana Press; 2022.
31. Souza-Fonseca-Guimaraes F, Cursons J, Huntington ND. The Emergence of Natural Killer Cells as a Major Target in Cancer Immunotherapy. *Trends Immunol*. 2019;40(2):142-158. doi:10.1016/j.it.2018.12.003
32. Ames E, Murphy WJ. Advantages and clinical applications of natural killer cells in cancer immunotherapy. *Cancer Immunol Immunother*. 2014;63(1):21-28. doi:10.1007/s00262-013-1469-8
33. Zitti B, Bryceson YT. Natural killer cells in inflammation and autoimmunity. *Cytokine Growth Factor Rev*. 2018;42(August):37-46. doi:10.1016/j.cytogfr.2018.08.001
34. Ruggeri L, Capanni M, Urbani E, et al. Effectiveness of donor natural killer cell aloreactivity in mismatched hematopoietic transplants. *Science (80-)*. 2002;295(5562):2097-2100. doi:10.1126/science.1068440

35. Varani, Auletta, Signore, Galli. State of the Art of Natural Killer Cell Imaging: A Systematic Review. *Cancers (Basel)*. 2019;11(7):967. doi:10.3390/cancers11070967
36. Seymour L, Bogaerts J, Perrone A, et al. iRECIST: guidelines for response criteria for use in trials testing immunotherapeutics. *Lancet Oncol*. 2017;18(3):e143-e152. doi:10.1016/S1470-2045(17)30074-8
37. Wolchok JD, Hoos A, O'Day S, et al. Guidelines for the evaluation of immune therapy activity in solid tumors: Immune-related response criteria. *Clin Cancer Res*. 2009;15(23):7412-7420. doi:10.1158/1078-0432.CCR-09-1624
38. Kurtz DM, Gambhir SS. *Tracking Cellular and Immune Therapies in Cancer*. Vol 124. 1st ed. Elsevier Inc.; 2014. doi:10.1016/B978-0-12-411638-2.00008-2
39. Badr CE, Tannous BA. Bioluminescence imaging: Progress and applications. *Trends Biotechnol*. 2011;29(12):624-633. doi:10.1016/j.tibtech.2011.06.010
40. Kircher MF, Gambhir SS, Grimm J. Noninvasive cell-tracking methods. *Nat Rev Clin Oncol*. 2011. doi:10.1038/nrclinonc.2011.141
41. Massoud TF, Gambhir SS. Molecular imaging in living subjects: Seeing fundamental biological processes in a new light. *Genes Dev*. 2003;17(5):545-580. doi:10.1101/gad.1047403
42. Bernstein M, King K, Zhou X aohong. *Handbook of MRI Pulse Sequences*. Amsterdam: Elsevier, Acad. Press; 2005.
43. Blumfield E, Swenson DW, Iyer RS, Stanescu AL. Gadolinium-based contrast agents — review of recent literature on magnetic resonance imaging signal intensity changes and tissue deposits, with emphasis on pediatric patients. *Pediatr Radiol*. 2019;49(4):448-457. doi:10.1007/s00247-018-4304-8
44. Wang Y-X. Superparamagnetic iron oxide based MRI contrast agents: Current status of clinical application. *Quant Imaging Med Surg*. 2011;1(1):35-40.
45. Hu SL, Lu PG, Zhang LJ, et al. In Vivo magnetic resonance imaging tracking of SPIO-labeled human umbilical cord mesenchymal stem cells. *J Cell Biochem*. 2012;113(3):1005-1012. doi:10.1002/jcb.23432
46. Rad AM, Arbab AS, Iskander ASM, Jiang Q, Soltanian-Zadeh H. Quantification of superparamagnetic iron oxide (SPIO)-labeled cells using MRI. *J Magn Reson Imaging*. 2007;26(2):366-374. doi:10.1002/jmri.20978
47. Dodd CH, Hsu HC, Chu WJ, et al. Normal T-cell response and in vivo magnetic resonance imaging of T cells loaded with HIV transactivator-peptide-derived superparamagnetic nanoparticles. *J Immunol Methods*. 2001;256(1-2):89-105. doi:10.1016/S0022-1759(01)00433-1
48. Heyn C, Bowen C V., Rutt BK, Foster PJ. Detection threshold of single SPIO-labeled cells with FIESTA. *Magn Reson Med*. 2005;53(2):312-320. doi:10.1002/mrm.20356
49. Haacke EM, Brown RW, Thompson MR, Venkatesan R. Haacke - Magnetic Resonance Imaging - Physical Principles and Sequence Design.pdf. *J Appl Phys*. 1999. doi:10.1063/1.3554697
50. Krafft MP. Fluorocarbons and fluorinated amphiphiles in drug delivery and biomedical research. *Adv Drug Deliv Rev*. 2001;47(2-3):209-228. doi:10.1016/S0169-409X(01)00107-7
51. Riess JG. Perfluorocarbon-based oxygen delivery. *Artif Cells, Blood Substitutes, Biotechnol*. 2006;34(6):567-580. doi:10.1080/10731190600973824
52. Riess JG. Understanding the fundamentals of perfluorocarbons and perfluorocarbon emulsions relevant to in vivo oxygen delivery. *Artif Cells Blood Substit Immobil Biotechnol*. 2005;33(1):47-63. doi:10.1081/BIO-200046659
53. Grapentin C, Mayenfels F, Barnert S, et al. Optimization of perfluorocarbon nanoemulsions

for molecular imaging by 19F MRI. *Nanomedicine*. 2014:268-286. doi:10.2119/molmed.2013.00045\rmolmed.2013.00045 [pii]

54. Díaz-López R, Tsapis N, Fattal E. Liquid perfluorocarbons as contrast agents for ultrasonography and 19F-MRI. *Pharm Res*. 2010;27(1):1-16. doi:10.1007/s11095-009-0001-5
55. Chapelin F, Okada H. Assessing Oximetry Response to Chimeric Antigen Receptor T-cell Therapy against Glioma with 19 F MRI in a Murine Model. 2021;19:1-9.
56. Yu JX, Hallac RR, Chiguru S, Mason RP. New frontiers and developing applications in 19F NMR. *Prog Nucl Magn Reson Spectrosc*. 2013;70:25-49. doi:10.1016/j.pnmrs.2012.10.001
57. Hitchens TK, Ye Q, Eytan DF, Janjic JM, Ahrens ET, Ho C. 19F MRI detection of acute allograft rejection with in vivo perfluorocarbon labeling of immune cells. *Magn Reson Med*. 2011;65(4):1144-1153. doi:10.1002/mrm.22702
58. Nöth U, Morrissey SP, Deichmann R, et al. Perfluoro-15-crown-5-ether labelled macrophages in adoptive transfer experimental allergic encephalomyelitis. *Artif Cells Blood Substit Immobil Biotechnol*. 1997;25(3):243-254. doi:10.3109/10731199709118914
59. Makela A V., Foster PJ. Imaging macrophage distribution and density in mammary tumors and lung metastases using fluorine-19 MRI cell tracking. *Magn Reson Med*. 2018;80(3):1138-1147. doi:10.1002/mrm.27081
60. Kennis BA, Michel KA, Brugmann WB, et al. Monitoring of intracerebellarly-administered natural killer cells with fluorine-19 MRI. *J Neurooncol*. 2019;142(3):395-407. doi:10.1007/s11060-019-03091-5
61. Bouchlaka MN, Ludwig KD, Gordon JW, et al. 19F-MRI for monitoring human NK cells in vivo. *Oncoimmunology*. 2016;5(5):1-12. doi:10.1080/2162402X.2016.1143996
62. Lechuga LM, Ludwig KD, Forsberg MH, Walker KL, Capitini CM, Fain SB. Detection and viability of murine NK cells in vivo in a lymphoma model using fluorine-19 MRI. *NMR Biomed*. 2021;(July):1-14. doi:10.1002/nbm.4600
63. Srinivas M, Morel PA, Ernst LA, Laidlaw DH, Ahrens ET. Fluorine-19 MRI for visualization and quantification of cell migration in a diabetes model. *Magn Reson Med*. 2007;58(4):725-734. doi:10.1002/mrm.21352
64. Gonzales C, Yoshihara HAI, Dilek N, et al. In-Vivo Detection and Tracking of T Cells in Various Organs in a Melanoma Tumor Model by 19 F-Fluorine MRS/MRI. *PLoS One*. 2016. doi:10.1371/journal.pone.0164557
65. Ahrens ET, Helfer BM, O'Hanlon CF, Schirda C. Clinical cell therapy imaging using a perfluorocarbon tracer and fluorine-19 MRI. *Magn Reson Med*. 2014;72(6):1696-1701. doi:10.1002/mrm.25454
66. Helfer BM, Balducci A, Nelson AD, et al. Functional assessment of human dendritic cells labeled for in vivo 19F magnetic resonance imaging cell tracking. *Cytotherapy*. 2010. doi:10.3109/14653240903446902
67. Boehm-Sturm P, Mengler L, Wecker S, Hoehn M, Kallur T. In Vivo tracking of human neural stem cells with 19F magnetic resonance imaging. *PLoS One*. 2011. doi:10.1371/journal.pone.0029040
68. Gaudet JM, Ribot EJ, Chen Y, Gilbert KM, Foster PJ. Tracking the fate of stem cell implants with fluorine-19 MRI. *PLoS One*. 2015;10(3):1-11. doi:10.1371/journal.pone.0118544
69. Helfer BM, Balducci A, Sadeghi Z, et al. 19F MRI tracer preserves in vitro and in vivo properties of hematopoietic stem cells. *Cell Transplant*. 2013;22(1):87-97. doi:10.3727/096368912X653174
70. Srinivas M, Heerschap A, Ahrens ET, Figdor CG, de Vries IJM. 19F MRI for quantitative in vivo cell tracking. *Trends Biotechnol*. 2010;28(7):363-370. doi:10.1016/j.tibtech.2010.04.002

71. Schubert R, Reichmann G, Schrader J, et al. In Vivo Monitoring of Inflammation After Cardiac and Cerebral Ischemia by Fluorine Magnetic Resonance Imaging. *Circulation*. 2008;118(2):140-148. doi:10.1161/circulationaha.107.737890
72. Temme S, Bönner F, Schrader J, Flögel U. 19F magnetic resonance imaging of endogenous macrophages in inflammation. *Wiley Interdiscip Rev Nanomedicine Nanobiotechnology*. 2012;4(3):329-343. doi:10.1002/wnan.1163
73. Temme S, Jacoby C, Ding Z, et al. Technical Advance: Monitoring the trafficking of neutrophil granulocytes and monocytes during the course of tissue inflammation by noninvasive 19F MRI. *J Leukoc Biol*. 2014;95(4):689-697. doi:10.1189/jlb.0113032
74. Waiczies S, Niendorf T, Lombardi G. Labeling of cell therapies: How can we get it right? *Oncoimmunology*. 2017;6(10):20-23. doi:10.1080/2162402X.2017.1345403
75. Waiczies H, Lepore S, Janitzek N, et al. Perfluorocarbon particle size influences magnetic resonance signal and immunological properties of dendritic cells. *PLoS One*. 2011;6(7):1-9. doi:10.1371/journal.pone.0021981
76. Fink C, Gaudet JM, Fox MS, et al. 19F-perfluorocarbon-labeled human peripheral blood mononuclear cells can be detected in vivo using clinical MRI parameters in a therapeutic cell setting. *Sci Rep*. 2018;8(1):1-13. doi:10.1038/s41598-017-19031-0
77. Janjic JM, Srinivas M, Kadayakkara DKK, Ahrens ET. Self-delivering nanoemulsions for dual fluorine-19 MRI and fluorescence detection. *J Am Chem Soc*. 2008;130(9):2832-2841. doi:10.1021/ja077388j
78. Balducci A, Wen Y, Zhang Y, et al. A novel probe for the non-invasive detection of tumor-associated inflammation. *Oncoimmunology*. 2013;2(2):37-41. doi:10.4161/onci.23034
79. Meier R, Piert M, Piontek G, et al. Tracking of [18F]FDG-labeled natural killer cells to HER2/neu-positive tumors. *Nucl Med Biol*. 2008;35(5):579-588. doi:10.1016/j.nucmedbio.2008.02.006
80. Sellmyer MA, Richman SA, Lohith K, et al. Imaging CAR T Cell Trafficking with eDFHR as a PET Reporter Gene. *Mol Ther*. 2019;28(1):42-51. doi:10.1016/j.ymthe.2019.10.007
81. Galli F, Rapisarda AS, Stabile H, et al. In vivo imaging of natural killer cell trafficking in tumors. *J Nucl Med*. 2015;56(10):1575-1580. doi:10.2967/jnumed.114.152918
82. Brand JM, Meller B, Von Hof K, et al. Kinetics and organ distribution of allogeneic natural killer lymphocytes transfused into patients suffering from renal cell carcinoma. *Stem Cells Dev*. 2004;13(3):307-314. doi:10.1089/154732804323099235
83. Dobrenkov K, Olszewska M, Likar Y, et al. Monitoring the efficacy of adoptively transferred prostate cancer-targeted human T lymphocytes with PET and bioluminescence imaging. *J Nucl Med*. 2008;49(7):1162-1170. doi:10.2967/jnumed.107.047324
84. Ahrens ET, Bulte JWM. Tracking immune cells in vivo using magnetic resonance imaging. *Nat Rev Immunol*. 2013;13(10):755-763. doi:10.1038/nri3531
85. Glover JC, Aswendt M, Boulland JL, et al. In vivo Cell Tracking Using Non-invasive Imaging of Iron Oxide-Based Particles with Particular Relevance for Stem Cell-Based Treatments of Neurological and Cardiac Disease. *Mol Imaging Biol*. 2020;22(6):1469-1488. doi:10.1007/s11307-019-01440-4
86. Yu J, Kodibagkar V, Cui W, Mason R. 19F: A Versatile Reporter for Non-Invasive Physiology and Pharmacology Using Magnetic Resonance. *Curr Med Chem*. 2005;12(7):819-848. doi:10.2174/0929867053507342
87. Ruiz-Cabello J, Barnett BP, Bottomley PA, Bulte JWM. Fluorine (19F) MRS and MRI in biomedicine. *NMR Biomed*. 2011;24(2):114-129. doi:10.1002/nbm.1570
88. Amiri H, Srinivas M, Veltien A, van Uden MJ, de Vries IJM, Heerschap A. Cell tracking using 19F magnetic resonance imaging: Technical aspects and challenges towards clinical applications. *Eur Radiol*. 2015;25(3):726-735. doi:10.1007/s00330-014-3474-5

89. Gustafson HH, Holt-Casper D, Grainger DW, Ghandehari H. Nanoparticle uptake: The phagocyte problem. *Nano Today*. 2015;10(4):487-510. doi:10.1016/j.nantod.2015.06.006
90. Rosenberg SA, Restifo NP, Yang JC, Morgan RA, Dudley ME. Adoptive cell transfer: A clinical path to effective cancer immunotherapy. *Nat Rev Cancer*. 2008;8(4):299-308. doi:10.1038/nrc2355
91. Schlom J, Vergati M, Intrivici C, Huen NY, Tsang KY. Strategies for cancer vaccine development. *J Biomed Biotechnol*. 2010;2010. doi:10.1155/2010/596432
92. Dougan M, Dranoff G. Immune therapy for cancer. *Annu Rev Immunol*. 2009;27:83-117. doi:10.1146/annurev.immunol.021908.132544
93. Morris ZS, Guy EI, Francis DM, et al. In situ tumor vaccination by combining local radiation and tumor-specific antibody or immunocytokine treatments. *Cancer Res*. 2016;76(13):3929-3941. doi:10.1158/0008-5472.CAN-15-2644
94. Taylor P. Ostwald ripening in emulsions. *Adv Colloid Interface Sci*. 1998. doi:10.1016/S0001-8686(98)00035-9
95. Patel SK, Williams J, Janjic JM. Cell labeling for 19F MRI: New and improved approach to perfluorocarbon nanoemulsion design. *Biosensors*. 2013;3(3):341-359. doi:10.3390/bios3030341
96. Flogel U, Ahrens E, eds. *Fluorine Magnetic Resonance Imaging*. Pan Standford Publishing Pte. Ltd.; 2017. doi:10.1201/9781315364605
97. Pelchen-Matthews A, Parsons IJ, Marsh M. Phorbol Ester-induced Downregulation of CD4 is a Multistep Process Involving Dissociation from p56lck, Increased Association with Clathrin-coated Pits, and Altered Endosomal Sorting. *J Exp Med*. 1993;178(October). http://jem.rupress.org/content/178/4/1209.full.pdf.
98. Emens LA, Ascierto PA, Darcy PK, et al. Cancer immunotherapy: Opportunities and challenges in the rapidly evolving clinical landscape. *Eur J Cancer*. 2017;81:116-129. doi:10.1016/j.ejca.2017.01.035
99. Couzin-Frankel J. Cancer immunotherapy. *Science (80-)*. 2013;342(6165):1432-1433. doi:10.1126/science.342.6165.1432
100. Melero I, Rouzaut A, Motz GT, Coukos G. T-cell and NK-cell infiltration into solid tumors: A key limiting factor for efficacious cancer immunotherapy. *Cancer Discov*. 2014;4(5):522-526. doi:10.1158/2159-8290.CD-13-0985
101. Beatty GL, Gladney WL. Immune escape mechanisms as a guide for cancer immunotherapy. *Clin Cancer Res*. 2015;21(4):687-692. doi:10.1158/1078-0432.CCR-14-1860
102. Guillerey C, Huntington ND, Smyth MJ. Targeting natural killer cells in cancer immunotherapy. *Nat Immunol*. 2016;17(9):1025-1036. doi:10.1038/ni.3518
103. Berg M, Lundqvist A, McCoy P, et al. Clinical-grade ex vivo-expanded human natural killer cells up-regulate activating receptors and death receptor ligands and have enhanced cytolytic activity against tumor cells. *Cytotherapy*. 2009;11(3):341-355. doi:10.1080/14653240902807034
104. Liu E, Marin D, Banerjee P, et al. Use of CAR-transduced natural killer cells in CD19-positive lymphoid tumors. *N Engl J Med*. 2020;382(6):545-553. doi:10.1056/NEJMoa1910607
105. Barkholt L, Alici E, Conrad R, et al. Safety analysis of ex vivo-expanded NK and NK-like T cells administered to cancer patients: A Phase I clinical study. *Immunotherapy*. 2009. doi:10.2217/IMT.09.47
106. Yang Y, Lim O, Kim TM, et al. Phase I study of random healthy donor-derived allogeneic natural killer cell therapy in patients with malignant lymphoma or advanced solid tumors. *Cancer Immunol Res*. 2016;4(3):215-224. doi:10.1158/2326-6066.CIR-15-0118

107. Shah NN, Baird K, Delbrook CP, et al. Acute GVHD in patients receiving IL-15/4-1BBL activated NK cells following T-cell-depleted stem cell transplantation. *Blood*. 2015;125(5):784-792. doi:10.1182/blood-2014-07-592881

108. Geller MA, Cooley S, Judson PL, et al. A phase II study of allogeneic natural killer cell therapy to treat patients with recurrent ovarian and breast cancer. *Cytotherapy*. 2011;13(1):98-107. doi:10.3109/14653249.2010.515582

109. Ciurea SO, Schafer JR, Bassett R, et al. Phase 1 clinical trial using mbIL21 ex vivo-expanded donor-derived NK cells after haploidentical transplantation. *Blood*. 2017;130(16):1857-1868. doi:10.1182/blood-2017-05-785659

110. Ishikawa T, Okayama T, Sakamoto N, et al. Phase I clinical trial of adoptive transfer of expanded natural killer cells in combination with IgG1 antibody in patients with gastric or colorectal cancer. *Int J Cancer*. 2018;142(12):2599-2609. doi:10.1002/ijc.31285

111. Sta Maria NS, Barnes SR, Jacobs RE. In Vivo Monitoring of Natural Killer Cell Trafficking during Tumor Immunotherapy. *Magn Reson Insights*. 2014;7:MRI.S13145. doi:10.4137/mri.s13145

112. Smyth MJ, Hayakawa Y, Takeda K, Yagita H. New aspects of natural-killer-cell surveillance and therapy of cancer. *Nat Rev Cancer*. 2002. doi:10.1038/nrc928

113. Sungur CM, Murphy WJ. Utilization of mouse models to decipher natural killer cell biology and potential clinical applications. *Hematology Am Soc Hematol Educ Program*. 2013;2013:227-233. doi:10.1182/asheducation-2013.1.227

114. Fridman WH, Pagès F, Sauts-Fridman C, Galon J. The immune contexture in human tumours: Impact on clinical outcome. *Nat Rev Cancer*. 2012;12(4):298-306. doi:10.1038/nrc3245

115. Ratner A V., Muller HH, Bradley-Simpson B, et al. Detection of tumors with 19F magnetic resonance imaging. *Invest Radiol*. 1988. doi:10.1097/00004424-198805000-00006

116. Somanchi SS, Kennis BA, Gopalakrishnan V, Lee DA, Bankson JA. In vivo 19F-magnetic resonance imaging of adoptively transferred NK cells. *Methods Mol Biol*. 2016;1441:317-332. doi:10.1007/978-1-4939-3684-7_27

117. Hernandez R, Walker KL, Grudzinski JJ, et al. 90Y-NM600 targeted radionuclide therapy induces immunologic memory in syngeneic models of T-cell Non-Hodgkin's Lymphoma. *Commun Biol*. 2019;2(1). doi:10.1038/s42003-019-0327-4

118. Gudbjartsson H, Patz S. The rician distribution of noisy mri data. *Magn Reson Med*. 1995;34(6):910-914. doi:10.1002/mrm.1910340618

119. Vivier E, Ugolini S, Blaise D, Chabannon C, Brossay L. Targeting natural killer cells and natural killer T cells in cancer. *Nat Rev Immunol*. 2012;12(4):239-252. doi:10.1038/nri3174

120. Jha P, Golovko D, Bains S, et al. Monitoring of natural killer cell immunotherapy using noninvasive imaging modalities. *Cancer Res*. 2010;70(15):6109-6113. doi:10.1158/0008-5472.CAN-09-3774

121. Neubauer AM, Myerson J, Caruthers SD, et al. Gadolinium-modulated 19F signals from perfluorocarbon nanoparticles as a new strategy for molecular imaging. *Magn Reson Med*. 2008;60(5):1066-1072. doi:10.1002/mrm.21750

122. Mathiasen AB, Qayyum AA, Jørgensen E, et al. In Vivo MRI Tracking of Mesenchymal Stromal Cells Labeled with Ultrasmall Paramagnetic Iron Oxide Particles after Intramyocardial Transplantation in Patients with Chronic Ischemic Heart Disease. *Stem Cells Int*. 2019;2019. doi:10.1155/2019/2754927

123. Makela A V., Gaudet JM, Foster PJ. Quantifying tumor associated macrophages in breast cancer: A comparison of iron and fluorine-based MRI cell tracking. *Sci Rep*. 2017;7(February):1-9. doi:10.1038/srep42109

124. Meller B, Frohn C, Brand JM, et al. Monitoring of a new approach of immunotherapy with

allogenic 111In-labelled NK cells in patients with renal cell carcinoma. *Eur J Nucl Med Mol Imaging*. 2004;31(3):403-407. doi:10.1007/s00259-003-1398-4

125. Grégoire C, Cognet C, Chasson L, et al. Intrasplenic trafficking of natural killer cells is redirected by chemokines upon inflammation. *Eur J Immunol*. 2008;38(8):2076-2084. doi:10.1002/eji.200838550
126. Rachel Liou HL, Myers JT, Barkauskas DS, Huang AY. Intravital imaging of the mouse popliteal lymph node. *J Vis Exp*. 2012;(60):1-5. doi:10.3791/3720
127. van Heeswijk RB, Colotti R, Darçot E, et al. Chemical shift encoding (CSE) for sensitive fluorine-19 MRI of perfluorocarbons with complex spectra. *Magn Reson Med*. 2018;79(5):2724-2730. doi:10.1002/mrm.26895
128. Goette MJ, Keupp J, Rahmer J, Lanza GM, Wickline SA, Caruthers SD. Balanced UTE-SSFP for 19F MR imaging of complex spectra. *Magn Reson Med*. 2015. doi:10.1002/mrm.25437
129. Schmid F, Höltke C, Parker D, Faber C. Boosting 19F MRI - SNR efficient detection of paramagnetic contrast agents using ultrafast sequences. *Magn Reson Med*. 2013;69(4):1056-1062. doi:10.1002/mrm.24341
130. Kislukhin AA, Xu H, Adams SR, Narsinh KH, Tsien RY, Ahrens ET. Paramagnetic fluorinated nanoemulsions for sensitive cellular fluorine-19 magnetic resonance imaging. *Nat Mater*. 2016;15(6):662-668. doi:10.1038/nmat4585
131. Pruessmann KP, Weiger M, Scheidegger MB, Boesiger P. SENSE: Sensitivity encoding for fast MRI. *Magn Reson Med*. 1999. doi:10.1002/(sici)1522-2594(199911)42:5<952::aid-mrm16>3.3.co;2-j
132. Lustig M, Donoho DL, Santos JM, Pauly JM. Compressed Sensing MRI. *IEEE Signal Process Mag*. 2008;25(2):72-82. doi:10.1109/msp.2007.914728
133. Lustig M, Donoho D, Pauly JM. Sparse MRI: The application of compressed sensing for rapid MR imaging. *Magn Reson Med*. 2007;58(6):1182-1195. doi:10.1002/mrm.21391
134. Zhong J, Mills PH, Hitchens TK, Ahrens ET. Accelerated fluorine-19 MRI cell tracking using compressed sensing. *Magn Reson Med*. 2013;69(6):1683-1690. doi:10.1002/mrm.24414
135. Neal MA, Pippard BJ, Hollingsworth KG, et al. Optimized and accelerated 19F-MRI of inhaled perfluoropropane to assess regional pulmonary ventilation. *Magn Reson Med*. 2019;82(4):1301-1311ok. doi:10.1002/mrm.27805
136. Fröbom R, Berglund E, Berglund D, et al. Phase I trial evaluating safety and efficacy of intratumorally administered inflammatory allogeneic dendritic cells (ilixadencel) in advanced gastrointestinal stromal tumors. *Cancer Immunol Immunother*. 2020;69(11):2393-2401. doi:10.1007/s00262-020-02625-5
137. Subbiah V, Murthy R, Hong DS, et al. Cytokines produced by dendritic cells administered intratumorally correlate with clinical outcome in patients with diverse cancers. *Clin Cancer Res*. 2018;24(16):3845-3856. doi:10.1158/1078-0432.CCR-17-2707
138. Tchou J, Zhao Y, Levine BL, et al. Safety and efficacy of intratumoral injections of chimeric antigen receptor (CAR) T cells in metastatic breast cancer. *Cancer Immunol Res*. 2017;5(12):1152-1161. doi:10.1158/2326-6066.CIR-17-0189
139. Laurell A, Lönnemark M, Brekkan E, et al. Intratumorally injected pro-inflammatory allogeneic dendritic cells as immune enhancers: A first-in-human study in unfavourable risk patients with metastatic renal cell carcinoma. *J Immunother Cancer*. 2017;5(1):1-15. doi:10.1186/s40425-017-0255-0
140. Lee JM, Lee MH, Garon E, et al. Phase I trial of intratumoral injection of CCL21 gene–modified dendritic cells in lung cancer elicits tumor-specific immune responses and CD8+ T-cell infiltration. *Clin Cancer Res*. 2017;23(16):4556-4568. doi:10.1158/1078-0432.CCR-

16-2821
141. Rozera C, Cappellini AG, D'Agostino G, et al. Intratumoral injection of IFN-alpha dendritic cells after dacarbazine activates anti-tumor immunity: Results from a phase I trial in advanced melanoma. *J Transl Med*. 2015;13(1):1-13. doi:10.1186/s12967-015-0473-5
142. Fujiwara S, Wada H, Miyata H, et al. Clinical trial of the intratumoral administration of labeled DC combined with systemic chemotherapy for esophageal cancer. *J Immunother*. 2012;35(6):513-521. doi:10.1097/CJI.0b013e3182619cb4
143. Plewes DB, Kucharczyk W. Physics of MRI: A primer. *J Magn Reson Imaging*. 2012;35(5):1038-1054. doi:10.1002/jmri.23642
144. Rastogi N, Tyagi N, Singh O, et al. Mn(II) based T1 and T2 potential MRI contrast agent appended with tryptamine: Recognition moiety for Aβ-plaques. *J Inorg Biochem*. 2017;177(August):76-81. doi:10.1016/j.jinorgbio.2017.08.007
145. Tirotta I, Dichiarante V, Pigliacelli C, et al. 19 F Magnetic Resonance Imaging (MRI): From Design of Materials to Clinical Applications . *Chem Rev*. 2015;115(2):1106-1129. doi:10.1021/cr500286d
146. Rogosnitzky M, Branch S. Gadolinium-based contrast agent toxicity: a review of known and proposed mechanisms. *BioMetals*. 2016;29(3):365-376. doi:10.1007/s10534-016-9931-7
147. Hao D, Ai T, Goerner F, Hu X, Runge VM, Tweedle M. MRI contrast agents: Basic chemistry and safety. *J Magn Reson Imaging*. 2012;36(5):1060-1071. doi:10.1002/jmri.23725
148. Kanda T, Fukusato T, Matsuda M, et al. Gadolinium-based contrast agent accumulates in the brain even in subjects without severe renal dysfunction: Evaluation of autopsy brain specimens with inductively coupled plasma mass spectroscopy. *Radiology*. 2015;276(1):228-232. doi:10.1148/radiol.2015142690
149. Gulani V, Calamante F, Shellock FG, Kanal E, Reeder SB. Gadolinium deposition in the brain: summary of evidence and recommendations. *Lancet Neurol*. 2017;16(7):564-570. doi:10.1016/S1474-4422(17)30158-8
150. Figdor CG, Bonetto F, de Vries IJM, Heerschap A, Srinivas M, Cruz LJ. Customizable, multi-functional fluorocarbon nanoparticles for quantitative in vivo imaging using 19F MRI and optical imaging. *Biomaterials*. 2010;31(27):7070-7077. doi:10.1016/j.biomaterials.2010.05.069
151. Blanco E, Shen H, Ferrari M. Principles of nanoparticle design for overcoming biological barriers to drug delivery. *Nat Biotechnol*. 2015;33(9):941-951. doi:10.1038/nbt.3330
152. Kobayashi H, Turkbey B, Watanabe R, Choyke PL. Cancer drug delivery: Considerations in the rational design of nanosized bioconjugates. *Bioconjug Chem*. 2014;25(12):2093-2100. doi:10.1021/bc500481x
153. Schleich N, Po C, Jacobs D, et al. Comparison of active, passive and magnetic targeting to tumors of multifunctional paclitaxel/SPIO-loaded nanoparticles for tumor imaging and therapy. *J Control Release*. 2014;194:82-91. doi:10.1016/j.jconrel.2014.07.059
154. Diou O, Tsapis N, Giraudeau C, et al. Long-circulating perfluorooctyl bromide nanocapsules for tumor imaging by 19FMRI. *Biomaterials*. 2012;33(22):5593-5602. doi:10.1016/j.biomaterials.2012.04.037
155. Barres AR, Wimmer MR, Mecozzi S. Multicompartment Theranostic Nanoemulsions Stabilized by a Triphilic Semifluorinated Block Copolymer. *Mol Pharm*. 2017;14(11):3916-3926. doi:10.1021/acs.molpharmaceut.7b00624
156. Cox BL, Ludwig KD, Adamson EB, Eliceiri K, Fain SB. An open source, 3D printed preclinical MRI phantom for repeated measures of contrast agents and reference standards. *Biomed Phys Eng Express*. 2018;4(2). doi:10.1088/2057-1976/aa9491

157. Ludwig KD, Hernando D, Roberts NT, van Heeswijk RB, Fain SB. A chemical shift encoding (CSE) approach for spectral selection in fluorine-19 MRI. *Magn Reson Med*. 2018;79(4):2183-2189. doi:10.1002/mrm.26874
158. Constantinides C, Maguire ML, Stork L, et al. Temporal accumulation and localization of isoflurane in the C57BL/6 mouse and assessment of its potential contamination in 19F MRI with perfluoro-crown-ether-labeled cardiac progenitor cells at 9.4 Tesla. *J Magn Reson Imaging*. 2017;45(6):1659-1667. doi:10.1002/jmri.25564
159. Press P. Basic Pharmacokinetics sample. *Basic Pharmacokinet*. 2012:106-130.
160. Jacoby C, Temme S, Mayenfels F, et al. Probing different perfluorocarbons for in vivo inflammation imaging by 19F MRI: Image reconstruction, biological half-lives and sensitivity. *NMR Biomed*. 2014;27(3):261-271. doi:10.1002/nbm.3059
161. Wooster TJ, Golding M, Sanguansri P. Impact of oil type on nanoemulsion formation and ostwald ripening stability. *Langmuir*. 2008;24(22):12758-12765. doi:10.1021/la801685v
162. Maeda H, Nakamura H, Fang J. The EPR effect for macromolecular drug delivery to solid tumors: Improvement of tumor uptake, lowering of systemic toxicity, and distinct tumor imaging in vivo. *Adv Drug Deliv Rev*. 2013;65(1):71-79. doi:10.1016/j.addr.2012.10.002
163. Rosenberg SA. Progress in human tumour immunology and immunotherapy. *Nature*. 2001;411(6835):380-384. doi:10.1038/35077246
164. Turtle CJ, Hanafi LA, Berger C, et al. CD19 CAR-T cells of defined CD4+:CD8+ composition in adult B cell ALL patients. *J Clin Invest*. 2016;126(6):2123-2138. doi:10.1172/JCI85309
165. Newick K, O’Brien S, Moon E, Albelda SM. CAR T Cell Therapy for Solid Tumors. *Annu Rev Med*. 2017;68(1):139-152. doi:10.1146/annurev-med-062315-120245
166. Hingorani D V., Chapelin F, Stares E, Adams SR, Okada H, Ahrens ET. Cell penetrating peptide functionalized perfluorocarbon nanoemulsions for targeted cell labeling and enhanced fluorine-19 MRI detection. *Magn Reson Med*. 2020;83(3):974-987. doi:10.1002/mrm.27988
167. Colotti R, Bastiaansen JAM, Wilson A, et al. Characterization of perfluorocarbon relaxation times and their influence on the optimization of fluorine-19 MRI at 3 tesla. *Magn Reson Med*. 2017;77(6):2263-2271. doi:10.1002/mrm.26317
168. Hargreaves BA, Vasanawala SS, Pauly JM, Nishimura DG. Characterization and reduction of the transient response in steady-state MR imaging. *Magn Reson Med*. 2001;46(1):149-158. doi:10.1002/mrm.1170
169. Hargreaves B. Rapid gradient-echo imaging. *J Magn Reson Imaging*. 2012;36(6):1300-1313. doi:10.1002/jmri.23742
170. Chavhan GB, Babyn PS, Jankharia BG, Cheng HLM, Shroff MM. Steady-state MR imaging sequences: Physics, classification, and clinical applications. *Radiographics*. 2008;28(4):1147-1160. doi:10.1148/rg.284075031
171. Griswold MA, Jakob PM, Heidemann RM, et al. Generalized Autocalibrating Partially Parallel Acquisitions (GRAPPA). *Magn Reson Med*. 2002;47(6):1202-1210. doi:10.1002/mrm.10171
172. Watts R, Wang Y. k-space interpretation of the Rose Model: Noise limitation on the detectable resolution in MRI. *Magn Reson Med*. 2002;48(3):550-554. doi:10.1002/mrm.10220
173. Renieblas GP, Nogués AT, González AM, Gómez-Leon N, del Castillo EG. Structural similarity index family for image quality assessment in radiological images. *J Med Imaging*. 2017;4(3):035501. doi:10.1117/1.jmi.4.3.035501
174. Wang Z, Simoncelli EP, Bovik AC. Multi-scale structural similarity for image quality assessment. *Thrity-Seventh Asilomar Conf Signals, Syst Comput*. 2003;2:1398-1402.

doi:10.1109/acssc.2003.1292216

175. Constantinides CD, Ergin A, Mcveigh ER. Signal-to-Noise Measurements in Magnitude Images from NMR Phased Arrays. *Magn Reson Med*. 1997;2(5):1113-1162. doi:10.1007/978-981-4560-44-3_37

176. Kellman P, Mcveigh ER. SNR Unit Recon. *Magn Reson Med*. 2008;54(6):1439-1447. doi:10.1002/mrm.20713.Image

177. Weibel S, Basse-Luesebrink TC, Hess M, et al. Imaging of Intratumoral Inflammation during Oncolytic Virotherapy of Tumors by 19F-Magnetic Resonance Imaging (MRI). *PLoS One*. 2013;8(2). doi:10.1371/journal.pone.0056317

178. Vasudeva K, Andersen K, Zeyzus-Johns B, et al. Imaging neuroinflammation in vivo in a neuropathic pain rat model with near-infrared fluorescence and 19 magnetic resonance. *PLoS One*. 2014;9(2):1-12. doi:10.1371/journal.pone.0090589

179. Balducci A, Helfer BM, Ahrens ET, O'Hanlon CF 3rd, Wesa AK. Visualizing arthritic inflammation and 1. Balducci, A., Helfer, B. M., Ahrens, E. T., O'Hanlon, C. F. 3rd & Wesa, A. K. Visualizing arthritic inflammation and therapeutic response by fluorine-19 magnetic resonance imaging (19F MRI). J. Inflamm. (Lond). 9,. *J Inflamm (Lond)*. 2012;9(1):24.

180. Staal AHJ, Becker K, Tagit O, et al. In vivo clearance of 19F MRI imaging nanocarriers is strongly influenced by nanoparticle ultrastructure. *Biomaterials*. 2020;261. doi:10.1016/j.biomaterials.2020.120307

181. Mallett CL, Foster PJ. Optimization of the balanced steady state free precession (bSSFP) pulse sequence for magnetic resonance imaging of the mouse prostate at 3T. *PLoS One*. 2011;6(4):3-8. doi:10.1371/journal.pone.0018361

182. Elliott AM, Bernstein MA, Ward HA, Lane J, Witte RJ. Nonlinear averaging reconstruction method for phase-cycle SSFP. *Magn Reson Imaging*. 2007;25(3):359-364. doi:10.1016/j.mri.2006.09.013

183. Robson PM, Grant AK, Madhuranthakam AJ, Lattanzi R, Sodickson DK, McKenzie CA. Comprehensive quantification of signal-to-noise ratio and g-factor for image-based and k-space-based parallel imaging reconstructions. *Magn Reson Med*. 2008;60(4):895-907. doi:10.1002/mrm.21728

184. Schulte RF, Sacolick L, Deppe MH, et al. Transmit gain calibration for nonproton MR using the Bloch-Siegert shift. *NMR Biomed*. 2011;24(9):1068-1072. doi:10.1002/nbm.1657

185. Hofer M, Hoferová Z, Depeš D, Falk M. Combining pharmacological countermeasures to attenuate the acute radiation syndrome-A concise review. *Molecules*. 2017;22(5). doi:10.3390/molecules22050834

186. Donnelly EH, Nemhauser JB, Smith JM, et al. Acute radiation syndrome: Assessment and management. *South Med J*. 2010;103(6):541-546. doi:10.1097/SMJ.0b013e3181ddd571

187. Dainiak N. Medical management of acute radiation syndrome and associated infections in a high-casualty incident. *J Radiat Res*. 2018;59(March):ii54-ii64. doi:10.1093/jrr/rry004

188. López M, Martín M. Medical management of the acute radiation syndrome. *Reports Pract Oncol Radiother*. 2011;16(4):138-146. doi:10.1016/j.rpor.2011.05.001

189. Forsberg MH, Kink JA, Thickens AS, et al. Exosomes from primed MSCs can educate monocytes as a cellular therapy for hematopoietic acute radiation syndrome. *Stem Cell Res Ther*. 2021;12(1):1-15. doi:10.1186/s13287-021-02491-7

190. Chinnadurai R, Forsberg MH, Kink JA, Hematti P, Capitini CM. Use of MSCs and MSC-educated macrophages to mitigate hematopoietic acute radiation syndrome. *Curr Stem Cell Reports*. 2020;6(3):77-85. doi:10.1007/s40778-020-00176-0.Use

191. Kisseberth WC, Lee DA. Adoptive Natural Killer Cell Immunotherapy for Canine Osteosarcoma. *Front Vet Sci*. 2021;8(June):1-8. doi:10.3389/fvets.2021.672361

192. Fenger JM, London CA, Kisseberth WC. Canine osteosarcoma: A naturally occurring disease to inform pediatric oncology. *ILAR J*. 2014;55(1):69-85. doi:10.1093/ilar/ilu009

193. Paoloni M, Davis S, Lana S, et al. Canine tumor cross-species genomics uncovers targets linked to osteosarcoma progression. *BMC Genomics*. 2009;10(625):1-13. doi:10.1186/1471-2164-10-625

194. Fan TM, Khanna C. Comparative aspects of osteosarcoma pathogenesis in humans and dogs. *Vet Sci*. 2015;2(3):210-230. doi:10.3390/vetsci2030210